UC Berkeley
UC Berkeley Electronic Theses and Dissertations

**Title**
Electrical and Electrothermal Transport Properties of n- and p-type InN

**Permalink**
https://escholarship.org/uc/item/8fd7p32m

**Author**
Miller, Nathaniel Reed

**Publication Date**
2010

Peer reviewed|Thesis/dissertation

eScholarship.org Powered by the California Digital Library
University of California

# Electrical and Electrothermal Transport Properties of n- and p-type InN

by

Nathaniel Reed Miller

A dissertation submitted in partial satisfaction of the
requirements for the degree of
Doctor of Philosophy

in

Engineering - Materials Science and Engineering

in the

GRADUATE DIVISION
of the
UNIVERSITY OF CALIFORNIA, BERKELEY

Committee in charge:
Professor Eugene E. Haller, Chair
Dr. Joel W. Ager III
Professor Oscar Dubon
Professor Ali Javey

Fall 2010

**Electrical and Electrothermal Transport Properties of n- and p-type InN**

Copyright 2010
by
Nathaniel Reed Miller

# Abstract

Electrical and Electrothermal Transport Properties of n- and p-type InN

by

Nathaniel Reed Miller

Doctor of Philosophy in Engineering - Materials Science and Engineering

University of California, Berkeley

Professor Eugene E. Haller, Chair

The group III-N alloy system has attracted considerable interest for various electronic and opto-electronic applications including high power and high frequency electronics, photovoltaics, photo-electrochemical electrodes, and solid-state light emitters. While wide-gap group III-N materials have achieved commercial success and technological maturity, more narrow-gap alloys closer to the InN end of the system have yet to make an impact. The unique defect properties of InN, mostly stemming from an unusually large electron affinity, have masked even the most basic electronic and optical properties and made technological advancement difficult. This dissertation builds upon the collective work of the small InN community that has been slowly building up fundamental understanding of this material over the last decade.

The development of thermopower measurements as a tool for investigating the transport properties of InN is a recurring theme in this work. Thermopower measurements of Mg-doped InN provide some of the first definitive proof of free-hole conduction and help to elucidate the role of Mg as an acceptor. Analysis of multilayer structures using a parallel conduction model allows measurement of two of the most fundamental p-type transport properties, free-hole concentration and mobility, which have been difficult to evaluate by other techniques. Well developed transport modeling theories are extended to include the effects of donor-type, charged dislocation scattering on electron mobility and thermopower in n-type InN. Comparison of this modeling to variable temperature transport data and electron microscopy has provided strong evidence that the high density of dislocations in InN are positively charged donors and can limit the electron mobility in n-type InN. Finally, electrolyte gating is shown to be a powerful tool for controlling the surface band bending condition. Using this technique, parasitic surface currents are eliminated leading to the first measurement of rectification in InN, a crucial step on the path towards InN device development.

# Contents


**1 Introduction** **1**
- 1.1 A brief history of nitride semiconductors . . . 1
- 1.2 Unique properties of indium nitride . . . 2
- 1.3 Characterization challenges and solutions for p-type InN . . . 9

**2 Mg-doping in InN** **17**
- 2.1 Background and theory . . . 17
- 2.2 Experimental methods . . . 20
- 2.3 Electrical and thermoelectric measurements . . . 21
- 2.4 Photoluminescence . . . 25
- 2.5 Conclusions . . . 29

**3 Thermopower of parallel conducting structures** **31**
- 3.1 Background and theory . . . 31
- 3.2 Undoped interlayer experiment . . . 34
- 3.3 Conclusions and future work . . . 42

**4 Dislocation scattering in n-type InN** **44**
- 4.1 Background . . . 44
- 4.2 Experiment . . . 47
- 4.3 Theory . . . 49
- 4.4 Results and discussion . . . 54
- 4.5 Conclusions . . . 60

**5 Electrolyte-gated transport** **61**
- 5.1 Background and theory . . . 61
- 5.2 Electrolyte-gated thermopower measurements . . . 63
- 5.3 Electrolyte-gated IV measurements . . . 66

**6 Conclusions and future work** **73**

**References** **75**

**A Broader thermoelectric background and theory** **85**
- A.1 Thermoelectric Effects and Devices . . . 85
- A.2 Origins of the Seebeck Effect . . . 89

**B Thermopower equipment and measurement details** **92**
B.1 Variable temperature apparatus: setup and instrumentation . . . . . . . . . . . . . . . 92
B.2 Variable temperature rig: thermopower data collection . . . . . . . . . . . . . . . . . . 94
B.3 Room temperature apparatus . . . . . . . . . . . . . . . . . . . . . . . . . . . . . . . . . 95

**C Interlayer experiment modeling** **97**

**D Electrolyte-based measurements** **100**

## Acknowledgments

I would like to acknowledge the continual support of my family and friends, especially the patience and understanding of my special lady friend and darling fiancée, Amy. I also acknowledge the continual input and encouragement of Joel Ager for motivating, guiding, and mentoring me throughout my career at Berkeley. I also acknowledge the support and guidance throughout my graduate student career from my advisor, Eugene Haller; with a strong sense of how things "should be" he puts the wellbeing of his students and the quality of our science first and then everything else, core values that will continue to shape my personal and professional development long into the future. I also acknowledge the members of the Haller research group and Wladek Walukiewicz (who always knows the answer), Kin Man Yu, Zuzanna Liliental-Weber, and the members of the Solar Energy Materials Research Group who have made considerable intellectual contributions to my work. Jeff Beeman, Bill Hansen, Lothar Reichertz, and Holland Smith have aided considerably in the development of the thermopower instrumentation and provided unending technical and personal support. Special thanks also go to David Hom for crucial help in navigating the administrative labyrinth of LBL and for keeping my spirits high and my ego in check with encouragement, humor, and snarky comments. I also acknowledge the invaluable efforts of Bill Schaff's group at Cornell University, Jim Speck's group at UC - Santa Barbara, and Ke "Michael" Wang and Yasushi Nanishi's group at Ritsumeikan University in Japan for growth of the InN films used in this study and for continual intellectual exchange and collaboration. Finally, I must acknowledge the support of the Department of Defense and the Department of Energy; this research was made with Government support under and awarded by DoD, Air Force Office of Scientific Research, National Defense Science and Engineering Graduate (NDSEG) Fellowship, 32 CFR 168a; this work was supported by the Director, Office of Science, Office of Basic Energy Sciences, Division of Materials Sciences and Engineering, of the U.S. Department of Energy under Contract no. DE-AC02-05CH11231.

# Chapter 1

# Introduction

## 1.1 A brief history of nitride semiconductors

Although Si is and possibly always will be the preeminent semiconductor, its properties are not ideal for every application, and it must sometimes yield to other materials. Specifically, Si is usually not preferred for applications requiring light emission, high power, or high frequency operation [1]. This is where compound semiconductors often come to the forefront. It should be remembered that when Michael Faraday observed the first semiconducting properties in 1833 (decreasing resistivity with increasing temperature), he was studying a *compound* semiconductor, AgS [2, 3]. And much of the early practical success for semiconductors came from the use of PbS (galena) in "crystal radios." Even the first observation of a photovoltaic effect by Edmund Becquerel in 1839 occurred with the compound semiconductor AgCl [4]. However, the early dominance of compound semiconductors would soon come to an end. With the need for millions of point contact rectifiers in Allied radar receivers, the elemental group IV semiconductors Si and Ge got a big boost during World War II. Owing mostly to wartime research and development efforts, purification of these elemental materials vastly accelerated, producing 5-nines pure (99.999%) Si by war's end. Then when the first transistor was developed at Bell Labs in 1947 using a slab of high-purity Ge, the legacy of the group IV elemental semiconductors really began. Soon after in 1958-1961, the first integrated circuits were developed at Texas Instruments, again using Ge. Eventually Si would gain preference due to its nearly surface-state-free oxide, and the semiconductor industry began steadily following Moore's Law by doubling the density of transistors on integrated curcuits every two years. Today, state of the art integrated circuits made from Si contain more than 2 billion transistors. Si dominates the integrated circuit industry, and despite inroads by other technologies, still accounts for the majority of the photovoltaics industry.

However, this is certainly not the whole story. In general, both Si and Ge have a tremendous disadvantage when it comes to optoelectronic applications in that they both have indirect bandgaps. This means that optical absorption and emission require the aid of a phonon or other species to match the momentum of the recombining carriers, making these processes inherently inefficient. And so it is here that compound semiconductors have the upper hand, as many have direct bandgaps, allowing for efficient absorption or emission of light. It is not surprising then that the primary employment for compound semiconductors comes in the manufacture of high-efficiency photovoltaics (PV), laser diodes (LDs), and perhaps most importantly light emitting diodes (LEDs). These industries primarily use alloys of group III-Vs such as GaAs and GaP. The use of GaAs electronics has also grown tremendously for applications in cellular phones where

its high carrier mobilities have made low power consumption, high-frequency devices possible. Although the wide variety of bandgaps and other properties available with the more exotic group III-V and II-VI materials has been exploited for myriad specialty optical applications, most have found no large volume industrial use. However, a revolution occurred beginning in the early 1990's with the introduction of high-brightness blue LEDs and LDs based on Ga-rich InGaN alloys following the pioneering work by Shuji Nakamura at Nichia Chemical [5–7].

This achievement brought wide-gap, group III-nitride materials into the spotlight for the first time where they are now used extensively for blue and green light emitters in a large range of optoelectronic applications, among them high power green LEDs in displays, traffic lights, and white lighting, and blue LDs in the now-famous BluRay disc players. Optical storage capacity has increased enormously with the introduction of nitride-based lasers with shorter wavelengths and thus smaller focus spots; compact disc (CD) technology based on infrared lasers producing a capacity of 0.65 Gb quickly gave way to digital versatile disks (DVDs) using 650 nm red AlGaInP lasers producing a capacity of 4.7 Gb and now the use of nitride-based 405 nm violet lasers has pushed the capacity into the 25-200 Gb range [8]. Whereas optical storage requires ever shorter wavelengths, nitride materials for LEDs need to go in the other direction. Fig. 1.1a shows how the different colors of the spectrum are created with various group III-V materials, relying heavily on InGaN materials for both blue and green. Fig. 1.1b shows that the efficiency of LEDs made from both InGaN and AlGaInP degrade sharply in moving towards the green part of the spectrum. Dubbed the "green valley of death," this represents a major challenge to the LED industry. High-efficiency green emitters are required to enable widespread commercial use of solid-state lighting, which holds the promise of lower power consumption, longer lifetime, and greater reliability over incandescents. Alloys in this range are also sought for laser diodes, photovoltaics, and photoelectrochemical cell production of hydrogen from water [9–15]. For InGaN materials, moving towards the green part of the spectrum requires the incorporation of more In, a process which so far has been plagued by structural defects, phase segregation, degraded optical properties, and difficulties with p-type doping. By the early 2000's, the Ga-rich end of the alloy system had become quite mature, even enjoying great commercial successes, but little was known about InN or In-rich group III-N alloys. However, with the weight of such important commercial enterprise and the looming presence of scientific mysteries, the field was ripe for a revolution in understanding.

## 1.2 Unique properties of indium nitride

### 1.2.1 Revision of the bandgap and usefulness for optoelectronics

For about three decades the fundamental bandgap of indium nitride (InN) was believed to be $\sim$1.9 eV based on optical measurements of films with electron concentrations $\geq 10^{19}$ cm$^{-3}$ and mobilities less than 100 cm$^2$/Vs [16, 17]. These films were synthesized by radio frequency sputtering of In metal in a high-purity nitrogen atmosphere, yielding polycrystalline films with high densities of structural and chemical defects [17, 18]. In the early 2000's when high-quality, single-crystalline films were first grown using more sophisticated techniques such as molecular beam epitaxy (MBE) and metal organic chemical vapor deposition (MOCVD), the electrical and optical properties were found to be very different; lower defect densities led to lower free carrier concentrations, higher mobilities, and absorption edges below 1 eV [19–23]. It was discovered that the large bandgap measured previously was the result of the Burstein-Moss effect, a phenomenon in which degenerate carrier concentrations lead to filled states from the bottom of the conduction band to large energies

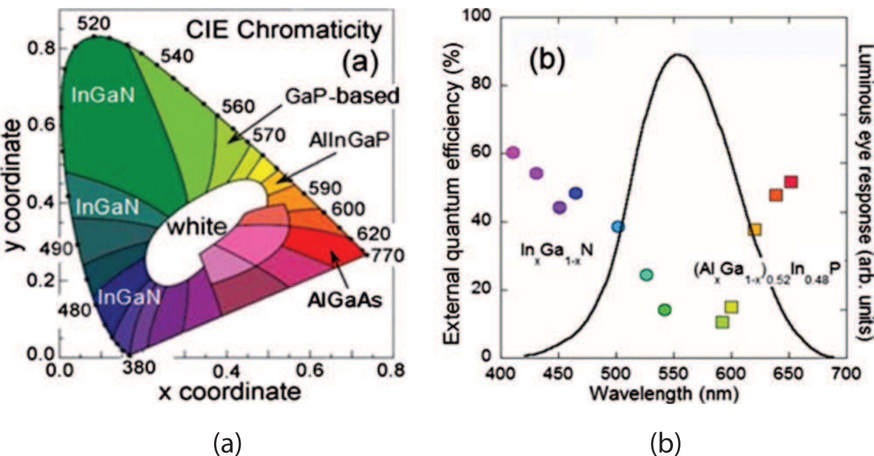


**Figure 1.1** (a) Diagram showing the so-called CIE chromaticity for different compound semiconductor based LED technologies. Creating white light requires some contribution from red, green, and blue light emitters, relying increasingly on InGaN materials for green and blue wavelength ranges. (b) The colored dots/squares show the achieved external quantum efficiency of various LED materials plotted as a function of emission wavelength illustrating the so-called "green valley of death." Plotted on top of this (solid line) is the response of the human eye to various colors showing that the valley of death corresponds exactly to the most sensitive wavelengths of the eye. Fig. reproduced from Ref. [14].

preventing optical transitions from the top of the valence band to the bottom of the conduction band [24–26]. In this case optical spectroscopy yields an absorption edge which can be significantly larger than the fundamental bandgap.

State of the art undoped InN (at room temperature) has an electron concentration in the low $10^{17}$ $cm^{-3}$ range, a mobility as high as 2250 $cm^2$/Vs, and a bandgap of 0.675 eV where only the third digit is still debated in the literature [27, 28]. The revision of the bandgap down to such low energy has opened up new opportunities for optoelectronic applications utilizing InN and its alloys (InGaN and InAlN). Nitride alloys are now known to have bandgaps extending from InN $E_g$ = 0.675 eV ($\lambda > 1800$ nm) to GaN $E_g$ = 3.4 eV ($\lambda = 365$ nm) and AlN $E_g$ = 6.1 eV ($\lambda = 203$ nm), spanning virtually the entire solar spectrum and including all visible wavelengths [11]. Fig. 1.2 shows the bandgaps of the nitride alloys as a function of lattice parameter as adapted from reference [17]. Devices such as solar cells, laser diodes, and light emitting diodes made from nitride alloys could therefore operate over this entire range of photon energies making the study of this alloy system very important. As high-quality InN has only been available for about the last decade, it is the least studied of the nitride materials and great effort has begun by researchers worldwide to understand the unique properties of this material, some of which will be elucidated below.

### 1.2.2 High Electron Affinity

Many of the unique properties of InN stem from its extremely high electron affinity, which depending on the band offset values used, lies in the range of 5.5-5.8 eV [29–31]. This is the largest electron affinity of all group III-V semiconductors and puts the conduction band lower than most if not all known semiconductor materials as shown in Fig. 1.3. An important consequence of this fundamental property is that native defects tend to be donors in InN. This tendency is quantified

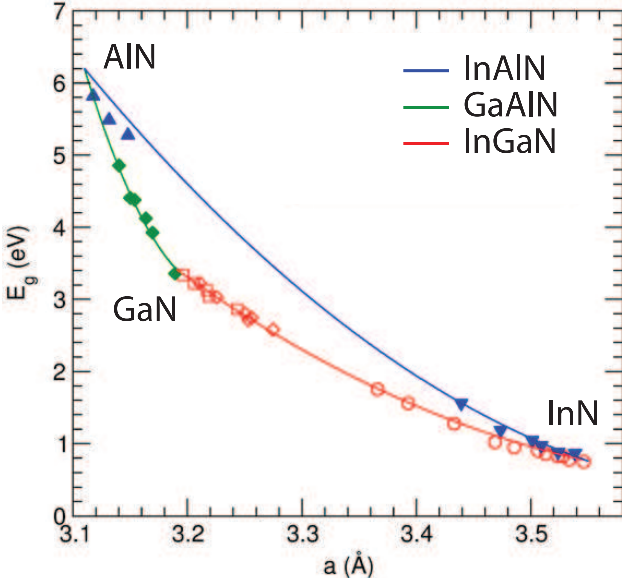


**Figure 1.2** Summary of observed bandgaps of the nitride alloys plotted as a function of lattice parameter showing that the nitride alloy system spans nearly the full solar spectrum, which is most intense from ∼0.5 eV to ∼ 4 eV. Figure adapted from reference [17].

within the Amphoteric Defect Model (ADM) developed by Walukiewicz [32, 33]. This model states that the average energy of localized native point defects is found at a universal energy level reference in semiconductors referred to as the Fermi level stabilization energy, $E_{FS}$. The formation energy of such defects is Fermi level dependent and $E_{FS}$ is the energy at which the formation energy of donor type and acceptor type native defects is equal. If the Fermi level ($E_F$) is below $E_{FS}$ then donor defects have lower formation energy and if $E_F$ is above $E_{FS}$, acceptor type defects have lower formation energy such that there is a donor to acceptor transition at $E_{FS}$.

A conceptually different model that predates the ADM has also been applied to InN to describe the nature of surface defects; this theory introduces the "branch point energy" or "charge neutrality level" which are in close agreement with $E_{FS}$ [34–36].[a] A universal energy level for hydrogen is also predicted theoretically, which is close to the position of $E_{FS}$ [38]. The position of $E_{FS}$ relative to the band edges greatly affects the properties of the material. As seen in Fig. 1.3, $E_{FS}$ is found within the bandgap of most semiconductor materials. However, in rare cases $E_{FS}$ is found above the conduction band edge and InN is the most extreme case with $E_{FS}$ nearly 1 eV above the conduction band minimum. Since the Fermi level is nearly always below $E_{FS}$ in InN, the formation energy of donor type native defects is reduced, which has a profound effect on the electrical and optical properties.

Due to the large electron affinity, persistent n-type conductivity is observed in undoped InN material, and since native defects tend to be donors, the electron concentration depends strongly on the structural quality of the films. In addition to native point defects, impurities such as H and O as well as extended defects such as dislocations have been proposed as important donors

[a] Taking a weighted average of the conduction and valence bands over all of k-space results in a charge neutrality level, which is typically in the gap. For InN, this is also true on the whole, although a very sharp minimum in the conduction band at the gamma point puts the charge neutrality level above the conduction band at the zone center [37].

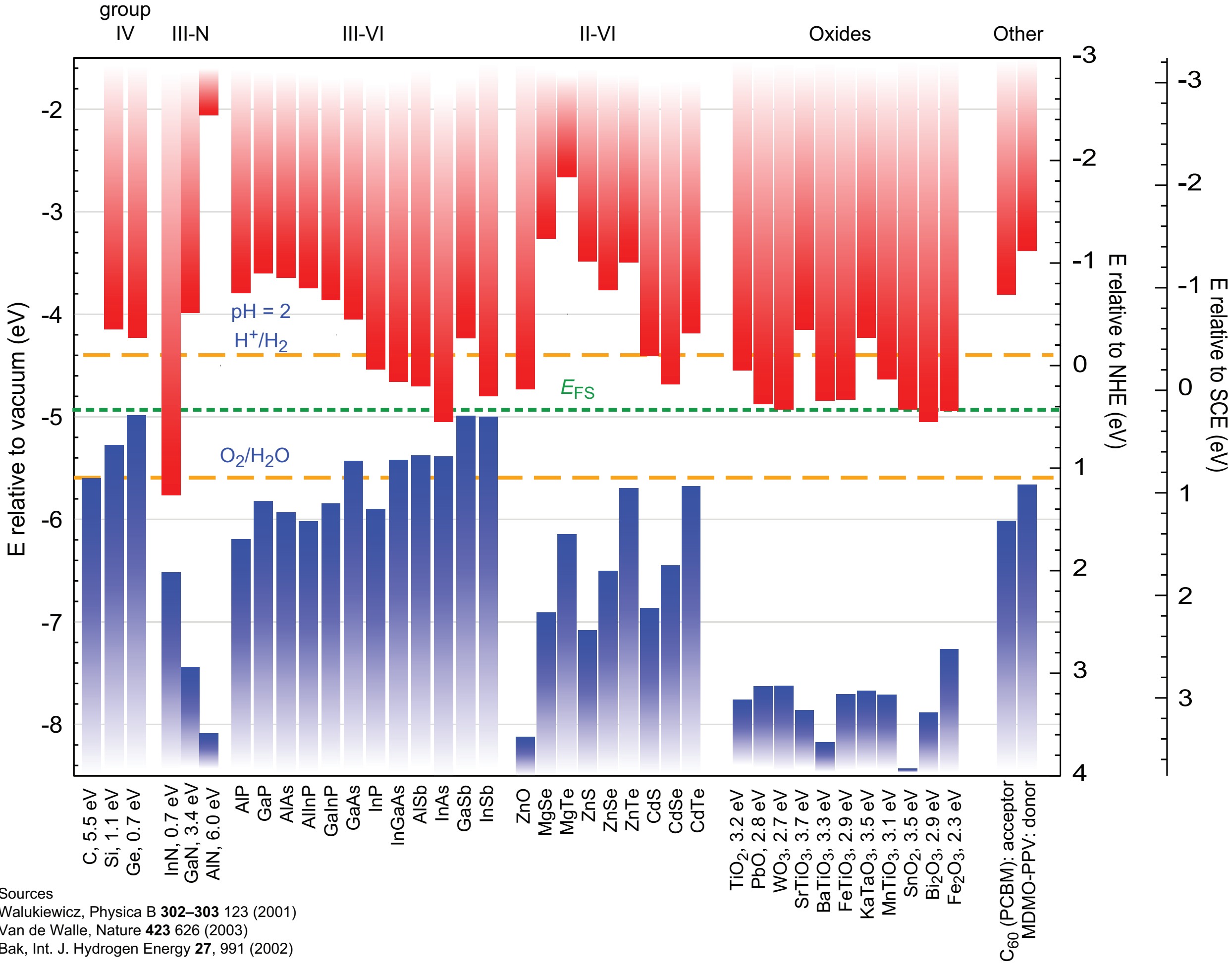


**Figure 1.3** Summary of conduction and valence band positions for various semiconductor materials on several universal energy scales including the position of the Fermi level stabilization energy $E_{FS}$ from the ADM of Walukiewicz [32]. $E_{FS}$ coincides well with the "branch point energy" or "charge neutrality level" proposed by other researchers [35]. This figure courtesy of Dr. Joel Ager III.

in InN [14, 39]. As discussed in section 1.2.1, improved film growth techniques have lowered the minimum electron concentration from $10^{20}$ cm$^{-3}$ to as low as $10^{17}$ cm$^{-3}$. However, even state of the art films are degenerately doped, meaning the Fermi level is above the conduction band edge.[b] In comparison, ultra-pure Ge material, which has a similar bandgap, is available as intrinsic material with carrier concentrations as low as $10^{10}$ cm$^{-3}$. The high carrier concentration in InN was the cause of the erroneous measurement of its bandgap due to the Burstein-Moss effect discussed previously. In fact, the carrier concentration of a high-quality sample can be increased by creating donor type defects using particle irradiation; the absorption edge increases until the Fermi level saturates at $E_{FS}$, thus recreating the Burstein-Moss effect [26, 40–43]. Furthermore, areas of high defect density such as surfaces and interfaces are subject to electron accumulation; the Fermi level tends to pin at $E_{FS}$ ~1 eV above the conduction band edge leading to downward band bending and electron accumulation [40, 44–48]. Fig. 1.4 shows this surface electron accumulation and associated conduction band bending derived from high-resolution electron-energy-loss spectroscopy [45].

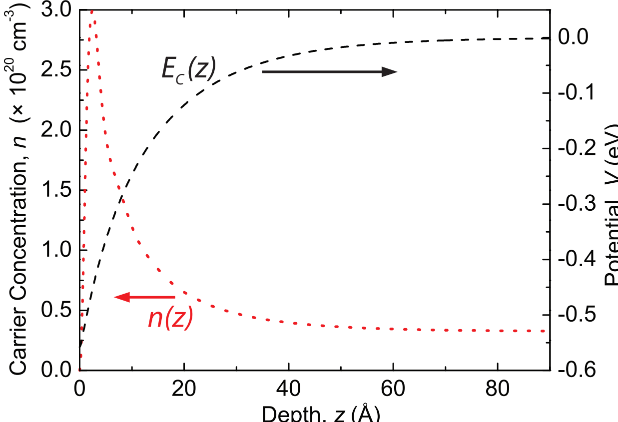


**Figure 1.4** Diagram showing the bending of the conduction band edge (black dashed) and electron concentration (red dashed) as a function of distance from the surface of InN adapted from Mahboob *et al.* [45]. Note that the surface electron accumulation is very thin, contained within the first few nanometers of material.

Although surface pinning and the associated electron accumulation/inversion is well documented, it is not yet well known what happens at threading dislocations, which exist in concentrations of $10^9 - 10^{11}$ cm$^{-2}$ in InN. One could assume that dislocations pin the Fermi level just like the surface, in which case they would be expected to accumulate electrons and act like metallic wires, as shown schematically in Fig. 1.5. This kind of scenario is supported by recent calculations, which report that the Fermi level is pinned as much as 0.6 eV above the conduction band minimum at edge-type dislocations [39]. In this configuration, edge-type dislocations would act as donors, as suggested by several reports that dislocations are a significant source of the background electron concentration in InN [49–52]. If so, then the dislocations would be expected to be positively charged and therefore act as strong scattering centers for electrons and holes, significantly affect-

[b] In fact, the carrier concentration is almost completely invariant to temperature. Because the carriers are delocalized into a band they do not "freeze out" upon cooling even to liquid He temperature. Heating to high temperature could theoretically enable observation of the intrinsic regime; however, at the low decomposition temperature of InN ~ 500 °C, the intrinsic carrier concentration is only ~ $10^{17}$ cm$^{-3}$ (assuming parabolic bands, $E_g = 0.7$ eV, $m_e^* = 0.07m_\circ$, and $m_h^* = 0.7m_\circ$), largely preventing this experiment in practice.

ing the mobility [53–55]. However, these studies do not support causation so much as correlation between electron density and dislocation density, and there are those that show the opposite result [56]. It is also unclear whether the donor nature of dislocations is intrinsic or extrinsic, i.e., is it the property of dislocations themselves, or the result of decoration by point defects. Regardless, the effect of extended dislocations on transport in InN is of paramount importance given the high density of such defects. This issue will be addressed further in chapter 4, including the presentation of experimental and theoretical investigations.

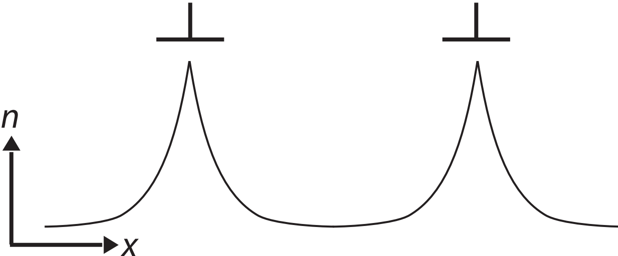


**Figure 1.5** Schematic diagram showing variation of electron concentration ($n$) as a function of distance ($x$) in the vicinity of threading dislocation cores ($\perp$) in InN.

### 1.2.3 Non-parabolic conduction band

A common property of narrow-gap semiconductors is a strongly nonparabolic conduction band due to the $k \cdot p$ interaction. It has been studied extensively in the model narrow gap material InSb with the theory laid out by Kane [57]. Using Kane's model and extensions by Zawadzki and Szymanska, it can be shown that the conduction band dispersion is defined by only two parameters: the bandgap and the band edge effective mass, and is given by the following relation [58, 59]

$$E_C(k) = -\frac{E_g}{2} + \frac{\hbar^2 k^2}{2m_o} + \sqrt{\frac{E_g^2}{4} + E_g \frac{\hbar^2 k^2}{2m^*}} \tag{1.1}$$

where $E_g$ is the bandgap, $\hbar$ is Planck's constant divided by $2\pi$, $k$ is the wavevector, and $m_o$ and $m^*$ are the free electron and electron effective masses, respectively. The $k$-dependent effective mass is given by the following expression:

$$m^*(k) = \frac{\hbar^2 k}{dE_C(k)/dk} \tag{1.2}$$

which shows that for a nonparabolic conduction band the effective mass of the free carriers depends on their momentum (or equivalently their energy). In a nondegenerate semiconductor, even one with a nonparabolic conduction band, most of the free carriers are found near the bottom of the conduction band and the $k$-dependent effective mass does not have a strong effect. But in a material such as InN the Fermi level is above the conduction band edge by as much as 1 eV depending on the free electron concentration. Like in a metal, the free carriers are found near the Fermi level and therefore the effective mass of free carriers can vary greatly from sample to sample. This property of InN has turned the determination of the electron effective mass into a challenge, and debate

continues in the literature where in recent years values of the effective mass have been reported in the range of 0.033 to 0.076 $m_o$ [59–63]. Now that consensus has been reached on the fundamental bandgap of InN, the effective mass must be similarly determined to fully understand the band structure.

The top diagram of Fig. 1.6 shows the calculated parabolic and nonparabolic conduction band dispersion diagrams for InN with the same band edge effective mass of 0.065 $m_o$. Note that above ∼100 meV from the band edge the parabolic and nonparabolic curves deviate significantly. The bottom of Fig. 1.6 shows the $k$-dependent effective mass for parabolic (constant) and nonparabolic bands illustrating the increasing effective mass with increasing $k$. The density of states, and thus the carrier concentration, is affected by this band restructuring. Fig. 1.7 shows the calculated electron concentration as a function of Fermi level position relative to the band edge for parabolic and nonparabolic conduction bands. Note that for a given Fermi level position the resulting carrier concentration is higher in the nonparabolic case due to the increased density of states. This diagram also shows that the electron concentration where the nondegenerate to degenerate transition occurs is in the low $10^{17}$ $cm^{-3}$ range. All of these effects are important concerns in the calculation of transport coefficients such as mobility and thermopower where these properties depend on the effective mass and the relationship between carrier concentration and Fermi level. Thus, accurate treatment of the nonparabolicity of the conduction band is essential [14].

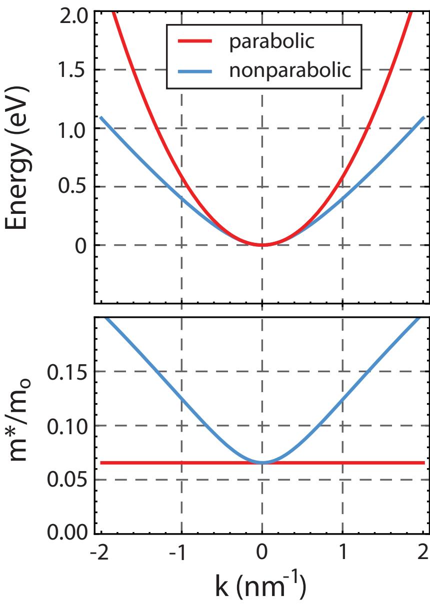


**Figure 1.6** Top: Parabolic and nonparabolic dispersion diagrams for InN with the same band edge effective mass of 0.065 $m_o$. Bottom: Calculated $k$-dependence of the effective mass for parabolic and nonparabolic conduction band.

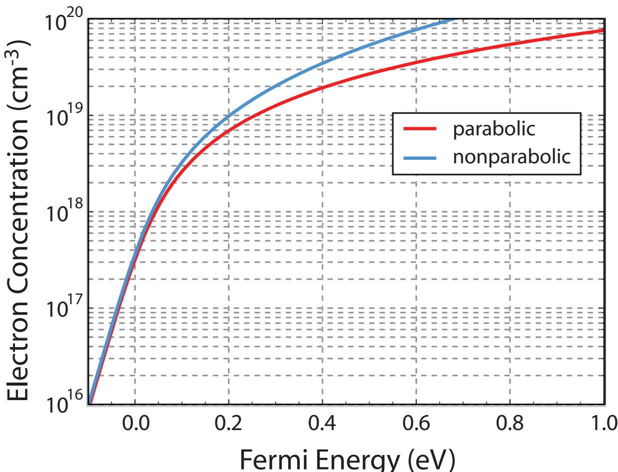


**Figure 1.7** Calculated carrier concentration as a function of Fermi level position relative to the band edge for parabolic and nonparabolic conduction bands. The bandgap and band edge effective mass are assumed to be 0.7 eV and 0.065 $m_o$, respectively.

## 1.3 Characterization challenges and solutions for p-type InN

### 1.3.1 Doping Limits

Most useful semiconductor devices require the formation of p-n junctions, which in turn requires control of the majority carrier type. In fact, the ability to make a semiconductor both n-type and p-type is one of the more fundamental milestones in the development of a material for scientific and technological applications. The difficulty in achieving p-type InN has been a great barrier to progress with InN and In-rich nitride alloys. All undoped material is n-type, as discussed previously, due to the high electron affinity of InN, and early efforts to dope the material p-type were unsuccessful. The ADM has some predictive power as to how well a material can be doped either n-type or p-type by examining the position of $E_{FS}$ relative to the conduction and valence band edges as shown by Walukiewicz and similarly by others; empirical observations imply that there is a limit as to how far the Fermi level can be moved away from $E_{FS}$ by doping [33, 36].

For instance, many oxide semiconductors have conduction bands near $E_{FS}$ and valence bands far below as shown in Fig. 1.3. These materials are generally n-type and forming p-type material is very difficult. The most famous and possibly most important of these is ZnO with a very low conduction band edge and large bandgap that puts $E_{FS}$ very far from the valence band edge. Tremendous effort has been put into discovering a method of reliable p-type doping for this material, so far without success. An extreme counter example is diamond (marked C on Fig. 1.3), which can be doped p-type but is very difficult to dope n-type due to the extremely high position of the conduction band edge relative to $E_{FS}$. It's so high, close to the vacuum level, that it's actually off the top edge of the diagram and is not shown.[c]

Fig. 1.8a shows the band offsets of ZnSe and ZnTe relative to vacuum with the position of $E_{FS}$ marked. This pair of seemingly similar materials can serve as an illustrative example. The diagram shows the maximum achieved Fermi level through doping (red dashed lines) corresponding

[c] In fact, there are reports in the literature of negative electron affinity diamond meaning the conduction band edge is *above* the vacuum level, e.g. [64, 65].

generally with the empirically observed limits $E_{Fmax}$ and $E_{Fmin}$ across many materials. The upper limit is well within the conduction band for ZnSe as it is easily doped heavily n-type, though very difficult to dope p-type, consistent with the lower limit being well above the valence band edge. The upper limit for ZnTe on the other hand is below the conduction band edge, and the lower limit reaches well into the valence band; indeed this material typically exhibits p-type conductivity.

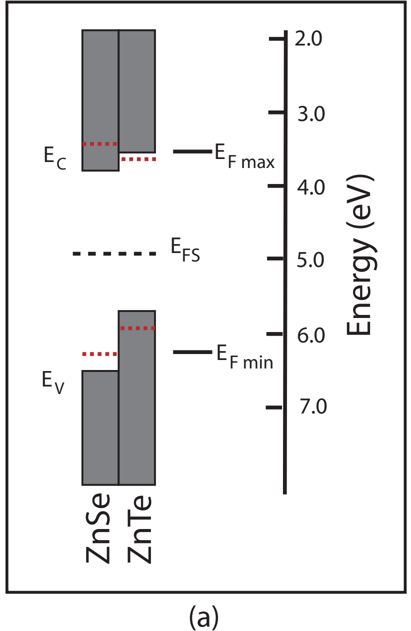


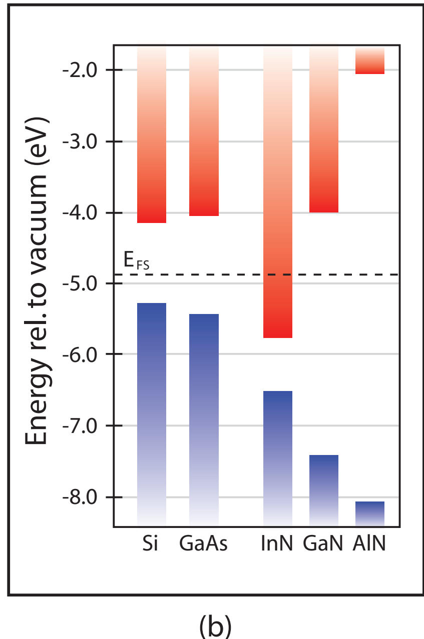


**Figure 1.8** Conduction and valence band positions of several semiconductors relative to vacuum and the universal energy reference $E_{FS}$ (black dashed) adapted from reference [33]. In (a) the approximate limits of the Fermi level position achieved in each material by doping are indicated (red dashed) along with the empirically observed limits to how far the Fermi level can be moved above and below $E_{FS}$ across many group II-VI materials, $E_{Fmax}$ and $E_{Fmin}$ respectively. In (b) the nitride materials are shown alongside the more common semiconductors Si and GaAs.

In the group III-N system, Mg is well known to act as an acceptor in GaN and p-type material can be formed, though achieving very high free hole concentrations can be difficult because of the relatively large hole binding energy. Examining now Fig. 1.8b, one sees that, if the Fermi level can be moved low enough in GaN to produce p-type material, then it should be even easier in InN, which has a valence band 0.5 to 1 eV closer to $E_{FS}$ [29–31]. However, developing p-type InN has in fact not been easy. According to this qualitative analysis with the ADM, it does not appear to be an intrinsic problem with doping limits. Instead, it will be shown that the difficulty is not in obtaining p-type material, but in properly observing the p-type conductivity using electrical measurements.

### 1.3.2 Evidence for p-type InN

The primary problem with observing p-type conductivity in InN is the existence of an inversion layer of n-type material in the very near surface region. Recalling from the previous discussion of electron accumulation at the surface of n-type InN, the Fermi level in p-type material is similarly pinned near $E_{FS}$ well above the conduction band at the surface. This results in massive band

bending in the near surface region and a thin layer of n-type material. Fig. 1.9 shows calculations of (a) the carrier concentration showing accumulation of electrons and depletion of holes, and (b) the associated band bending in the near surface region of a p-type InN sample in which the Fermi level $E_F$ is pinned ∼0.9 eV above the conduction band edge at the surface [66].

The usual method of determining the majority carrier type in semiconductors is to perform a simple Hall effect measurement in which a current must be passed through the material perpendicular to a magnetic field and the sign of the potential in the third perpendicular direction due to the Lorentz force gives the majority carrier type [67–69]. Such measurements on Mg-doped InN show all samples to be n-type. One hypothesis is that the surface inversion layer is separated from the bulk of the film by an insulating depletion layer such that Hall measurements are dominated by electron transport [70]. The idea is that the depletion layer largely prevents the electric field from penetrating into the bulk of the film so that there is no hole current; then Hall measurements, even in p-type samples, are dominated by electron flow in the surface and interface layers and return a result of "n-type."

An alternative hypothesis is simply that the conductivity of the p-type region is very low relative to the n-type region(s), either due to low hole concentration or low hole mobility, or both. If the depletion layer does not provide junction isolation and both the n- and p-type regions contribute in parallel to electrical conduction, then low conductivity of the p-type layer could prevent it from being detected by a Hall effect measurement. To date, characterization of free hole concentration and mobility in p-type InN have been very challenging, so it is difficult to confirm which hypothesis is correct [71, 72]. However, there are hints that the second hypothesis may be correct. The possibility of very low hole mobility is reasonable, given that the hole mass is expected to be ∼10x larger than the electron mass [73]. Thermopower measurements (discussed below) seem to be sensitive to bulk transport even though direct contact to p-type material is not made [74]. Some Hall effect/conductivity studies have reported observing hole transport in some form or another, again with surface contacts only [71, 75, 76]. There are reports from other materials systems, such as HgCdTe, that junction isolation can be poor due to electrically conducting threading dislocations, which act to short the junction; threading dislocation density in InN is extremely high, and the position of $E_{FS}$ would imply that dislocations may be donors and therefore be conducting, which is supported by recent calculations [39, 49–52, 77–84]. The question of junction isolation, as well as the challenge of quantifying the hole concentration and mobility, will be addressed in chapters 2 and 3.

With Hall effect measurements complicated by the surface inversion layer, other techniques were employed to search for evidence for p-type InN. Capacitance-voltage measurements are a common way of investigating doping in semiconductor devices within the depletion region of a p-n junction or Schottky contact. Due to the highly degenerate surface of InN:Mg films, all metals form Ohmic contacts, but an electrolyte can be used to form a blocking contact over a range of a few Volts. Electrolyte based capacitance-voltage (ECV) measurements have been used successfully to observe the presence of ionized, negatively charged acceptors in Mg-doped InN [70, 85–88].

Fig. 1.10 shows a Mott-Schottky plot ($1/C^2$ vs. $V$) for an undoped InN sample, one Mg-doped InN sample, and one Mg-doped In-rich InGaN sample. The slope of the Mott-Schottky plot is inversely proportional to the space charge concentration, and increasing the voltage from negative to positive (for this reference) reduces the band bending at the surface, reducing the electron accumulation and pushing the depletion layer deeper below the sample surface. Examining the undoped sample, the low slope at negative voltages corresponds to the high carrier concentration of the surface accumulation layer. Then the slope becomes very steep near +0.5 V as depletion

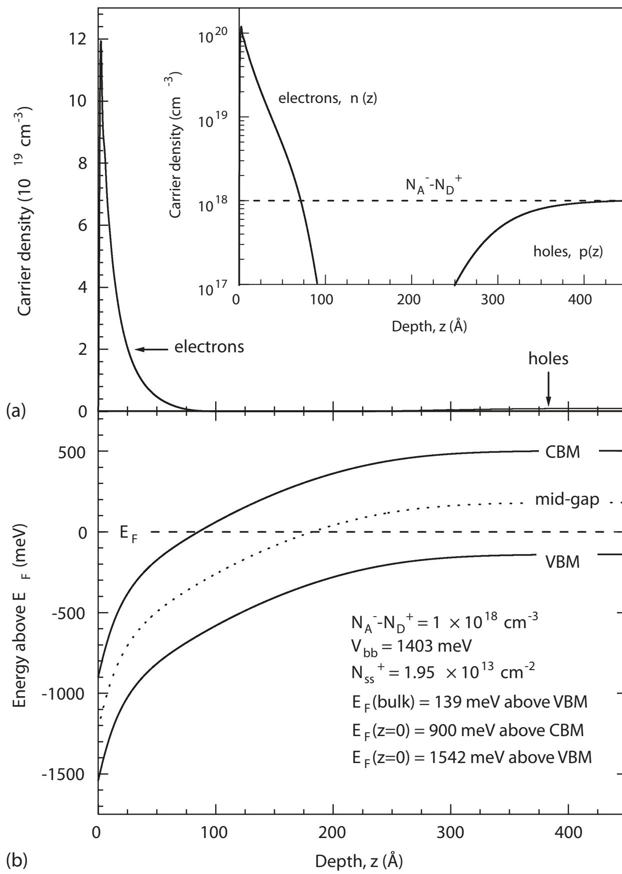


**Figure 1.9** Calculated diagram of (a) the carrier concentration showing accumulation of electrons and depletion of holes, and (b) the associated band bending in the near surface region of a p-type InN sample. Figure from reference [66].

begins to sample the much lower carrier concentration of the bulk. The Mg-doped samples are very similar until eventually the slope completely changes sign, which is evidence that negatively charged, ionized acceptors exist below the surface layer (Mott-Schottky curves for n-type samples will eventually "turn over" as well, but at higher voltages; see reference [85] for discussion).

This is very strong evidence that these Mg-doped samples are in fact p-type in the bulk below the thin inversion layer. However, there are two drawbacks to this measurement: 1) this is not a bulk measurement and in fact only the region within ∼10 nm of the surface is probed with this technique, and 2) this measurement is only sensitive to space charge and does not actually measure free carriers (holes) below the inversion layer but only ionized acceptors. This strongly suggests evidence of p-type conductivity, but to prove it would require a transport measurement of free holes.

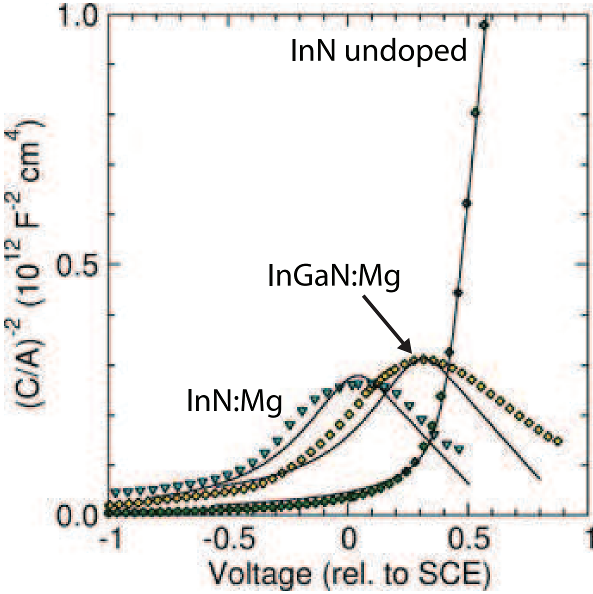


**Figure 1.10** Mott-Schottky plot for undoped InN, InN:Mg, and In-rich InGaN:Mg. Slope inversion at moderate positive voltages is evidence of a net concentration of ionized acceptors below the surface inversion layer of Mg-doped samples. Figure adapted from reference [88].

Where traditional Hall effect measurements have failed, special variations of this technique have been used to extract information from the films. Borrowing from the success of ECV measurements it was recognized that the surface inversion layer could be modulated with an electrolyte. Thus, electrolyte-gated Hall effect measurements were performed, showing that indeed the surface layer could be depleted, though the carrier type remained $n$ since the interfacial inversion layer could not be depleted [89]. The results were consistent with a bulk p-type film with thin surface and interface inversion layers. Another technique, known as variable magnetic field Hall effect, is capable of detecting multiple "species" of carriers with different mobilities in a parallel conduction geometry. This technique was applied successfully to p-type HgCdTe in which there is typically an n-type conducting layer on the surface making traditional Hall effect measurements with a single magnetic field difficult [90]. Applied to Mg-doped InN this technique reportedly detects the presence of both electrons and holes [75]. However, this technique involves a complicated treatment of the data called "quantitative mobility spectrum analysis" (QMSA), requires very high fields not widely available,

and is not practically capable of sensing carriers with low mobility due to the necessity that the square of the product of the mobility and magnetic field $(\mu B)^2$ be at least unity or preferably larger for unambiguous results [71]. This means that to observe carriers of mobility 10 $cm^2/Vs$ requires a magnetic field of 1000 Tesla while the highest pulsed fields available at special facilities are of the order of only 100 Tesla.[d]

A much simpler and more widely used technique for determining majority carrier type known as "hot probe" was shown to be able to qualitatively distinguish between n-type and p-type In-rich InGaN samples [92]. This technique relies on the Seebeck effect, which is characterized by a potential that develops in the presence of an applied temperature gradient [93, 94]. The polarity of this potential is indicative of the type of charged carriers dominating the transport; a negative potential is measured at the cold end of an n-type material and positive for p-type material as discussed in more detail in section 1.3.3. Given the qualitative success of this technique by Matthews *et al.* [92] with In-rich InGaN:Mg, accurate, quantitative measurement of the Seebeck coefficient was recognized as a possible way to characterize hole transport and confirm p-type conductivity in Mg-doped InN, which is covered in Chapter 2.

### 1.3.3 The case for thermopower

The Seebeck effect is a well known phenomenon in solid-state physics. It is the basis for the ubiquitous "thermocouple" devices for measuring temperature in which two different metals are joined and the difference in thermoelectric potential between them produces a very accurate measure of temperature. The Seebeck effect was discovered in metals by Thomas Johann Seebeck in the 1820s and has been used to characterize semiconductors since the early days of Si and Ge work at Bell Labs and Purdue University [95, 96]. Fig. 1.11 shows measured and calculated thermopower data from Geballe and Hull reported in 1955 [96]. Note the difference in the sign of the Seebeck coefficient for p-type and n-type samples. For more information and discussion of thermoelectric effects and devices, please refer to Appendix A. For the case of p-type InN, the primary advantage of a thermopower measurement over a traditional Hall effect measurement is that transport is induced through a temperature gradient, which pervades equally through the entire bulk of the sample while in a Hall effect measurement current flows due to an applied electric field (potential gradient), which does not pervade equally through the entire bulk of the sample due to inhomogeneities in the conductivity. In the case of a very highly conductive surface n-type layer and a less conductive p-type layer separated by an insulating depletion layer at the p-n junction, most of the potential drops in the conductive surface layer only and very little of the electric field penetrates into the bulk of the sample. Thus, there is comparatively little hole transport in such a geometry, and the Hall effect measurements are dominated by electron transport in the surface inversion layer.

Several important aspects of the thermopower can be understood by examining a simple equation describing the process. A more general form will be discussed later in section 2.1, but for simplicity's sake the nondegenerate approximation is discussed here. In the relaxation time approximation if the relaxation time $\tau$ is assumed to follow a power law with the energy of the carrier such that $\tau \sim \varepsilon^r$, the Seebeck coefficient of a nondegenerate n-type semiconductor is given by the

[d]The National High Magnetic Field Laboratory operates the world record non-pulsed magnet at 45 Tesla and the world record multi-shot pulsed magnet at 100 Tesla. There are pulsed magnets with higher fields, but they destroy themselves in the process since they are not structurally capable of withstanding the forces they generate, and are thus termed "single-shot" pulsed magnets [91].

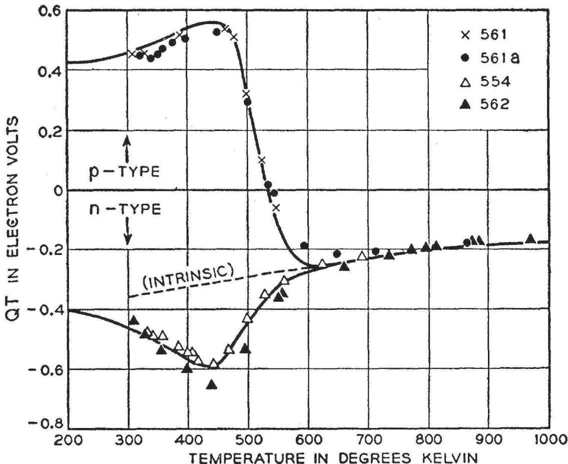


**Figure 1.11** Measured and calculated thermopower data for n-type and p-type Si from Geballe and Hull [96]. Here the Seebeck coefficient is $Q$ and the data are plotted as the Seebeck coefficient multiplied by the temperature $QT$, which is also known as the Peltier coefficient. Note that p-type Si has a positive Seebeck coefficient, and n-type Si has a negative coefficient. At higher temperatures the intrinsic carrier concentration becomes greater than the extrinsic concentrations and the curves merge into one described by ambipolar conduction, where the sign depends on the relative mobilities of electrons and holes.

following relation

$$S_{\text{nondegen}} = \frac{-k_{\text{B}}}{e}\left(r + \frac{5}{2} + \frac{E_C - E_F}{k_{\text{B}}T}\right) \tag{1.3}$$

where $k_{\text{B}}$ is the Boltzmann constant, $e$ is the elementary electron charge, $T$ is the temperature, $E_C$ is the conduction band edge, and $E_F$ is the Fermi energy. The constant $r$ depends on the dominant scattering mechanism taking on values from -1/2 for acoustic phonon scattering to 3/2 for ionized impurity scattering [97]. The $E_C - E_F$ term is the separation between the Fermi energy and the conduction band edge and is often the largest term in the equation. For example, the Fermi level in Si with an electron concentration $10^{16}$ cm$^{-3}$ at room temperature is about $8k_{\text{B}}T$ below the conduction band edge. The sum of terms inside the parentheses is then positive and the Seebeck coefficient for n-type materials is negative. For p-type materials the $E_C - E_F$ term is replaced by $E_F - E_V$, and the negative sign in front of the equation is removed so that the Seebeck coefficient is positive [94].

Since the Fermi level moves closer to the band edge with increasing extrinsic carrier concentrations, the thermopower is larger for materials with lower carrier concentration. Also, the thermopower is larger for materials with larger effective mass since increasing the mass increases the density of states and a greater separation between the Fermi level and band edge is required for the same carrier concentration in a material with a higher density of states. Both of these aspects favor detection of holes in the bulk rather than electrons at the surface of p-type InN since the electron concentration in the inversion layer is likely to be significantly larger than the bulk hole concentration and since the hole effective mass in InN is predicted to be on the order of 10 times larger than the electron effective mass [66, 73]. It will also be shown that parallel conduction models are appropriate for InN, and that in these the contributions from different layers to the total

thermoelectric response are weighted by their conductance $n\mu$ or $p\mu$, whereas in the Hall effect the layers' contributions are weighed by $n\mu^2$ or $p\mu^2$. Thus, thermopower measurements are inherently more sensitive to layers with lower mobility carriers (the holes) than are Hall effect measurements.

# Chapter 2

# Mg-doping in InN

## 2.1 Background and theory

The role of Mg as an acceptor in InN has been investigated extensively [14]. Research efforts have focused on Mg because this has been the most successful acceptor in GaN. Doping with other acceptors, such as Be and Zn, has been attempted but reports in the literature are very sparse and to date all efforts have been unsuccessful [98, 99].[a] Due to the high-conductivity, metallic surface accumulation layer and inherent low mobility of holes in InN, Hall effect results are dominated by electron conduction even in p-type films [70, 74]. For this reason, alternative techniques such as ECV and thermopower have been employed, which are more sensitive to the existence of ionizable acceptors and free hole conduction in InN, respectively [74, 83, 87, 88]. This chapter illustrates how these techniques have been used to understand the role of Mg and effects of Mg doping on p-type conductivity in InN.[b]

### 2.1.1 Seebeck coefficient theory

In the relaxation time approximation, the thermopower of electrons (an analogous expression holds for holes) can be written as follows

$$S = \frac{-k_{\mathrm{B}}}{e}\left(\frac{\langle \mu_k \varepsilon / k_{\mathrm{B}}T\rangle}{\langle \mu_k \rangle} - \frac{\zeta}{k_{\mathrm{B}}T}\right) \tag{2.1}$$

where $\mu_k$ is the $k$-dependent mobility defined below, $\varepsilon$ is the electron energy, and $\zeta$ is the Fermi energy defined to be zero at the conduction band edge [93, 100–102]. Because of the nonparabolic band structure of InN, the mobility $\mu_k$ differs from the mobility of parabolic bands and is defined as $\mu_k = e\tau_m/m_k^*$ where $\tau_m$ is the momentum relaxation time and $m_k$ is the $k$-dependent "momentum effective mass" $m^*(k) = \frac{\hbar^2 k}{dE_C(k)/dk}$ where $E_C(k)$ is the conduction band dispersion relation. The thermal averages in the first term of Eq. (2.1) as a function of reduced energy $x = \varepsilon/k_{\mathrm{B}}T$ are

[a] However, historically a "p-type" Hall effect response has been the only criterion used to evaluate the effectiveness of p-type doping. Given what is now known about Mg doping including results reported herein, i.e., even p-type films still exhibit an "n-type" Hall effect response, the use of alternative acceptors is worth reevaluating using ECV and thermopower directly and Hall effect and PL indirectly as guides.

[b] Early results with Cornell and UCSB films are presented here. A similar trend is observed in samples from Ritsumeikan University, as discussed later in Chapter 3.

defined as

$$\langle \mu(x) \rangle = \int_0^\infty -\frac{\partial f_o(x,\eta)}{\partial x} \mu(x) k^3(x) dx \tag{2.2}$$

where $f_o$ is the Fermi-Dirac distribution for the reduced Fermi energy $\eta = \zeta / k_\mathrm{B}T$ and $k(x)$ is the wavevector, which for electrons in InN follows a nonparabolic dispersion relation. Initial work with n-InN comparing electron concentrations obtained using Eq. (2.1) and 300 K measurements of $S$ with those from Hall effect have found good agreement [103]. Using Eq. (2.1), the thermopower of n- and p-type InN can be calculated as a function of carrier concentration as shown in Fig. 2.1. In this calculation we assume a nonparabolic conduction band with a band-edge electron effective mass of 0.065 $m_o$ and a parabolic valence band with hole effective mass of 0.64 $m_o$ and consider only elastic scattering by assuming an energy power law dependence of the relaxation times of carriers ($\tau = A\varepsilon^r$) where $r = 1$ (as in reference [43]). More detailed calculations of $S$ for n-InN including both inelastic and elastic scattering are disussed in Chapter 4.

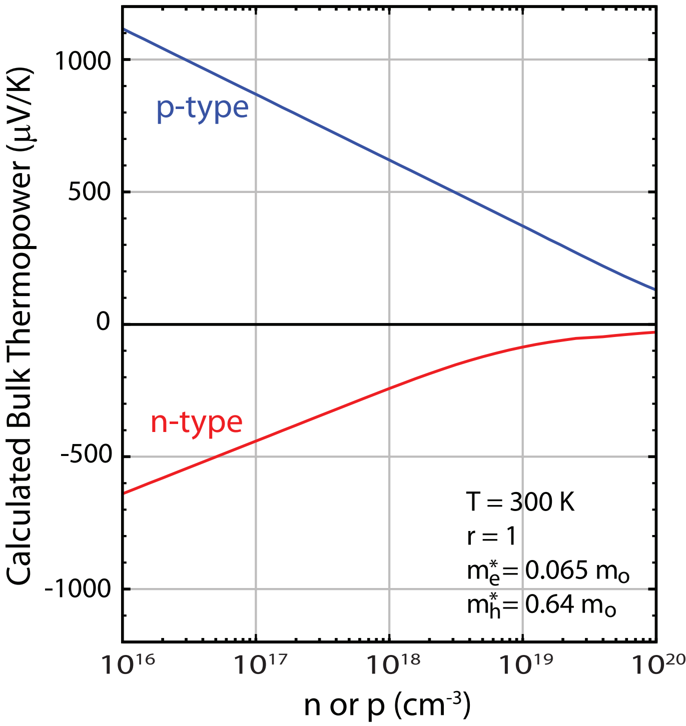


**Figure 2.1** Calculated carrier concentration dependence of the thermopower at 300 K of n- and p-type InN using Eq. (2.1).

Equation (2.1) can be used to calculate the temperature dependence of $S$ given that the carrier concentration and dominant scattering mechanisms are known. However, for strongly degenerate semiconductors, equation (2.1) reduces to the following relation [93],

$$S_{Degenerate} = -\frac{k_B}{e}(r + 3/2)\frac{\pi^2}{3}\frac{k_B T}{\zeta} \tag{2.3}$$

where the terms have the same meaning as above. This form of the equation shows clearly that the Seebeck coefficient follows a simple linear temperature dependence for metallically doped semicon-

ductors.

### 2.1.2 Parallel conduction model

The calculations of section 2.1.1 are for homogeneous layers but, as discussed in Chapter 1, surface Fermi level pinning creates a metallic electron accumulation layer on n-type films and an n-type surface inversion layer on p-type films as shown schematically in Fig. 2.2. In addition, buffer or substrate layers under the InN films could also play a role.

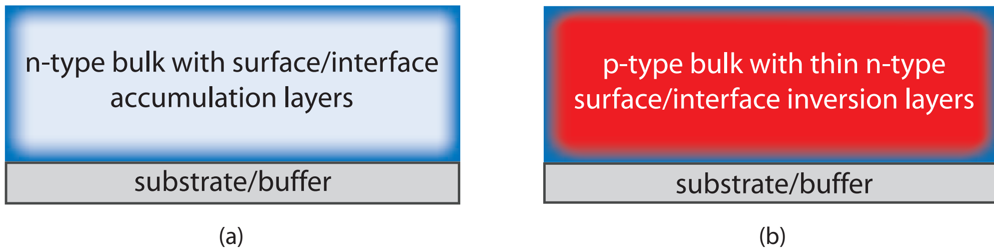


**Figure 2.2** (a) Illustration of n-type InN with surface and interface accumulation layers (blue), (b) illustration of p-type InN with p-type bulk (red) and surface/interface inversion layers (blue). The inversion and accumulation layer thicknesses are exaggerated here; in reality the surface layers are on the order of 10 nm thick while the films are on the order of 0.5 to 1 $\mu$m thick.

The geometry of these experiments, in which thermopower is measured parallel to a shallow p-n junction, is uncommon, but has been considered before in the work of Baars *et al.* on HgCdTe (MCT) photodetectors and very recently in the work of Wagener *et al.* on p-type InAs [104–106]. The p-InAs study is especially relevant here given that InAs has defect properties similar to InN; the Fermi level is pinned above the conduction band edge at the surface, leading to surface inversion on p-type films and surface electron accumulation on n-type films [106–110]. In both the studies, a parallel conduction model is used to explain the observed thermopower of samples with buried p-n junctions parallel to the transport direction.

Baars *et al.* use a parallel conduction model in which the observed Seebeck coefficient is given by a sum of the conductance-weighted-thermopower of each layer; for $j$ layers

$$S_{Observed} = \sum_j S_j \frac{\sigma_j d_j}{\sigma_T d_T} \tag{2.4}$$

where the total conductivity $\sigma_T = \sum_j \sigma_j \frac{d_j}{d_T}$ and the total thickness $d_T = \sum_j d_j$. In this approach all layers contribute to the observed thermopower as if connected in parallel. Since the thermopower of the thin surface inversion layer on p-InAs is very small in comparison to the bulk, Wagener *et al.* employ an approximation of this approach in which the observed Seebeck coefficient is simply given by the conductance-weighted-thermopower of the bulk: $S_{Observed} = S_{Bulk} \frac{\sigma_{Bulk} d_{Bulk}}{\sigma_T d_T}$.

In principle, potentials developed in the p-type bulk of the sample should be independent of those in the surface layer given that the two regions are separated by an insulating depletion layer. However, in the cases considered here, the junction isolation is not ideal. For example, MCT diodes can have a significant shunt current path provided by conducting dislocations [77, 78], and both InAs and InN thin films are typically grown on substrates for which there is a large lattice mismatch, leading to the formation of high dislocation densities. There is evidence that dislocations

act as donors and may indeed act as junction shunts in these materials as well, providing a plausible explanation for why the depletion region fails to fully isolate the p-type bulk from the n-type surface layer [39, 49–52, 79–84]. In this model then, it must be assumed that charge carriers are able to freely cross the pn junction, or at least encounter only a small barrier, such that potentials are able to equilibrate between the various layers. The exact way in which this happens is not yet understood although finite element modeling is underway that may provide the answers [111].

It should be noted that any conducting layer, including buffer/substrate layers, will contribute to the thermopower of the sample. This is especially important when searching for p-type InN using thermopower measurements where the contribution of a conductive, n-type buffer layer could mask the positive thermopower of a p-type InN film. In this data set, however, the contribution from substrate/buffer layers is assumed to be negligible because the films are grown on insulating GaN.

## 2.2 Experimental methods

InN thin-film samples from Cornell University and the University of California - Santa Barbara (UCSB) were used for this work. The samples from Cornell were grown by plasma assisted molecular beam epitaxy (PAMBE) on c-sapphire substrates using AlN nucleation and GaN buffer layers [19, 112]. The samples from UCSB were grown by the same method on semi-insulating GaN commercial templates using ∼100 nm thick undoped GaN buffer layers [113, 114]. The composition and thickness of the films were determined by Rutherford Backscattering Spectrometry (RBS) measurements. RBS results show that all of the films are stoichiometric (within an accuracy of ∼3%). Channeling RBS (c-RBS) found minimum surface channeling yields of $<8\%$, indicative of single crystal epitaxial films. The Mg content was measured by secondary ion mass spectrometry (SIMS) using Mg-implanted InN as a calibration standard.

For electrical and thermoelectric measurements, samples were cut into 5 mm × 10 mm rectangles and In foil was pressed on to form Ohmic contacts. Thermopower (Seebeck coefficient) measurements were performed in the lateral gradient geometry by measuring the voltage that develops across a sample when a temperature gradient is applied. The Seebeck coefficient $S$ is given by the ratio $\Delta V/\Delta T$, where the deltas on voltage $V$ and temperature $T$ signify the difference between the values at the two ends of the sample. A more detailed description of the thermopower measurement system and procedure has been reported previously [87]. Hall effect measurements were performed with a 3000 Gauss magnet and In contacts in the van der Pauw configuration. Electrolyte-based capacitance voltage (ECV) measurements were performed with a Biorad ECV profiler using 1.0 M NaOH as the electrolyte. More details of our ECV procedures and analysis methods are reported elsewhere [70, 87, 88]. Photoluminescence (PL) measurements were performed using a SPEX 1680 0.22 m double grating spectrometer and either a Ge, InSb, or InGaAs photodiode detector cooled to 77 K. PL spectra were corrected for instrument response using a calibrated lamp. The 515 nm line of an Ar ion laser was used as the excitation source, and PL was collected in the backscattering geometry. Samples were cooled to ∼25 K using a closed-cycle He cryostat.

## 2.3 Electrical and thermoelectric measurements

### 2.3.1 Results

The measurement results for all the Mg-doped InN films are summarized in Table 2.1, and the Seebeck coefficients measured from ∼150 to 300 K are shown in Fig. 2.3a. Positive Seebeck coefficients are observed at room temperature for three of the samples (one sample has a positive $S$ at lower temperature). Because the Seebeck effect requires *moving* charge, this proves that there are positively charged carriers (holes) in the films and that they are mobile, findings not easily obtained by other characterization techniques as discussed in Chapter 1. The range of room temperature Seebeck coefficients for all the samples extends from +868 to -206 $\mu$V/K; negative values indicate that electron transport is dominant.

| Sample | Thickness (nm) | Mg (cm$^{-3}$) | $S$ ($\mu$V/K) | $[n]$ (cm$^{-2}$) | $\mu$ (cm$^2$/Vs) |
|---|---|---|---|---|---|
| GS1548 | 445 | $4\times10^{19}$ | -54 | $9.8\times10^{13}$ | 22 |
| GS1547 | 480 | $2\times10^{19}$ | -27 | $9.7\times10^{13}$ | 42 |
| GS1810 | 450 | $6\times10^{18}$ | 74 | $1.2\times10^{14}$ | 25 |
| GS1650 | 1290 | $8\times10^{18}$ | 386 | $2.0\times10^{14}$ | 11 |
| 101107A | 820 | $2\times10^{18}$ | 868 | $2.9\times10^{14}$ | 18 |
| 101107B | 925 | $3\times10^{17}$ | -2 | $1.2\times10^{14}$ | 264 |
| 101107C | 950 | $3\times10^{16}$ | -206 | $4.0\times10^{13}$ | 1554 |

**Table 2.1** Summary of electrical and thermoelectric data for Mg-doped InN at room temperature as measured by SIMS, Hall effect, and thermopower measurements. Sheet electron concentrations are reported since the presence of parallel conducting layers precludes a quantitative measurement of the bulk carrier concentration in some samples. Note that although some of these films are p-type, the sign of the Hall coefficient is still negative in all cases, and the Hall properties listed here cannot be interpreted as measurements of free holes.

The room temperature Seebeck coefficient as a function of Mg content measured by SIMS is shown in Fig. 2.3b. The Seebeck coefficient depends non-monotonically on the Mg content of the film. Over the range of Mg concentrations in this study, $S$ is first negative, then increases with increasing Mg content to a large positive value, then eventually decreases to negative values again, implying that there is a "window" of Mg content that leads to p-type conductivity.

ECV data for the Mg-doped InN samples studied here are shown in Fig. 2.4. The dashed line is a guide for the eye showing that the peak shifts to lower applied bias for samples with Mg concentration above some threshold, which corresponds well with the transition from negative to positive thermopower.

### 2.3.2 Discussion

Too little Mg or too much can lead to n-type conductivity, consistent with reports based on ECV measurements that a Mg concentration in the range $\sim 10^{18}$ to $\sim 10^{20}$ cm$^{-3}$ results in a net-concentration of acceptors ($N_A - N_D > 0$) but a Mg concentration outside this range results in a net-concentration of donors in InN [86]. These stages are illustrated in Fig. 2.2. Undoped films, or those with Mg concentration less than $\sim 3 \times 10^{17}$ cm$^{-3}$, are n-type throughout with a surface accumulation layer as shown in Fig. 2.2a. With sufficient Mg doping, $\gtrsim 3 \times 10^{17}$ cm$^{-3}$, the

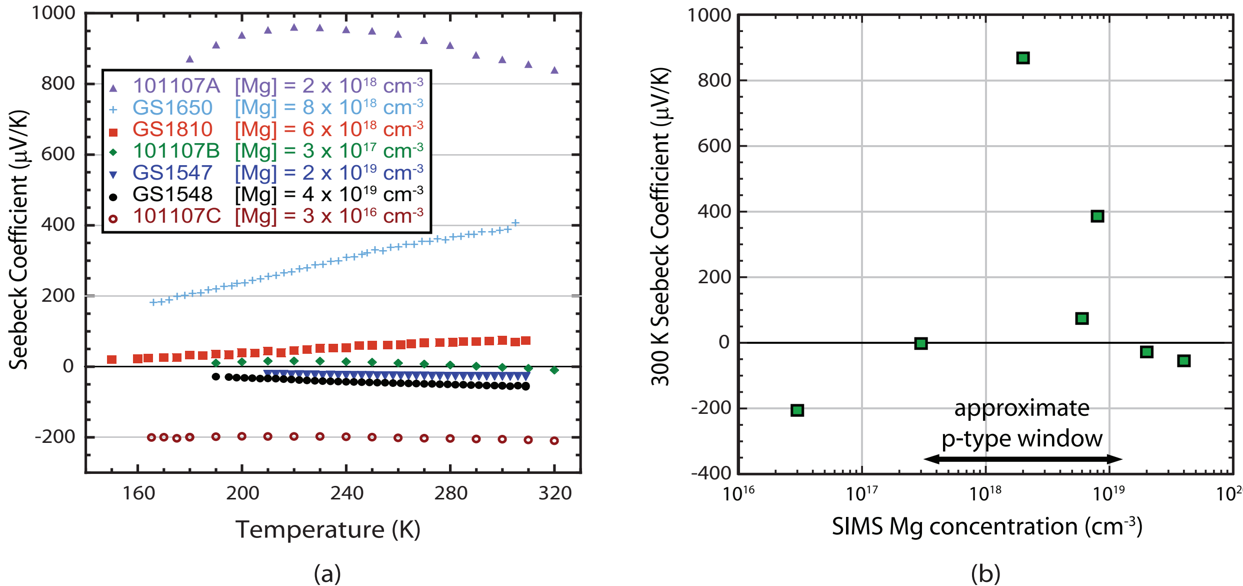


**Figure 2.3** a) Measured Seebeck coefficient of Mg-doped InN samples as a function of temperature. SIMS Mg content shown in legend. b) Measured Seebeck coefficient of Mg-doped InN samples at room temperature as a function of the Mg concentration measured by SIMS.

films become p-type in the bulk but retain the surface and interface inversion layers as shown in Fig. 2.2b. With too much Mg doping (high $10^{18}$ cm$^{-3}$ range) compensating donors[c] begin to form until eventually at Mg concentrations $\gtrsim 10^{20}$ cm$^{-3}$ fully n-type films result again as in Fig. 2.2a, but with higher bulk electron concentrations. Although using some of the same samples, a similar window of positive Seebeck coefficients has been observed recently by Dmowski *et al.* [76]. A similar trend in Mg doping is evident in the thermopower measurements of Nanishi *et al.*, which are unpublished as yet, but will be discussed later in Chapter 3.

The Mg-doping trend shown in Fig. 2.3b is consistent with the ECV and Hall data. Recent experimental and theoretical reports on ECV measurements of Mg-doped InN have shown that the voltage at which the minimum capacitance occurs (maximum in $C^{-2}$ vs. $V$ "Mott-Schottky" plots) is indicative of the net charge type (donor or acceptor) beneath the surface inversion/accumulation layer [85, 86]. This "turnover" occurs at lower applied bias in samples with a net-concentration of acceptors below the surface, and at higher applied bias in samples with a net-concentration of donors below the surface. Examining Fig. 2.4, one sees that the films with Mg concentration $\geq 2 \times 10^{18}$ cm$^{-3}$ all show slope inversion at lower bias voltages, consistent with a net-concentration of acceptors below the surface. The samples with Mg concentration $\leq 3 \times 10^{17}$ cm$^{-3}$ exhibit curves that turn over at relatively higher bias, similar to the n-type, undoped sample also shown for reference in Fig. 2.4.

In the work of Wang *et al.*, the turnover voltage returns to higher voltages for the heaviest Mg-doped films indicating a return to fully n-type material, which is not observed in this study, presumably because the highest Mg content film in this study ($[Mg] = 4 \times 10^{19}$ cm$^{-3}$) is below the threshold for complete donor compensation reported to be $\sim 10^{20}$ cm$^{-3}$ [86]. The ECV results of samples studied here show that there is still a net-concentration of acceptors in the near

[c]The identity of these donors will be discussed later on.

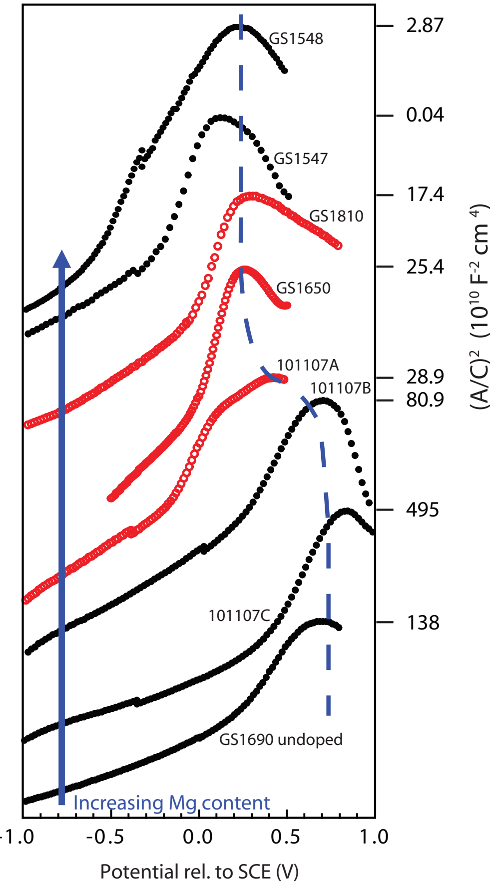


**Figure 2.4** Mott-Schottky plot (area divided by capacitance, the quantity squared vs. voltage, plotted here as potential relative to a standard calomel electrode (SCE)) showing all of the Mg-doped samples and one undoped sample (GS1690, $n = 1.2 \times 10^{18}$ cm$^{-3}$) for reference. The curves are each plotted on their own log scale and vertically offset for clarity; the hashes on the right hand side mark the maximum for each curve. Samples with positive (negative) Seebeck coefficients at room temperature are shown in red (black) with open (closed) symbols. The blue dashed line is a guide for the eye.

surface region for the samples with highest Mg content but do not rule out the possibility of a net-concentration of donors, and therefore regions of n-type conductivity, deeper within the films.

Considering the experimental data as a whole, we can make conclusions about the Mg doping dependence. Incorporation of too little Mg fails to overcome the background electron concentration $n_{min}$, which is typically $\sim 3 \times 10^{17}$ cm$^{-3}$ in InN, resulting in n-type conductivity with increased compensation. This assertion is corroborated by the electrical and thermoelectric data shown in Table 2.1; sample 101107C with Mg concentration below $n_{min}$ is a partially compensated film with low (for InN) carrier concentration, high mobility, and large negative Seebeck coefficient, but sample 101107B with Mg concentration approaching $n_{min}$ is closely compensated with greater carrier concentration, much lower mobility, and near-zero room temperature Seebeck coefficient. For samples with more Mg, mobility is even lower, consistent with the interpretation that only surface electron transport is contributing to the Hall effect results as discussed previously in chapter 1 [70].

The incorporation of Mg at $\gtrsim 10^{19}$ cm$^{-3}$ results again in InN films with negative $S$, indicating dominant electron transport. There are several possible sources of compensating donors in InN films with high Mg concentrations. In GaN, overdoping with Mg has been shown to produce donors and reduce the free hole concentration; this result has been attributed to the formation of compensating defect complexes (such as Mg-$V_N$) [115, 116] and pyramidal inversion domains [117, 118]. TEM studies of Mg-doped InN, InGaN, and GaN have shown that high levels of Mg result in large densities of planar extended defects, which could also be contributing to the n-type conductivity of overdoped films [119–122].

With two notable exceptions, the temperature dependence of $|S|$ plotted in Fig. 2.3a is generally linear and decreasing with decreasing temperature, consistent with metallically doped semiconductor behavior as discussed in section 2.1.1. However, the two samples with Mg content at or slightly above $n_{min}$, samples 101107A and 101107B, do have nonlinear $S$ vs. $T$ curves. The Seebeck coefficient of sample 101107B is slightly negative at room temperature but crosses through zero and becomes positive below ~280 K, only to reach a maximum at ~220 K before decreasing again. Similarly, the Seebeck coefficient of sample 101107A increases upon cooling, reaches a maximum near 220 K, then decreases upon further cooling. With contributions to the observed Seebeck coefficient coming from both n-type and p-type conducting regions, this temperature dependence may be analyzed in terms of the parallel conduction model of section 2.1.2. In n-type samples, variable temperature Hall effect measurements have shown that electron concentration is nearly temperature invariant; mobility also often depends weakly on temperature except in samples with very low electron concentrations, which exhibit the typical inverted U-shape due to phonon scattering and ionized impurity scattering at high and low temperatures, respectively [51, 83, 84, 123]. If the electron mobility in n-type regions were increasing over this temperature range it would be expected to decrease the observed Seebeck coefficient rather than increase it. Thus, the temperature dependence of the Seebeck coefficient observed in these two samples likely reflects changes in hole conductivity rather than electron conductivity.

Using Eq. (2.4) and the Seebeck coefficients estimated in section 2.1, the competing contributions of electron and hole conducting layers can be evaluated. In an otherwise bulk p-type InN sample, as in the case shown in Fig. 2.2b, similar, highly degenerate n-type inversion layers are expected on the surface as well as at the InN/substrate or InN/buffer-layer interface [40, 44–48]. Because these layers are degenerate ($n \sim 10^{20}$ cm$^{-3}$) [45, 48], their Seebeck coefficients are on the order of tens of $\mu$V/K as shown in Fig. 2.1. And due to their close proximity to the surface, mobility of inversion-layer carriers is expected to be low; if single-field Hall measurements of p-type samples are indeed dominated by inversion/interface electron transport, then conductivity is on the

order of only 1-10 ($\Omega$-cm)$^{-1}$. For comparison, the bulk p-type free hole concentration is likely lower ($p \sim 10^{17} - 10^{19}$ cm$^{-3}$), yielding larger Seebeck coefficients (~400-800 $\mu$V/K) as shown in Fig. 2.1, and hole mobility has been estimated in the range of 17 to 36 cm$^2$/Vs [71]. Now examining Eq. (2.4) and considering further the factor of ~100 difference in thickness between the inversion layers and the bulk p-type material, it is clear that very bulk-like positive Seebeck coefficients are expected when the only electron transport contribution comes from inversion layers. This effect is easily illustrated with an example: a 500 nm thick p-type film with free hole concentration $p = 10^{18}$ cm$^{-3}$ and hole mobility $\mu_h = 30$ cm$^2$/Vs would have a Seebeck coefficient of approximately +600 $\mu$V/K, but adding the contribution of converting 10 nm of this film to n-type material with conductivity 10 ($\Omega$-cm)$^{-1}$ and $S = -40$ $\mu$V/K only reduces the observed Seebeck coefficient to $S_{Observed} \simeq 574$ $\mu$V/K or within 96% of the bulk value. And indeed, large, positive Seebeck coefficients, similar to those predicted by theory, are measured for samples 101107A and GS1650 which have Mg doping in the "window" range.

In contrast, the samples with more Mg (e.g. GS1547 and GS1548) have small, negative Seebeck coefficients, suggesting an electron contribution in addition to that of the inversion layers to explain the apparent dominance of n-type conductivity in the thermopower measurements. In fact it has been shown for sample GS1548 (the Mg-doped sample of reference [89]) that even when the surface inversion layer is depleted with an electrolyte, a n-type Hall effect is still measured with a sheet concentration of $\sim 10^{14}$ cm$^{-2}$. This indicates the presence of a thicker layer of n-type conducting material, likely due to the combined effects of self-compensation and increased extended defect density with large Mg concentrations as well as interface-related charge [48, 124]. Using Eq. (2.4), we note that the contribution of a thicker, more conductive bulk-like n-type layer, in addition to the inversion layers and the bulk p-type layer, can drastically reduce the observed Seebeck coefficient. This effect is readily illustrated with another example: a 500 nm thick p-type film with free hole concentration $p = 10^{18}$ cm$^{-3}$ and hole mobility $\mu_h = 30$ cm$^2$/Vs would have a Seebeck coefficient of approximately +600 $\mu$V/K, but adding the contribution of just 30 nm of n-type material with free electron concentration $n = 10^{19}$ cm$^{-3}$, electron mobility $\mu_e = 300$ cm$^2$/Vs, and $S = -100$ $\mu$V/K is enough to reduce the observed Seebeck coefficient to negative values ($S_{Observed} \simeq -5$ $\mu$V/K in this case).

Thus, parallel conduction modeling of Mg-doped InN samples is consistent with thermopower, Hall effect, and capacitance-voltage measurements and electrolyte-gated Hall results reported in reference [89]. This modeling shows that the contribution of inversion layers alone to the observed Seebeck coefficient can be minor, but the presence of high conductivity n-type material in excess of the normal inversion layers can substantially reduce the observed Seebeck coefficient, even to negative values, with only a fraction of the total film thickness represented as n-type material.

## 2.4 Photoluminescence

### 2.4.1 Mg doping dependence

Using a Ge detector, which has high absolute sensitivity but limited spectral response below 0.65 eV, photoluminescence is observed only from the two samples with the lowest Mg concentration (101107C and 101107B).[d] Switching to a less sensitive InGaAs detector extends the range well into

[d]Because the spectral response of Ge detectors cuts off sharply at the bandgap energy of ~0.67 eV, broad PL peaks with peak energies < 0.67 eV (peak wavelengths > 1800 nm) may appear as false peaks centered near ~1600 nm. Therefore, this detector is often not suitable for assessing the lineshape or position of PL from InN.

the near infrared and reveals a PL signal from 101107A as well, though with ∼1000x lower intensity than 101107B, as shown in Fig. 2.5. The overall trend, no matter what detector is used, is that the PL signal decreases rapidly with increased Mg doping, consistent with previous reports of PL being quenched by Mg doping [75, 125, 126]. A plausible interpretation of this behavior is that trap states in the bulk of the film are emptied as the Fermi level drops, opening nonradiative recombination paths for the photoexcited carriers. This view is supported indirectly by the observation that PL is quenched for Mg concentrations roughly greater than or equal to the residual donor concentration [75, 125]. This view is also supported by the recovery of PL in InN:Mg by irradiation sufficient to compensate the free hole concentration [70].

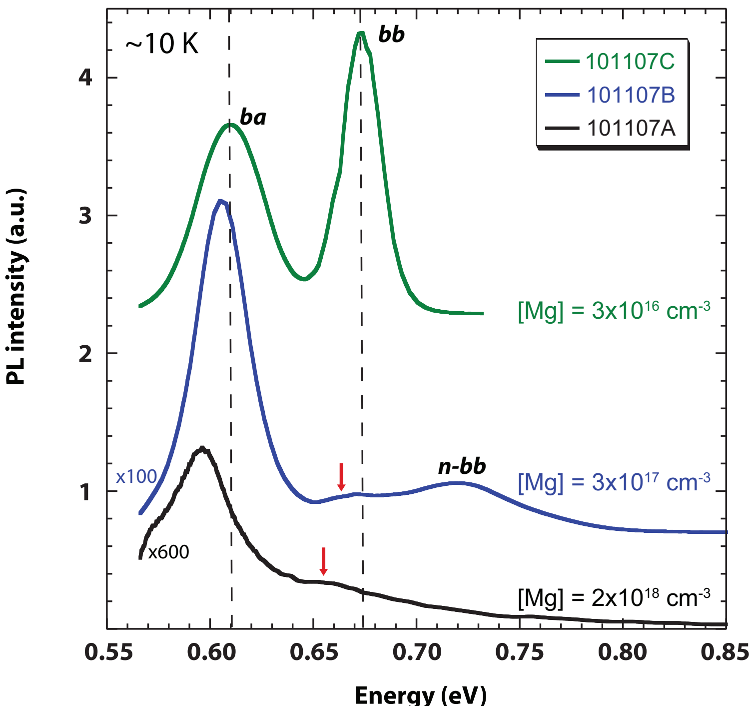


**Figure 2.5** Photoluminescence spectra at ∼10 K of samples 101107A ($S_{300\text{ K}} = +868$ $\mu$V/K), 101107B ($S_{300\text{ K}} = -2$ $\mu$V/K), and 101107C ($S_{300\text{ K}} = -206$ $\mu$V/K), using an excitation intensity of ∼56 mW and an InGaAs detector (vertically offset for clarity). The SIMS-measured Mg concentrations are shown. The dashed lines are guides for the eye and the red arrows mark the positions of the *bb* peak found by fitting (see text).

For sample 101107C, an n-type sample with the lowest Mg content, two PL peaks are clearly resolved, one near the InN bandgap energy at 673 meV, which is attributed to band-to-band transitions (labeled *bb*), and one at 610 meV attributed to band-to-acceptor transitions (labeled *ba*). The logic behind these peak assignments will be discussed in more detail below. As shown in Fig. 2.5, increasing Mg content results in several significant changes to the PL spectra in addition to the decreasing PL intensity discussed above. The band-to-band emission peak dramatically shrinks in intensity relative to the band-to-acceptor peak, likely due to the increasing density of states at the Mg acceptor level. Also, both the *ba* and *bb* peaks shift to lower energies by ∼15 meV with increasing Mg content, possibly reflecting the dropping Fermi level and emptying of the conduction band, which leads finally to emission from the conduction band minimum rather than from a

distribution of energies between the conduction band minimum and the Fermi level.[e] As the *bb* peak becomes smaller it is more difficult to resolve, but its position is marked by the red arrows in Fig. 2.5, which are found by fitting the PL spectra with a summation of Gaussian peaks. An example of this fitting is shown in Fig. 2.6 for sample 101107B in which three Gaussian curves are summed to reproduce the full PL spectrum, resulting in a very good fit to experimental data. In this sample, the third peak that appears at higher energy, marked as *n-bb*, is attributed to band-to-band emission from n-type areas of the film with greater defect concentration. PL emission energy is known to increase with electron concentration in InN due to conduction band filling (discussed previously along with the Burstein-Moss effect in section 1.2.1) [14]. Recalling from section 2.3, this sample is very closely compensated with a room temperature Seebeck coefficient near zero due to competing contributions from n-type and p-type regions of the film, which is consistent with the PL spectrum.

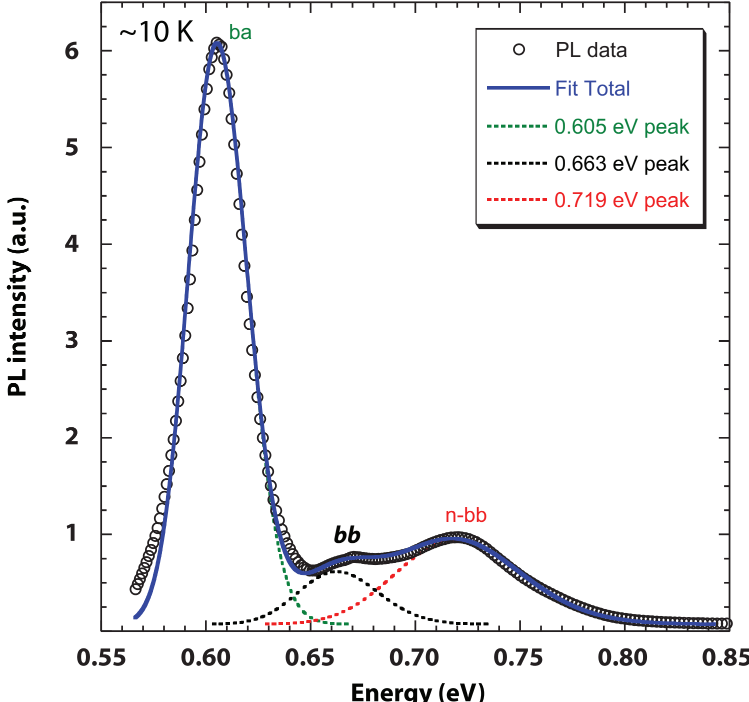


**Figure 2.6** Photoluminescence spectra at ~10 K of sample 101107B ($S_{300\ \mathrm{K}} = -2\ \mu\mathrm{V/K}$), using an excitation intensity of ~56 mW and an InGaAs detector. Three peaks are identified: one associated with band-to-band emission (bb), one with band-to-acceptor transitions (ba), and a third (n-bb) associated with residual n-type material with high electron concentration as explained in the text.

### 2.4.2 Mg ionization energy

In all the PL spectra, but most clearly resolved in the PL of 101107C, there is one peak near the InN band gap energy at ~0.66 eV (*bb*) and one ~60-70 meV lower in energy (*ba*), as discussed

[e] Another possible interpretation is that the energy shift is due to the increasing Mg level density of states, which shifts the quasi Fermi level of the photoexcited holes to slightly higher energy. Simple modeling of band filling could help to answer this question.

above. Table 2.2 shows a summary of the PL peak energies of the three samples near the transition from n-type to p-type conductivity, as indicated by the Seebeck coefficient. In this table the peak energies are derived from the PL spectra by Gaussian fitting, as shown in Fig. 2.6. This section will show that, to first order, the ionization energy of the Mg acceptor is given by the difference between the *bb* and *ba* peaks, which is listed in Table 2.2 as $E_{Mg}$. Note that although the peaks shift in energy with increasing Mg content, no systematic change in $E_{Mg}$ is observed. This is consistent with the interpretation from above that the lowest energy peak corresponds to band-to-acceptor emission and as the Fermi level shifts down, the energy of electrons decreases, thereby decreasing the energy of the PL peaks; the peak separation is dictated by the separation between the acceptor energy level and the valence band maximum, which is unaffected by the changing Fermi level. Averaging the values obtained with the InGaAs detector, gives a value of 61 meV for $E_{Mg}$. For the one PL spectrum, sample 101107C, that was observable with the InSb detector, the peak separation is somewhat larger at 69 meV, although the reason for this is not well understood. Due to limited data from the InSb detector and differing measurement conditions, the value of $E_{Mg}$ derived from the InGaAs detector is given precedence.

| Sample | Mg ($cm^{-3}$) | $S_{300K}$ ($\mu$V/K) | $E_{ba}$ (meV) | $E_{bb}$ (meV) | $E_{n-bb}$ (meV) | $E_{Mg}$ (meV) |
|---|---|---|---|---|---|---|
| 101107C | $3\times10^{16}$ | -206 | 610 [603]* | 673 [672]* | – | 63 [69]* |
| 101107B | $3\times10^{17}$ | -2 | 605 | 663 | 719 | 58 |
| 101107A | $2\times10^{18}$ | +868 | 594 | 655 | – | 61 |

* Data in square brackets [ ] measured with an InSb detector at ∼25 K.

**Table 2.2** Summary of PL peak energies and the derived Mg ionization energy, $E_{Mg}$, as explained in the text. Except where noted otherwise, all data recorded at ∼10 K with an InGaAs photodiode detector and ∼56 mW excitation intensity.

In the literature, a Mg-related peak, in addition to band-to-band emission, has been observed in PL spectra of InN films grown by both MBE and metal organic chemical vapor deposition; in both cases the Mg-related peak appeared at an energy ∼60 meV below the band-to-band emission and was interpreted as emission from band-edge electrons recombining with holes at the Mg acceptor state ∼60 meV above the valence band edge [125, 126]. In another report, a single PL peak was observed in InN:Mg ∼110 meV lower than in other samples with less Mg, leading to a larger estimate of ∼110 meV for the Mg activation energy [75]. Transitions to acceptor levels have also been reported in detailed studies of PL in undoped InN [127, 128]. In the study by Arnaudov *et al.*, two PL peaks are observed, which are attributed to transitions of band-edge electrons to two different acceptor states with ionization energies of 18 meV and 85 meV, respectively. In the study by Klochikhin *et al.*, again two PL peaks are observed; the higher energy peak is attributed to a combination of band-to-band transitions and transitions of band-edge electrons to Urbach tails in the valence band and/or to a shallow acceptor with ionization energy 5-10 meV, while the lower energy peak is attributed to transitions of band-edge electrons to a deeper acceptor with ionization energy of 50-55 meV. Nearly all of these reports are consistent with a hydrogenic acceptor in InN since the hole effective mass is not well known; assuming it falls in the range $m_h^* = 0.42 - 0.7m_\circ$ and using $\varepsilon_S = 10.3$ as the static dielectric constant [63], the acceptor ionization energy is estimated to be in the range of 54-90 meV by a simple Hydrogenic model calculation.

In the context of these previous reports, the *bb* peak is attributed to band-to-band emission, while the *ba* peak is attributed to transitions of free electrons near the conduction band edge to

the Mg acceptor state located ∼61 meV above the valence band edge. Further evidence for this interpretation comes from the dependence of the relative intensities of these two peaks on pumping intensity. As shown in Fig. 2.7b, the dominant emission line at low excitation intensities is the *ba* peak; with increasing laser intensity the *bb* peak increases linearly and becomes the dominant emission line while the *ba* peak increases more slowly, in excellent agreement with the findings reported by Wang *et al.* [125]. One interpretation of this behavior, which has been observed before in both Mg-doped and undoped InN, is that the majority of photoholes are localized on acceptor sites for low laser intensity but with increasing laser intensity the photohole population increases, the quasi Fermi level of holes moves towards the valence band, and more photoholes begin to occupy delocalized valence band states, leading to increasing band-to-band emission relative to band-to-acceptor emission [125, 128].

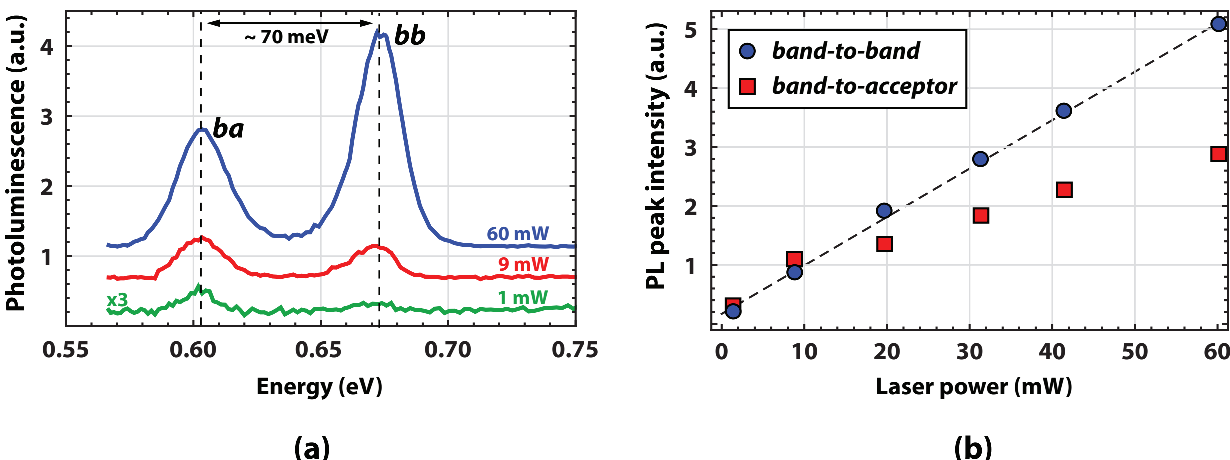


**Figure 2.7** Using an InSb detector: (a) Photoluminescence spectra at ∼25 K of the sample with the lowest Mg content, 101107C ($S_{300\text{ K}} = -206\ \mu$V/K), for several different laser excitation intensities, vertically offset for clarity. Two peaks are clearly resolved: one associated with band-to-band emission (*bb*), the other with band-to-acceptor transitions (*ba*) as explained in the text. (b) Peak PL intensity is plotted as a function of pumping laser power. The dashed line in (b) is a linear fit to the *bb* data.

## 2.5 Conclusions

Mg concentrations in a "window" from $\sim 3 \times 10^{17}$ to $\sim 1 \times 10^{19}$ cm$^{-3}$ produce p-type InN films as evidenced by a positive Seebeck coefficient. This conclusion is supported by changes in mobility observed by Hall effect and by capacitance voltage measurements, both of which are consistent with a change from surface accumulation on an n-type film to surface inversion on a p-type film. A parallel conduction path model is used to model the dependence of the observed thermopower on the properties of the films. At low Mg concentrations, two peaks are observed in photoluminescence, which are attributed to band-to-band and band-to-acceptor transitions, respectively, and an acceptor binding energy of ∼61 meV is deduced. At larger Mg concentrations, no PL is observed; this is attributed to electron trapping in deep states which become empty as the Fermi level drops below mid-gap. Direct optical measurement of these purported mid-gap states, by means of Fourier transform infrared spectroscopy (FTIR PL) or a similar technique, could provide great insight. One

is tempted to use one of the myriad deep level spectroscopy techniques to search for these states, but these require pn junctions, Schottky contacts, or resistive samples, which are still unobtainable in InN. The application of spectroscopic techniques, such as photothermal ionization spectroscopy (PTIS), to the study of the shallow acceptors in InN is also completely unexplored.

# Chapter 3

# Thermopower of parallel conducting structures

## 3.1 Background and theory

As discussed in chapter 2, the ever-presence of parallel conducting paths in InN, especially when doped effectively with acceptors, requires extra care in interpreting the results of electrical and thermoelectric measurements. In understanding the effects of Mg doping, it was necessary to take these parallel conducting paths into account, as discussed in section 2.3.2. Due firstly to the presence of inhomogeneities such as electron accumulation layers at the surface and interface with the buffer layer, even on p-type films, but secondly to the presumed presence of other n-type conducting regions in some films. Schematically, this is shown in Fig. 3.1b. One example is sample 101107B, which is very closely compensated and another example comes from the films with the highest Mg concentrations, all of which show signs of contributions from both n-type and p-type bulk-like material. To understand the properties of such films, the parallel conduction model of section 2.1.2 has proven quite useful. But more importantly, this analysis has yielded something even more useful; it has illustrated a way to quantitatively deduce the electrical properties of free holes in InN. This chapter will demonstrate the development of this method and show the experiments and analysis used to measure the free hole concentration and hole mobility in p-type InN.

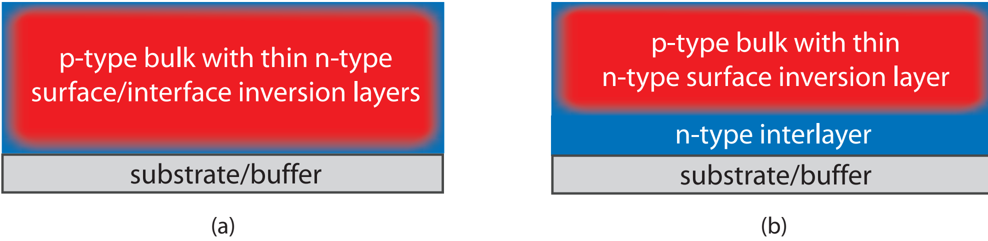


**Figure 3.1** (a) Illustration of p-type InN with p-type bulk (red) and surface/interface inversion layers (blue); (b) Illustration of p-type InN with thick, bulk-like n-type layer. The inversion layer thicknesses are exaggerated here; in reality the surface layers are on the order of 5-10 nm thick, the films are on the order of 0.5 to 1 $\mu$m thick, and the bulk-like n-type layer may be up to 100 nm thick (see text).

The examples mentioned above pose the question: how would the overall thermoelectric response of a p-type InN sample change if a layer of n-type InN were also contributing? And the answer is that it changes dramatically, as illustrated in Figs. 3.2 and 3.3, which show the results of calculations using Eq. 2.4 exploring the difference in overall thermoelectric response between films such as those depicted in Figs. 3.1a and 3.1b. Fig. 3.2 shows the results of a 3-layer parallel conduction model calculation of $S_{\mathrm{Apparent}}$ vs. n-type interlayer thickness at room temperature for several values of interlayer electron concentration; the assumed values of the total thickness $d_{\mathrm{T}}$, inversion layer thickness $d_{\mathrm{inv}}$ and conductivity $\sigma_{\mathrm{inv}}$, hole concentration $[p]$, and hole mobility $\mu_h$ are indicated in the figure. The major difference between this bulk-like n-type material and that of the inversion layers is that the electron mobility is higher; since we are considering bulk transport, the dependence of electron mobility on carrier concentration is assumed to be bulk-like as measured from undoped films [43, 129]. As shown for a wide range of electron concentrations, even a very thin layer of this high-conductivity material drastically reduces the observed Seebeck coefficient, reducing it to negative values at a thickness greater than only ∼30 nm, or only ∼6% of the total film thickness. This fraction is small due to the large disparity between electron and hole mobilities. However, it is reasonable to assume the electron mobility may be reduced in this high defect density layer, especially if it arises due to Mg overdoping or high extended defect density; this effect is simulated by the dashed lines, which show the same results with the electron mobility reduced, somewhat arbitrarily, by a factor of three. The effect is that the "crossover point" increases by a factor of ∼2.5 to just over 80 nm. Reducing electron mobility by a factor of ten rather than three (not shown) pushes the crossover to ∼200 nm.

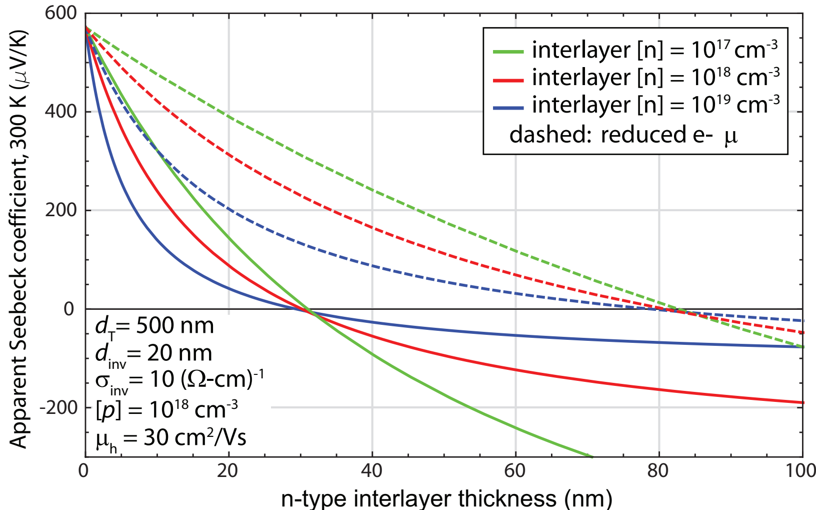


**Figure 3.2** Calculated Seebeck coefficient vs. n-type bulk layer thickness at room temperature based on a 3-layer parallel conduction model showing the effect of varying the electron concentration in the bulk-like layer for a 500 nm thick film with $10^{18}$ cm$^{-3}$, 30 cm$^2$/Vs p-type material and a 20 nm thick inversion layer with conductivity of 10 (Ω-cm)$^{-1}$. The dashed lines show the result when the electron mobility is divided by three to simulate the effects of compensation and extended defects in this part of the film.

Fig. 3.3a shows a similar calculation, although this time the electron concentration is fixed and results for a range of hole concentrations are shown. The effect of varying the bulk hole concentration is manifested most obviously in the conductance weighting (the shape of the curves),

but also affects the bulk value of the Seebeck coefficient of the p-type layer, which is the intersection of the curves on the y-axis. The crossover thickness varies greatly from tens to hundreds of nm depending on the bulk hole concentration in the p-type layer. A similar sensitivity to hole mobility also exists, which is shown in Fig. 3.3b. Here, the hole concentration is fixed at $10^{18}$ cm$^{-3}$, and the hole mobility is varied from 10-30 cm$^2$/Vs. As in Fig. 3.3a, the shape of the curves and the crossover thickness are shown to be very sensitive to the choice of hole mobility.

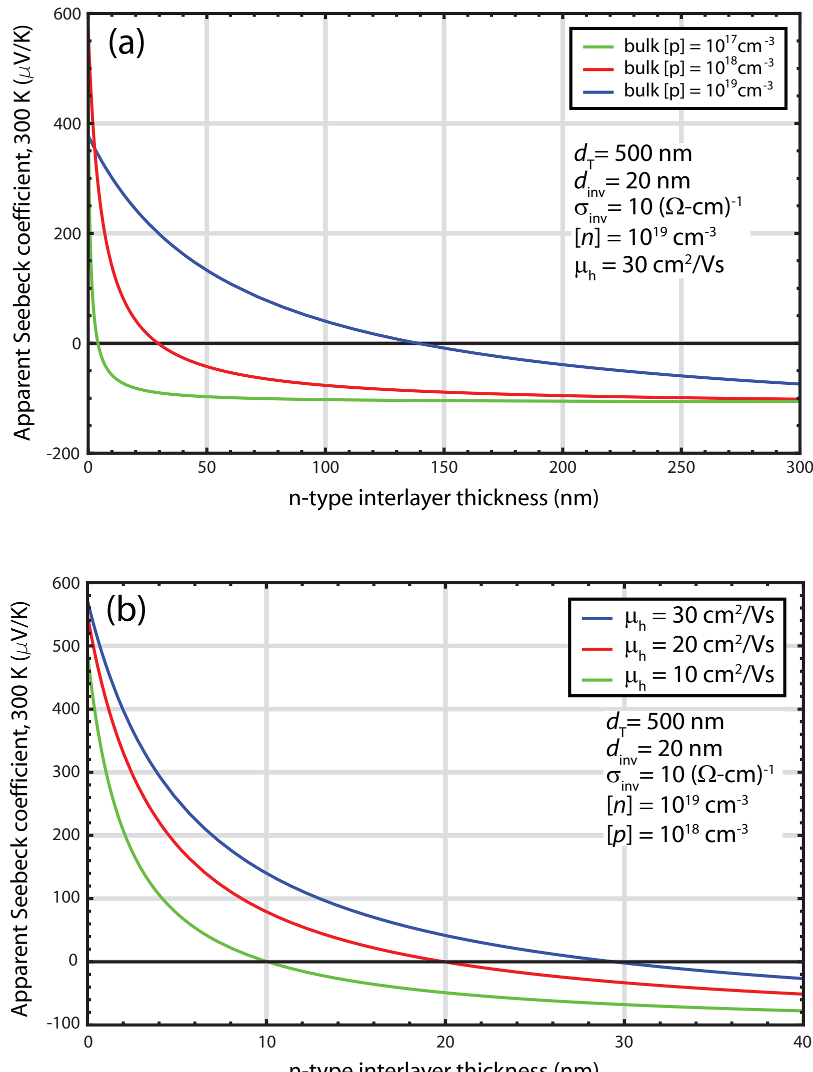


**Figure 3.3** (a) Calculated Seebeck coefficient vs. thickness of $10^{19}$ cm$^{-3}$ n-type interlayer material at room temperature based on a 3-layer parallel conduction model showing the effect of varying the bulk hole concentration for a 500 nm thick film with 30 cm$^2$/Vs hole mobility p-type material and a 20 nm thick inversion layer with conductivity of 10 $(\Omega\text{-cm})^{-1}$. (b) The same as in (a), except that the hole concentration is kept constant at $10^{18}$ cm$^{-3}$ and the hole mobility is varied from 10-30 cm$^2$/Vs.

As demonstrated, the Seebeck coefficient of such multilayered structures depends strongly on the thickness of the n-type interlayer as well as the electrical properties of the interlayer and bulk

p-type layer. To take advantage of this fact, Mg doped InN films were grown on top of undoped (n-type) InN interlayers with variable thickness. Within each series the thickness of the n-type interlayer is systematically varied while all other variables are held constant; this allows subtraction of the contribution from the interlayer and reliable determination of the electrical/thermoelectric properties of the p-type layer, including free hole concentration and mobility, as described below.

## 3.2 Undoped interlayer experiment

### 3.2.1 Mg doping dependence

In order to conduct the variable thickness interlayer experiment, growth conditions leading to p-type InN must first be established, as done previously for Cornell and UCSB grown material, since MBE growth is still highly variable from machine to machine. A series of InN films were grown by the Nanishi group, varying the Mg content by changing the temperature of the Mg effusion cell, $T_{Mg}$. Simply, the higher the temperature of the Mg cell, the greater the Mg flux and incorporated fraction of Mg. However, this relationship is highly nonlinear. As shown in Table 3.1, varying the Mg cell temperature from 150-235 °C leads to InN with Mg concentrations which vary over nearly three orders of magnitude: $2 \times 10^{17} < [\mathrm{Mg}] < 9 \times 10^{19}$ cm$^{-3}$.[a] Table 3.1 also lists a summary of thermopower and Hall data showing the effects of varying the Mg content, which are qualitatively very similar to those observed in Cornell and UCSB samples. Most importantly, the Seebeck coefficient reaches positive values at an intermediate Mg content, about which exists a limited “window” of p-type conductivity. Hall electron concentration decreases, then remains approximately constant in the window, then increases again. Hall mobility decreases precipitously near the onset of p-type conductivity. Finally, ECV measurements show the characteristic shift in the “turnover” voltage, as shown in Fig. 3.4, consistent with a shift from donors to acceptors below the surface inversion layer for intermediate Mg doping conditions.

| Sample | $d_{Mg}$ (nm) | $d_{int}$ (nm) | $T_{Mg}$ (°C) | [Mg] (cm$^{-3}$) | $S$ ($\mu$V/K) | $[n]$ (cm$^{-2}$) | $\mu$ (cm$^2$/Vs) |
|---|---|---|---|---|---|---|---|
| S600 | 500 | 60 | 150 | $2\times10^{17}$* | -167 | $8.7\times10^{13}$ | 1230 |
| S623 | 500 | 60 | 175 | $9\times10^{17}$ | -151 | $6.9\times10^{13}$ | 664 |
| S601 | 500 | 60 | 200 | $8\times10^{18}$ | +39 | $4.8\times10^{13}$ | 412 |
| S610 | 500 | 60 | 215 | $2\times10^{19}$* | +7 | $5.0\times10^{13}$ | 357 |
| S599 | 500 | 60 | 225 | $5\times10^{19}$ | -13 | $4.0\times10^{13}$ | 421 |
| S624 | 500 | 60 | 235 | $9\times10^{19}$* | -62 | $8.0\times10^{13}$ | 294 |

* This quantity by interpolation or extrapolation (see text).

**Table 3.1** Summary of electrical and thermoelectric data for Nanishi-group Mg-doped InN at room temperature as measured by Hall effect and thermopower measurements. This series illustrates the Mg doping dependence. Also shown are the thickness of the Mg-doped layer $d_{Mg}$, the thickness of the undoped interlayer $d_{int}$, the temperature of the Mg effusion cell $T_{Mg}$ during doping, and the resulting Mg concentration in the film [Mg] as measured by SIMS.

[a] The relationship between $T_{Mg}$ and [Mg] was established by growing a single sample with four distinct layers using $T_{Mg}$ = 175, 200, 225, and 250 °C, respectively. SIMS data from this sample, using a Mg-implanted InN sample as reference, shows a very nice exponential relationship: $[\mathrm{Mg}] = 2.77 \times 10^{12} e^{0.0736 T_{Mg}}$. The [Mg] for films grown with $T_{Mg}$ other than the four specifically tested values were obtained by extrapolation or interpolation of this equation. Sample-to-sample variation of [Mg] using the same $T_{Mg}$ was shown to be on the order of 15%.

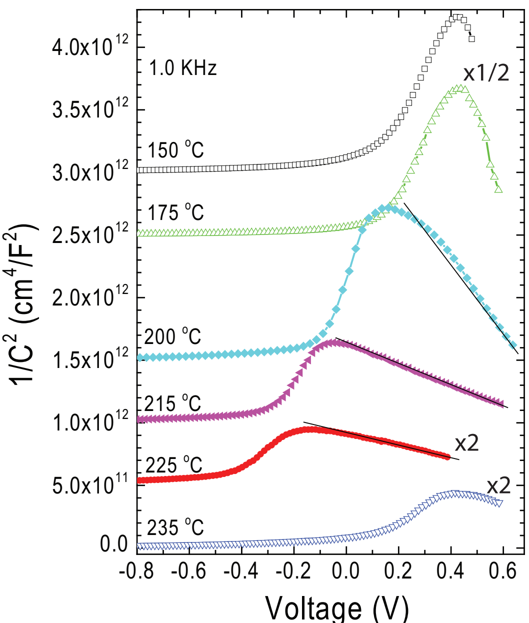


**Figure 3.4** Mott-Schottky plot showing ECV measurements of the Nanishi group Mg doping series of samples, vertically offset for clarity. The Mg cell temperature is shown for each curve. The solid lines are fits to the linear part of the curve representing ionizable acceptor concentrations from $7{\times}10^{18}$ (200 °C) to $6{\times}10^{19}$ cm$^{-3}$ (225 °C).

Fig. 3.5 shows that with increasing Mg content, the Seebeck coefficient is first large and negative, then rises sharply to positive values, then slowly decreases to small, negative values, just like with the Cornell/UCSB series. For example, compare Fig. 3.5 to Fig. 2.3b. The range of Mg doping leading to p-type conductivity seems to be wider in the Nanishi series than the Cornell/UCSB series, which could be due to differing growth conditions or impurities. However, it is premature to make a determination with the current sample set, given the effect of the undoped interlayer. An undoped interlayer is often used to improve crystalline quality of Mg-doped films by avoiding the added difficulties of Mg incorporation during the most critical, initial phase of film growth. Thus, the samples in the Mg-doping series in Table 3.1 were all grown with ~60 nm of undoped InN before opening the Mg shutter. Though it may improve crystalline quality, it also greatly affects electrical and thermoelectric properties of the films by supplying a relatively thick layer of n-type material to the films. Though we ultimately intend to use this very fact to our advantage as discussed above, this n-type interlayer alters the Seebeck coefficient to such a degree that it is difficult to determine the range of [Mg] leading to p-type conductivity. The largest Seebeck coefficient in this Mg doping series is +39 $\mu$V/K, more than a factor of 20 smaller than the largest Seebeck coefficient from the Cornell/UCSB Mg doping series, which was grown without conducting buffer layers. This effect is illustrated further in Fig. 3.5, which also shows how the Seebeck coefficient changes for a series of samples with the same Mg content, but varying interlayer thickness. This will be discussed in further detail below, but the takeaway at this moment is that the effect of the interlayer on measured Seebeck coefficient is large and must be taken into account in assessing the effectiveness of Mg doping. The best method would be to grow the Mg doping series with no interlayer to minimize contributions from n-type layers and maximize $S$. However, even with 60 nm of undoped

interlayer, positive Seebeck coefficients are observed for samples grown with $T_{\mathrm{Mg}}$ = 200 °C and 225 °C. Thus, these Mg doping levels are chosen for the variable interlayer thickness experiment.

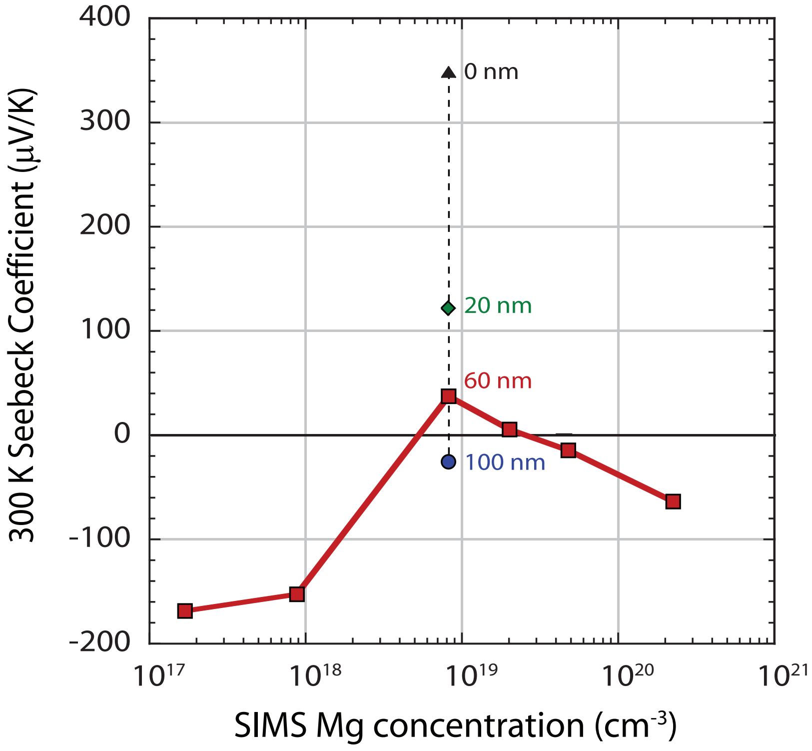


**Figure 3.5** Measured Seebeck coefficient of Nanishi-group Mg-doped InN samples at room temperature as a function of the Mg concentration measured by SIMS. The thickness of the undoped interlayer for the Mg doping series was constant at 60 nm. The Seebeck coefficient for several samples with the same Mg content but differing interlayer thickness (labeled) are also shown. The solid and dashed lines are guides for the eye.

### 3.2.2 Evaluation of free hole concentration and mobility

Table 3.2 summarizes the relevant data for the two series of samples employed in the variable interlayer thickness experiment. Samples were grown with two different Mg doping levels and within each series the thickness of the undoped interlayer $d_{\mathrm{int}}$ is varied from 0 nm to $\sim 10^2$ nm. As expected, increasing the interlayer thickness within each series rapidly reduces the measured Seebeck coefficient from a large, positive to a small, negative value as hole conduction within the p-type part of the film becomes dominated by electron conduction in the increasingly thick n-type interlayer. The reduction in the value of the Seebeck coefficient is accompanied by a factor of $\sim 3$ decrease in measured Hall carrier concentration and a factor of $\sim 10$ increase in Hall mobility. This results from increased Hall current in the n-type part of the film, but is also due to the increasing quality of the n-type layer as it gets thicker, as discussed further below.

As the parameter most sensitive to the hole conduction properties of the p-type bulk of the films, the primary focus is to model how the Seebeck coefficient changes with interlayer thickness. As shown in Figs. 3.2 and 3.3, this is a rather effective method for determining the major transport properties of the individual layers of the films for the following reasons: 1.) for $d_{\mathrm{int}} \ll d_{\mathrm{Total}}$

the Seebeck coefficient is given primarily by the bulk p-layer, which greatly constrains the free hole concentration given the known $S(p)$ relationship from section 2.1.1, 2.) as $d_{\text{int}}$ becomes large ($d_{\text{int}} \gtrsim 0.1 - 0.7 d_{\text{T}}$ depending on the relative conductivities), the Seebeck coefficient becomes dominated by the undoped interlayer, which constrains the interlayer electron concentration (again according to the known $S(n)$ relationship from section 2.1.1), 3.) for $0 < d_{\text{int}} \lesssim 0.1 - 0.7 d_{\text{Total}}$ the shape of the $S(d_{\text{int}})$ curve is determined by the relative conductivities, but since the concentrations are already constrained, this means the shape is very sensitive to the relative mobilities of interlayer electrons and p-layer holes. Some variability is expected, but there is a well known relationship between electron concentration and electron mobility in InN, so these parameters are not completely independent.

The measured Hall effect carrier concentration and mobility can also be used to constrain the open parameters, but some care must be taken in deciding how the various layers contribute to the Hall effect. Although perhaps not yet proven, evidence is mounting in favor of poor junction isolation for buried p-type layers in InN, as discussed in sections 1.3.2 and 2.1.2.[b] This would imply that even in Hall effect measurements, p-type layers can contribute to current flow in parallel. The way in which parallel conduction paths contribute to Hall effect measurements is slightly different than thermopower measurements. It has been shown that the Hall coefficient ($R_H = -\frac{1}{ne}$ or $R_H = \frac{1}{pe}$) for a multilayer structure of $j$ layers is given by the following,

$$R_{H,Apparent} = \frac{1}{\sigma_T^2 d_T} \sum_j R_{H,j} \sigma_j^2 d_j \tag{3.1}$$

where $\sigma_j$ and $d_j$ are the electrical conductivity and thickness of the individual layers, the total conductivity $\sigma_T = \sum_j \sigma_j \frac{d_j}{d_T}$, and $d_T$ is the total thickness [130–132]. A negative Hall coefficient indicates n-type transport and a positive one indicates p-type transport. In the case of ambipolar conduction or simply the existence of both n- and p-type layers, the Hall coefficient can even be zero.

[b] In the analysis to follow much better fits to the Hall data were possible assuming all layers contributed in parallel than when assuming the p-layer was junction isolated.

| Sample | $d_{\text{Mg}}$ (nm) | $d_{\text{int}}$ (nm) | $T_{\text{Mg}}$ (°C) | [Mg] (cm$^{-3}$) | $S$ ($\mu$V/K) | [$n$] (cm$^{-2}$) | $\mu$ (cm$^2$/Vs) |
|---|---|---|---|---|---|---|---|
| S665 | 500 | 0 | 200 | $8\times10^{18}$ | +350 | $9.6\times10^{13}$ | 76 |
| S696 | 500 | 20 | 200 | $8\times10^{18}$ | +123 | $5.5\times10^{13}$ | 210 |
| S601 | 500 | 60 | 200 | $8\times10^{18}$ | +39 | $4.8\times10^{13}$ | 412 |
| S697 | 500 | 100 | 200 | $8\times10^{18}$ | -24 | $3.1\times10^{13}$ | 722 |
| S625 | 500 | 0 | 225 | $5\times10^{19}$ | +249 | $12\times10^{13}$ | 19 |
| S629 | 500 | 10 | 225 | $5\times10^{19}$ | +108 | $6.5\times10^{13}$ | 80 |
| S599 | 500 | 60 | 225 | $5\times10^{19}$ | -13 | $4.0\times10^{13}$ | 421 |

**Table 3.2** Summary of electrical and thermoelectric data for Nanishi-group Mg-doped InN at room temperature as measured by Hall effect and thermopower measurements. These two series illustrate the effect of varying the n-type interlayer thickness. Also shown are the thickness of the Mg-doped layer $d_{\text{Mg}}$, the thickness of the undoped interlayer $d_{\text{int}}$, the temperature of the Mg effusion cell $T_{\text{Mg}}$ during doping, and the resulting Mg concentration in the film [Mg] as measured by SIMS.

Some rearranging shows that the properties of the individual layers are weighted by $n\mu^2$ (or $p\mu^2$) in the Hall effect while in thermopower the weighting is simply $n\mu$ (or $p\mu$). This partially explains why thermopower measurements are more sensitive to the low mobility hole conducting layers in InN than are Hall effect measurements. For a multilayer structure of known layer properties, Eq. 3.1 can be used to calculate the apparent Hall coefficient (or apparent Hall carrier concentration). Another equation based on the total conductivity can then be used to calculate the apparent Hall mobility. Since the total conductivity $\sigma_T = \sum_j \sigma_j \frac{d_j}{d_T}$ and $\sigma = n\mu e = \mu/R_H$, the equation for apparent Hall mobility is as follows,

$$\mu_{H,Apparent} = \frac{R_{H,Apparent}}{d_T} \sum_j \sigma_j d_j. \tag{3.2}$$

The thermopower, Hall coefficient, and Hall mobility can now be modeled self-consistently using Eqs. 2.4, 3.1, and 3.2, as shown in Figs. 3.6 and 3.7. This modeling is based on a three layer structure, representing the inversion, interlayer, and p-type layers, each of which has a uniform set of properties. It was found that the Hall data could not be fit well without accounting for the variation of electron concentration and mobility of the interlayer with thickness, at least on average. In this model the interlayer is assumed to have uniform properties, but those properties change based on the thickness of the layer.[c] This is consistent with numerous reports in the literature showing that the carrier concentration decreases dramatically with increasing thickness in n-type InN [51, 62, 82, 98].

Fig. 3.6 shows the effect of increasing the interlayer thickness on the measured Seebeck coefficient for the two series of samples listed in Table 3.2. In both series, an interlayer thickness of $< 100$ nm is enough to result in a negative Seebeck coefficient. The dashed lines show that excellent fits to the thermopower data are achieved using the parallel conduction model. The Seebeck coefficient fit is most sensitive to the properties of the p-type layer, the free hole concentration and mobility, which are listed in the plot for each series. These are also the parameters of primary interest. However, they are chosen in conjunction with the parameters of the inversion layer and undoped interlayer so that reasonable fits are produced for the Hall coefficient and Hall mobility as well, which are shown in Fig. 3.7. Though not quite as exact as the thermopower fit, the modeling produces reasonably good fits to the Hall data. The Hall data is quite sensitive to the properties of the interlayer, and not very sensitive to the properties of the p-layer. Better fits to the Hall data are certainly possible by including more detail into the thickness dependence of the interlayer properties, for example, but these improvements hardly affect the p-layer properties and are thus unnecessary. See the sensitivity analysis in Appendix C for more details.

The free hole concentrations extracted from the modeling process are very close to the Mg concentrations measured by SIMS, suggesting a very high activation fraction for Mg acceptors, similar to that observed previously [71]. The free hole concentrations are also comparable to the net acceptor concentrations estimated by ECV. For instance, ECV measurements of the three samples in the $T_{\mathrm{Mg}} = 225$ °C series are shown in Fig. 3.8 with fits corresponding to net acceptor concentrations in the range of 3-6$\times10^{19}$ cm$^{-3}$, very comparable to the free hole concentration of $4\times10^{19}$ cm$^{-3}$ extracted from the parallel conduction modeling. Similarly, an ECV-estimated net acceptor concentration of $7\times10^{18}$ cm$^{-3}$ for one of the $T_{\mathrm{Mg}} = 200$ °C series samples (S601) is very comparable to the free hole concentration of $9\times10^{18}$ cm$^{-3}$ extracted from the parallel conduction modeling. It should be noted that there is still considerable error in both the ECV-estimated net

[c]See Appendix C for more information on these assumptions.

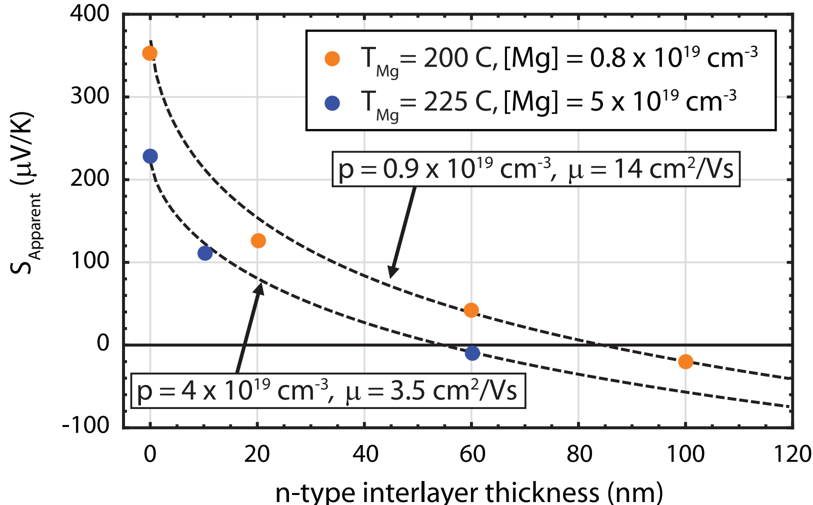


**Figure 3.6** Measured Seebeck coefficient of interlayer series samples at room temperature as a function of the undoped interlayer thickness. The Mg content for each series, as measured by SIMS, is shown in the legend. The dashed lines are calculated based on simultaneous fitting of the thermopower and Hall effect data. The free hole concentration and mobility extracted from the analysis are also shown for each series.

acceptor concentration and SIMS measurements, such that all three appear to be consistent within expected errors.

The hole mobilities extracted from the interlayer modeling process show that the mobility is lower for the sample with higher hole concentration and higher Mg content, which is to be expected for heavily doped material in which ionized impurity scattering likely limits the mobility. Mg doping has also been shown to increase structural defect density and could produce defect complexes, both of which could act as scattering centers [117–122]. There are very few estimates of hole mobility in InN with which to quantitatively compare these results. The sheet conductivity study by Wang, *et al.* estimated hole mobilities in the range of 17-36 $cm^2/Vs$ for samples with hole concentrations in the range of 1.4-3$\times10^{18}$ $cm^{-3}$, which are somewhat larger than the hole mobilities obtained here. The discrepancy could easily be due to the $\sim 10\times$ lower hole concentrations in their study. There is also an estimate of hole mobility as a minority carrier in n-type InN from a complicated optical technique known as "time-resolved transient grating spectroscopy," which reported $\mu_h = 39$ $cm^2/Vs$ [72]. Again, this is comparable but somewhat higher than our mobility, although the optical study was not really measuring the same property as the experiment described here. But based on what is known, the mobilities extracted from the interlayer modeling process seem to be consistent with the literature.

The analogous experiment, where the n-type interlayer thickness is held constant and the thickness of the p-layer is varied is currently underway. Preliminary data for this experiment are listed in Table 3.3 and plotted in Fig. 3.9. As expected, the thermopower increases with increasing thickness, reflecting the greater contribution from the p-layer as it gets thicker. The sheet Hall concentration also increases, implying that the p-layer is contributing to Hall effect measurements. However, the sheet charge only increases by $2.1 \times 10^{13}$ $cm^{-2}$ with a 900 nm increase in thickness. If the hole concentration in this layer is $4\times10^{19}$ $cm^{-3}$ as determined from the above analysis for Nanishi-grown InN:Mg with $T_{Mg} = 225$ °C, the increase in sheet charge should be $3.6 \times 10^{15}$ $cm^{-2}$, two orders of

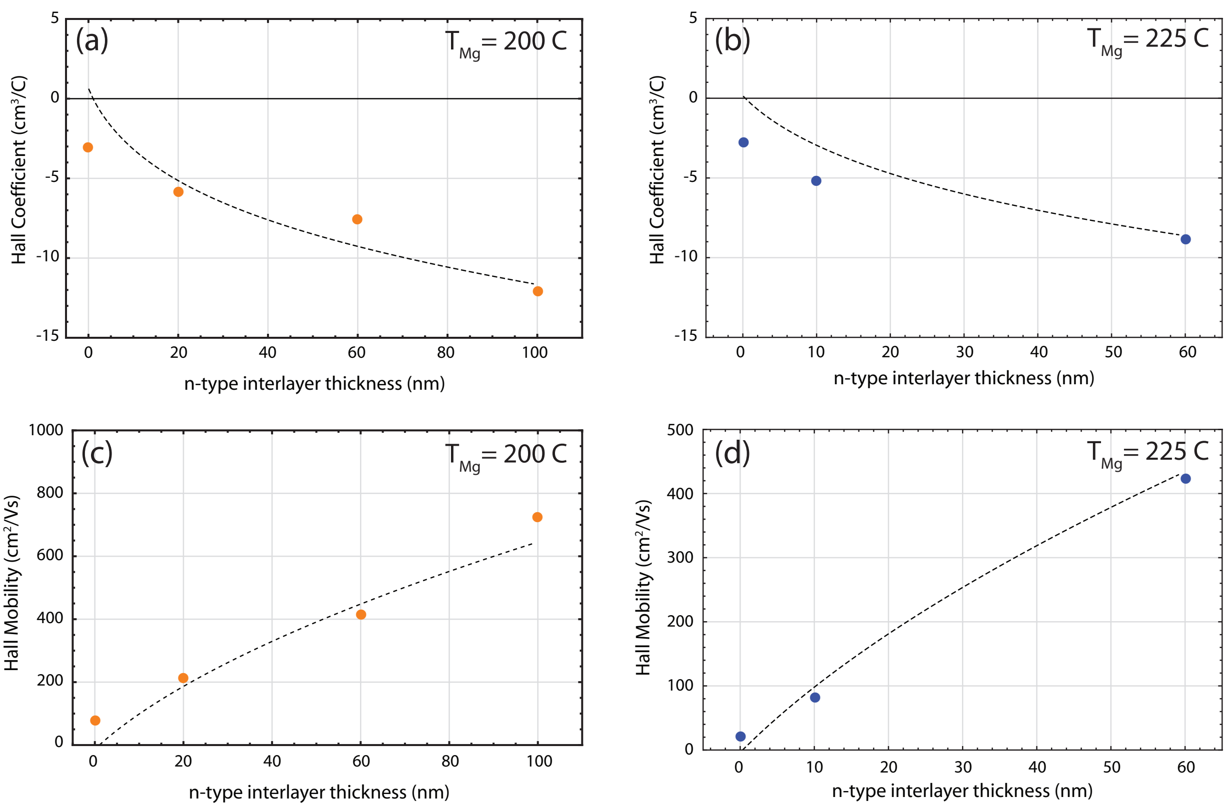


**Figure 3.7** Measured Hall coefficient and mobility of interlayer series samples at room temperature as a function of the undoped interlayer thickness. The dashed lines are calculated based on simultaneous fitting of the thermopower and Hall effect data using all the same conditions as the calculated curves in Fig. 3.6.

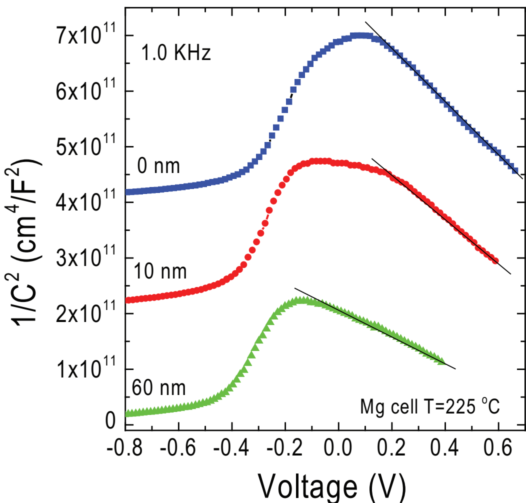


**Figure 3.8** Mott-Schottky plot showing ECV measurements of the $T_{\rm Mg}$ = 200 °C series of samples, vertically offset for clarity. The interlayer thickness is shown for each curve. The solid lines are fits to the linear part of the curve representing ionizable acceptor concentrations from 3-6×$10^{19}$ cm$^{-3}$.

magnitude larger. Clearly, the contribution of the p-layer to Hall results is still suppressed. The invariance of mobility is consistent with this interpretation as well, assuming that the Hall data comes mostly from the n-type layer that isn't changing over this set of three samples.

| Sample | $d_{\rm Mg}$ (nm) | $d_{\rm int}$ (nm) | $T_{\rm Mg}$ (°C) | [Mg] (cm$^{-3}$) | $S$ ($\mu$V/K) | [$n$] (cm$^{-2}$) | $\mu$ (cm$^2$/Vs) |
|---|---|---|---|---|---|---|---|
| S694 | 100 | 10 | 225 | 5×$10^{19}$ | +7 | 5.9×$10^{13}$ | 119 |
| S629 | 500 | 10 | 225 | 5×$10^{19}$ | +108 | 6.5×$10^{13}$ | 80 |
| S695 | 1000 | 10 | 225 | 5×$10^{19}$ | +288 | 8.0×$10^{13}$ | 82 |

**Table 3.3** Summary of electrical and thermoelectric data for Nanishi-group Mg-doped InN at room temperature as measured by Hall effect and thermopower measurements. This series illustrates the effect of varying the thickness of the p-type layer while holding the n-type interlayer thickness constant. Also shown are the thickness of the Mg-doped layer $d_{\rm Mg}$, the thickness of the undoped interlayer $d_{\rm int}$, the temperature of the Mg effusion cell $T_{\rm Mg}$ during doping, and the expected Mg concentration in the film [Mg].

In Fig. 3.9, the dashed line is calculated assuming all of the exact same parameters determined by fitting the thermopower and Hall data for the $T_{\rm Mg}$ = 225 °C interlayer series above. No new fitting has occurred, simply recalculation assuming that the interlayer is now of constant thickness while the thickness of the p-layer is changing. The transport properties of the p-layer are assumed to be constant, i.e., $[p] = 4 \times 10^{19}$ cm$^{-3}$ and $\mu_h = 3.5$ cm$^2$/Vs. This curve actually predicts almost exactly the measured value for a p-layer thickness of 100 nm, which is very near the crossover. However, the model undershoots the data point at $d_{\rm Mg}$ = 1000 nm by nearly a factor of two, as illustrated by the red arrow in the figure. The likely cause of this large discrepancy is that the transport properties of the p-layer are in fact *not* constant with thickness; the hole concentration decreases slightly and/or the hole mobility increases with thickness. This is actually not a surprising

result, given the known variation of crystalline quality and defect density in InN. Increasing mobility is easy to understand. Decreasing hole concentration is somewhat more unexpected, if one assumes that with thickness defect density and therefore compensating donor concentration decreases, the hole concentration might be expected to increase. However, perhaps the formation of stacking faults or inversion domains occurs for the thickest film, thereby increasing compensation slightly. It's also possible that Mg incorporation decreased somewhat for the thickest film, possibly due to segregation to the growing surface, which could be checked with SIMS. More data is necessary before definitive conclusions can be made, and those experiments are underway.

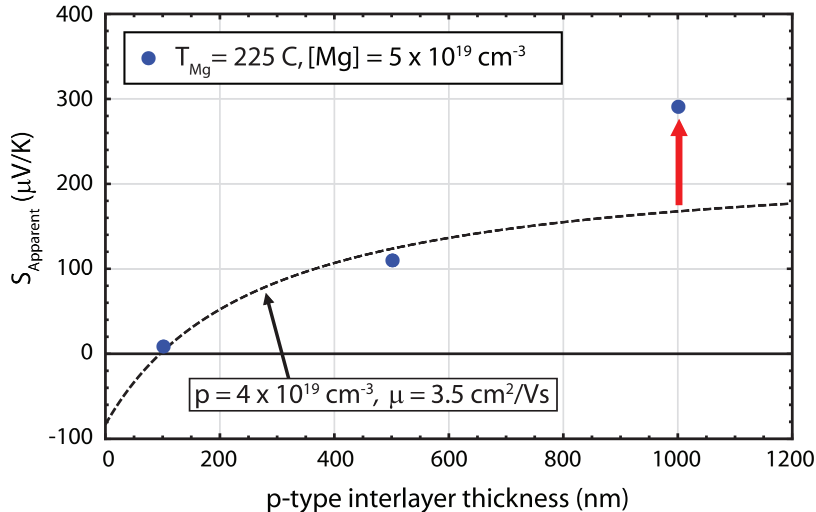


**Figure 3.9** Measured Seebeck coefficient as a function of p-layer thickness at room temperature for the sample listed in Table 3.3. The expected Mg content is shown in the legend based on the calibrated effusion cell temperature. The dashed line is calculated based on the model parameters used to fit the thermopower and Hall data for the $T_{\mathrm{Mg}} = 225$ °C interlayer series above.

## 3.3 Conclusions and future work

This interlayer experiment has illustrated the sensitivity of thermopower measurements to bulk hole transport and shown that parallel conduction modeling can be used to extract the properties of individual layers from multilayer structures. The p-layer free hole concentrations and mobilities are consistent with data from other techniques and published literature. It should be made clear however, that this analysis depends heavily on the $S(p)$ calculation, which in turn depends on the assumed hole effective mass. If the effective mass were to be refined, the values of the parameters here would change although the technique would still be valid. The analogous experiment to this one, in which the thickness of the interlayer is held constant and the thickness of the p-layer is varied, is currently underway. It may seem at first glance that this experiment is more appropriate, since the thickness of the layer of interest is being varied while all other parameters are held constant. However, this experiment may be plagued by the problem that the properties of the p-type layer are not constant with thickness. This would not be surprising given the known variation of quality of InN with thickness. In the current experiment this is avoided by the fact that the p-layer is the same thickness in all the samples. One way around this issue again would be to grow the

variable interlayer series again as described here, but with a thinner or thicker p-layer, to see if the properties of the p-layer change with thickness.

# Chapter 4

# Dislocation scattering in n-type InN

## 4.1 Background

Due to the lack of suitable growth substrates, threading dislocation (TD) densities in InN are very high, typically occurring at concentrations of $10^9 - 10^{11}$ cm$^{-2}$ as shown in Fig. 4.1. For comparison, threading dislocation densities in GaAs are typically on the order of $\sim 10^3$ cm$^{-2}$ and in homoepitaxial Si there are practically none [133]. The reason for this tremendous density of threading dislocations is lattice mismatch with the growth substrate. Although some alternatives have been investigated, the dominant substrate for group III-N materials continues to be c-sapphire, which has a 29% mismatch with InN. To aleviate this mismatch somewhat, buffer layers of AlN and/or GaN are typically used, reducing the lattice mismatch to 14% and 11%, respectively [19, 81, 134]. Still, materials with lattice mismatch greater than 4-5% cannot be grown psuedomorphically and most of the strain is accomodated through misfit dislocations [81].

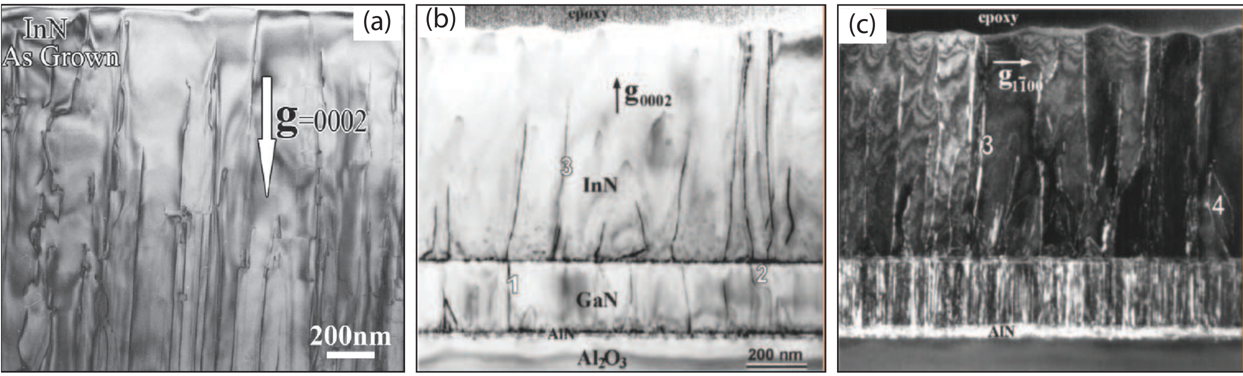


**Figure 4.1** Cross sectional TEM micrographs of typical MBE-grown InN on c-sapphire showing very high dislocation density; (a) reproduced from Ref. [135], (b) and (c) from Ref. [134]. (b) and (c) show the same area imaged in bright field and dark field, respectively, illustrating the high dislocation density in the InN film, but also in the underlying GaN and AlN buffer layers. In (b), many of the dislocations in the InN film are observed to originate in the GaN buffer layer; the density of TDs reaching the InN film surface is $2.2 \times 10^{10}$ cm$^{-2}$ and the TD density in the GaN buffer layer is approximately a factor of 10 higher.

The degree to which these dislocations limit the electrical and optical properties of InN, and ultimately any devices made from this highly dislocated material, is not yet known, but drawing

from the field's collective experience with GaN such large dislocation densities can be deleterious. Dislocations in n-GaN have been shown to be acceptors, recombination centers, and charged carrier scattering centers [133, 136–139]. Through tremendous technical effort it has been possible to reduce dislocation density in MOVPE GaN films to $< 10^7$ cm$^{-2}$ as shown in Fig. 4.2, resulting in improved LED efficiency and vastly increased laser diode lifetime [133]. With this history of GaN in mind, it becomes evident that investigating the nature of extended defects, especially the effect on transport properties, is of paramount importance to the utilization of InN in future devices.

| Sample | FWHM (PL) of near band gap PL at 10 K | TRPL (XA) | TD density | CL images 10 μm |
|---|---|---|---|---|
| Standard | < 3 meV | 80 ps | $5\times 10^8$ cm$^{-2}$ | |
| ULD | < 2 meV | 220 ps | $7\times 10^7$ cm$^{-2}$ | |
| 2S-ELO | < 1 meV | 375 ps | $5\times 10^6$ cm$^{-2}$ between stripes | |
| Free-standing | | | $1\times 10^6$ cm$^{-2}$ full wafer | |

**Figure 4.2** Comparison of threading dislocation (TD) density in thin films of MOVPE GaN grown by various techniques and the associated improvement in optical properties by examining photoluminescence (PL), time-resolved photoluminescence (TRPL), and cathodoluminescence (CL). Standard growth, so-called ultra low dislocation (ULD), two-step epitaxial lateral overgrowth (2S-ELO), and a free standing wafer are shown. Reproduced from Ref. [133].

First, let us review what is known about dislocations in InN. Similar to GaN, correlation between cathodoluminescence (CL) intensity and threading dislocations has been observed, leading to the conclusion that dislocations act as nonradiative recombination centers in InN [140]. Since optical properties are affected, it's possible that electrical properties are affected as well, raising the question of how dislocations affect the local band structure. Although developed for point defects, a simple extension of the amphoteric defect model to dislocations leads to the assertion that the Fermi level is pinned at dislocations similar to surfaces, in which case they would be expected to accumulate electrons and act like metallic wires, as shown schematically in Fig. 4.3a. This kind of scenario is also supported by recent calculations, which report that the Fermi level is pinned as much as 0.6 eV above the conduction band minimum at edge-type dislocations [39]. In this configuration, edge-type dislocations would act as donors; a view supported by several reports of correlation between dislocation density and electron concentration in InN [49–52]. There is at least one report to the

contrary, Ref. [56], although they do conclude that dislocations are scattering centers. This report is consistent with this author's view that dislocations need not always be the dominant source of carriers in order to be charged and act as scattering centers. There is still considerable debate in the literature about *the* source of the unintentional background electron concentration, including among them native point defects, impurities such as O and H, and dislocations, although it seems perfectly reasonable at this point that there is no single source; there are many possible donors in InN and from sample-to-sample different sources may dominate. Given the defect properties of InN it is very likely that dislocations are in fact donors, and if so, then they would be positively charged and therefore act as strong scattering centers for electrons and holes as in Fig. 4.3b, significantly affecting the mobility as will be shown.

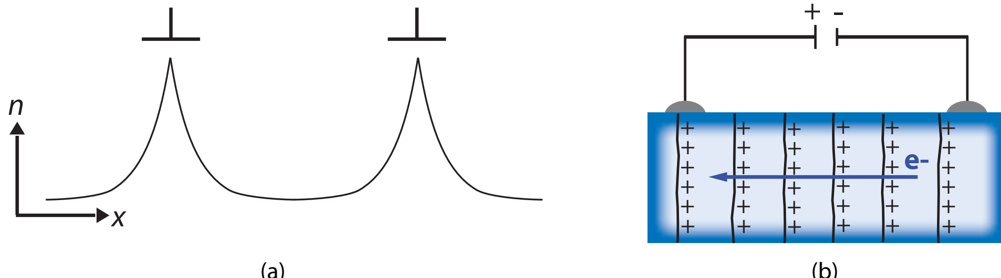


**Figure 4.3** (a) Schematic diagram showing variation of electron concentration ($n$) as a function of distance ($x$) in the vicinity of threading dislocation cores ($\perp$) in InN. (b) Schematic of electrons traveling within the plane of an InN film (cross sectional view), encountering lines of positive charge at threading dislocations.

For instance, the Monte Carlo simulations by Yu and Liang show that mobility is dramatically reduced for dislocation density above $\sim 10^9$ cm$^{-2}$, as shown in Fig. 4.4a, and dislocation scattering affects the temperature dependence of mobility [54]. These results perhaps help to explain the discrepancy between calculated and measured mobility, especially regarding temperature dependence, but there is little comparison to experiment and dislocations are assumed to be acceptors in their analysis rather than donors.[a] The discrepancy between calculated and measured mobility typically observed (in this case ignoring dislocation scattering) is illustrated in Figs. 4.4b and 4.4c [53, 123]. In Fig. 4.4c a compensation ratio $\Theta = 0.2$ is invoked to increase the effect of ionized impurity (Coulomb) scattering and improve the fit to experiment, but a similar effect could be achieved by adding dislocation scattering, which is simply a different kind of Coulomb scattering (charged line rather than charged point). This issue will be discussed more below.

The first work on charged dislocation scattering in GaN was done by Look and Sizelove [136], demonstrating that not only does their charged dislocation scattering model give near perfect agreement to temperature dependent Hall data, but also resolves several apparent paradoxes observed in GaN transport studies. Thus the existence of charged dislocation scattering in GaN is accepted, however, dislocation scattering is not typically an issue in commercial devices since GaN films for such purposes are intentionally grown with low dislocation density to reduce their detrimental

[a]This is actually quite common in the older literature on InN, where any unknowns in InN were assumed to be the same as in its sister compound GaN. Dislocations in GaN were known to be acceptor-like in n-type material and scatter carriers at high densities [136, 137, 141].

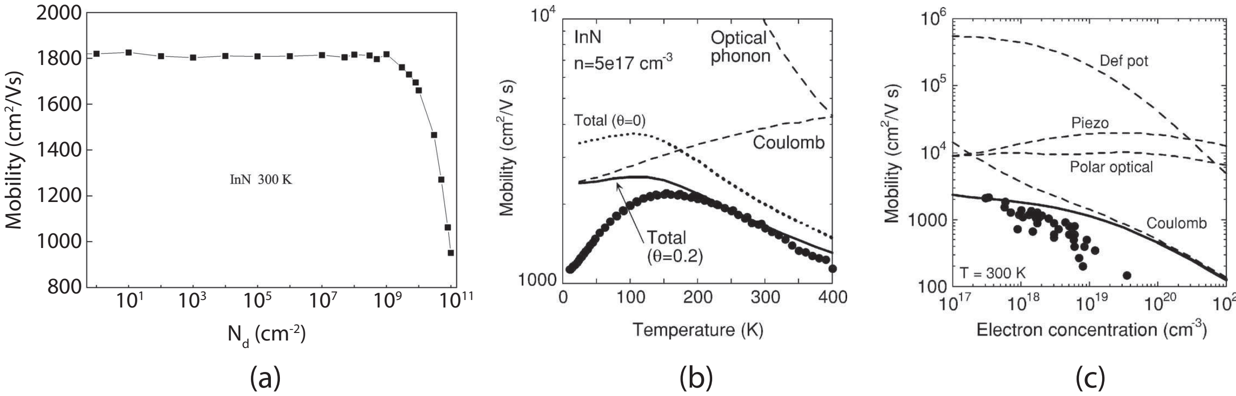


**Figure 4.4** (a) Simulated mobility of InN as a function of dislocation density $N_d$ adapted from Ref. [54]. Measured and calculated mobility (ignoring dislocation scattering) of InN as a function of temperature (b) and electron concentration (c) reproduced from Ref. [123]. Note that in (b) a compensation ratio $\Theta = 0.2$ is invoked to improve the agreement with experiment.

optical effects, as shown in Fig. 4.2.[b] However, current state of the art InN still has threading dislocation densities $\gtrsim 10^9$ cm$^{-2}$, high enough that dislocation scattering can have a strong effect.

In this work, the effect of dislocation scattering in InN will be explored by comparing modeled transport parameters to experimental data. Along the way, any extensions from existing transport theory will be explained, and key insights from the theoretical process will be discussed. The final objective of this analysis is to use the dislocation density as a fitting parameter in self-consistently modeling thermopower and Hall mobility, which can then be compared to independent measurement of the dislocation density obtained through TEM of the same films. Thermopower is included in addition to Hall mobility because it is also sensitive to scattering mechanisms and supplies a second set of data to fit, improving confidence in any model that accurately predicts both sets of transport parameters simultaneously using all of the same assumptions and inputs. Broader impacts for InN and the field will be discussed where insights can be drawn from this analysis.

## 4.2 Experiment

InN thin film samples from both W. Schaff's group at Cornell University as well as J. Speck's group at the University of California - Santa Barbara (UCSB) were used for this work. The Cornell samples were grown by molecular beam epitaxy (MBE) on c-sapphire substrates using AlN nucleation and GaN buffer layers. Detailed descriptions of the growth conditions of these samples can be found in references [112] and [19]. The UCSB samples were grown by plasma assisted MBE (PAMBE) on semi-insulating GaN commercial templates using ~100 nm thick undoped GaN buffer layers according to procedures reported in references [113] and [114]. A large set of samples was studied, though a select set of three samples illustrating the full range of available dislocation densities is discussed here for brevity. Hall and thermopower data on other samples are similar to

[b] At this point the reader may rightly suggest that the same or similar dislocation reduction strategies be applied to InN so that dislocation scattering is no longer dominant in this material either. There has been some work on this issue, for instance using "regrowth" methods as in Refs. [140, 142]. The lack of commercial InN products and the increased difficulties associated with InN growth seem to have limited such efforts, though there is room for much more work in this area.

those presented here, though TEM data was only collected on these three films of interest. The composition and thickness of the films were determined by Rutherford backscattering spectrometry (RBS) measurements performed by Dr. Kin Man Yu of Lawrence Berkeley National Lab. RBS results showed that all of the films are stoichiometric (within an accuracy of ∼3%). Channeling RBS (c-RBS) showed that the films have minimum surface channeling yields $<10\%$, indicating that they are single crystal epitaxial films. A summary of basic structural and electrical data is shown in Table 4.1.

The samples were cut into rectangles of approximately 5 mm × 10 mm in dimension and contacted with small pieces of In foil for thermopower measurements. Thermopower (Seebeck coefficient) measurements were performed by measuring the voltage that develops across a sample when a temperature gradient is applied. The Seebeck coefficient $S$ is given by the ratio $\Delta V/\Delta T$, where the deltas on voltage $V$ and temperature $T$ signify the difference between the values at the two ends of the sample. A detailed description of the thermopower measurement system and procedure has been reported recently [87] and is described more thoroughly in Appendix B. A similar instrument and procedure was used by Brandt *et al.* to measure the thermoelectric properties of Mg doped GaN [143].

Free carrier concentration and mobility were measured as a function of temperature with a Hall effect system using a 3000 Gauss magnet and contacts placed in the van der Pauw configuration. For the variable temperature Hall measurements, the samples were mounted on "chip carriers" consisting of diced pieces of sapphire wafer with Au pads on the corners. The Au pads are created by ebeam evaporation of Au onto a thin adhesion layer of Ti on clean sapphire, which is then shaped by covering the desired areas with pycene wax (Apiezon W) and etching off the metal in the other areas with Bromyl-etch solution (KBr and DI water) for the Au followed by 20:1 Nitric:HF acid solution for the Ti. Very fine (0.002 inch diameter) Cu wires connected the sample to the Au pads, and larger wires connected the Au pads to external equipment, as shown in Fig. 4.5. This setup was used to minimize errors caused by contact size and placement and to minimize thermal transport through the wires for the low temperature measurements. Ohmic contacts for these measurements were made using silver epoxy (Apiezon H20E).

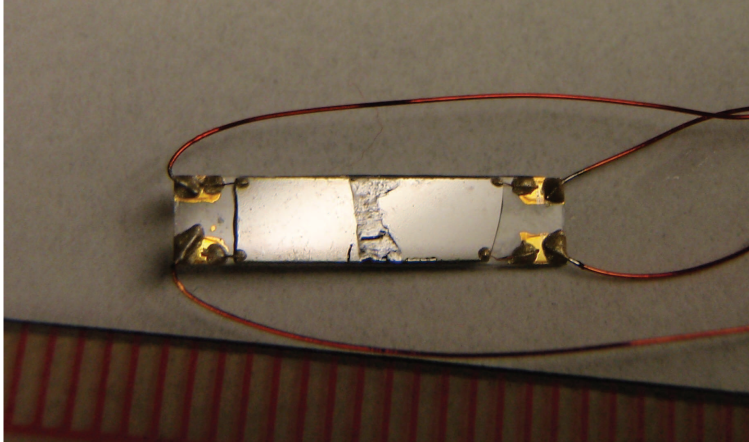

**Figure 4.5** Photograph of InN sample mounted on sapphire chip carrier. The vertical stripe across the center is vacuum grease left by the mounting string from the variable temperature Hall measurements. The scale at bottom is in mm.

Dislocation densities were determined from transmission electron microscopy (TEM) studies

in both plan-view and cross sectional geometry using two-beam conditions and the invisibility criterion. These studies were performed by Dr. Mike Hawkridge at the National Center for Electron Microscopy, Lawrence Berkeley National Lab.

**Table 4.1** Summary of basic sample data measured by RBS, Hall effect, and thermopower at room temperature including the film thickness $d$, the minimum surface channeling yield $\gamma$, electron concentration $n$, mobility $\mu$, and Seebeck coefficient $S$.

| Sample | $d$ (nm) | $\gamma$ | $n$ ($cm^{-3}$) | $\mu$ ($cm^2/Vs$) | $S$ ($\mu$V/K) |
|---|---|---|---|---|---|
| A (GS1360) | 128 | 0.07 | $6 \times 10^{18}$ | 364 | -86 |
| B (100907AC) | 1000 | 0.025 | $9 \times 10^{17}$ | 654 | -194 |
| C (GS2060) | 12160 | 0.07 | $4 \times 10^{17}$ | 1191 | -227 |

## 4.3 Theory

The literature on transport modeling is well developed, and there are various methods for calculating transport coefficients including Monte Carlo, variational, and Rode's iterative technique [54, 123, 144, 145]. The latter, which will be explained here, provides an intuitive procedure that has successfully been used for various group III-V semiconductor materials and requires little computational power. The heart of this procedure is the Boltzmann transport equation, which describes how driving forces such as spatial gradients and fields are balanced by scattering in affecting the distribution function $f$ of carriers. This equation can be written in many different ways, but the following expression captures the essence, shown here for the case of an electric field and a spatial gradient parallel to it:

$$v\frac{\partial f}{\partial z} + \frac{eF}{\hbar}\frac{\partial f}{\partial k} = \left(\frac{\partial f}{\partial t}\right)_{\text{scattering}} \tag{4.1}$$

where $v$ is the carrier velocity, $z$ is a spatial dimension, $F$ is electric field, $\hbar$ is Planck's constant, $k$ is the wave vector, and $t$ is time. Any number of driving forces for transport such as electric and magnetic fields or a gradient in temperature or carrier concentration can be included on the left hand side, while any number of scattering mechanisms can be included on the right hand side. At steady state, the driving forces on the left hand side must be balanced by scattering on the right hand side such that a steady state distribution function $f$ is achieved.[c] For example, an electron experiencing an electric field is accelerated until it is scattered; hypothetically without scattering mechanisms the electron's velocity would increase indefinitely. This equation also shows that in the absence of any driving forces the rate of change of the distribution function goes to zero; then the familiar Fermi-Dirac equilibrium distribution function $f_\circ = 1/\left(e^{(\varepsilon-\varepsilon_F)/k_BT}+1\right)$ is obtained.

The distribution function is of course a function of the carrier's energy $\varepsilon$ (or equivalently momemtum $k$) and the temperature $T$, but as shown in Eq. 4.1, can also be a function of fields and spatial position. This total distribution function $f(\varepsilon, T, F, z)$ can be thought of as the equilibrium

[c]In fact transient processes can also be modeled using the iterative technique with the Boltzmann equation by assuming each iteration corresponds to the appropriate time step, although Monte Carlo techniques are for often used for transient process modeling.

distribution function $f_\circ(\varepsilon, T)$ modified by the processes of fields, spatial gradients, and scattering in the following way:

$$f = f_\circ + g \tag{4.2}$$

where $f$ is the total distribution function, $f_\circ$ is the equilibrium distribution function, and $g(\varepsilon, T, F, z)$ is the small perturbation to the equilibrium distribution due to such processes described by Eq. 4.1. Thus, the effects of any non-equilibrium conditions are contained within $g$. Our task, then, is to evaluate how any non-equilibrium conditions affect the perturbation function $g$. It turns out that $g$ can be calculated straightforwardly from analyzing each scattering mechanism. The following notation will be useful: a carrier initially in the state characterized by $k$, will be scattered into the state characterized by $k'$. For elastic scattering processes such as ionized impurity scattering, in which the energy of the carrier is unaffected by the scattering process, i.e. $k = k'$, $\varepsilon = \varepsilon'$, $f = f'$, the contribution to $g$ can be evaluated analytically and lumped into an elastic relaxation rate $\nu_{\mathrm{el}}$. Such processes can be treated properly within the relaxation time approximation, where the relaxation time $\tau = 1/\nu_{\mathrm{el}}$. For inelastic scattering, such as optical phonon scattering, the energy of the carrier *is* affected by the scattering process and thus cannot be treated properly within the relaxation time approximation. Because the outcome (the final state of the carrier) of the inelastic scattering event depends on what states are available, the scattering process itself depends on the current distribution of carriers; it depends on $g$. Thus $g$ is both an input and an output to such a scattering process, and therefore cannot be calculated analytically. In momentum space, carriers can be scattered both into and out of a state $k$, such that $g$ contains both a scattering-*out* rate $S_{\mathrm{o}}$ and a scattering-*in* rate $S_{\mathrm{i}}$ (not to be confused with the Seebeck coefficient $S$). Then Rode shows that $g$ can be written as follows:

$$g = \frac{S_{\mathrm{i}}(g') - v(\partial f/\partial z) + (eF/\hbar)(\partial f/\partial k)}{S_{\mathrm{o}} + \nu_{\mathrm{el}}}. \tag{4.3}$$

Solutions to Eq. 4.3 can be used to calculate transport coefficients as shown below. Since it cannot be solved analytically however, a numerical approach is taken where the initial condition is assumed to be the equilibrium state $g = 0$ (although this choice is arbitrary) and Eq. 4.4 below is solved iteratively until convergence occurs, usually within less than 5 iterations. For inelastic processes, the $(i+1)$th iteration uses $g_i$, the distribution from the previous iteration, as an approximation until $g_{i+1} = g_i$.

$$g_{i+1} = \frac{S_{\mathrm{i}}(g_i') - v(\partial f/\partial z + (eF/\hbar)(\partial f/\partial k))}{S_{\mathrm{o}} + \nu_{\mathrm{el}}} \tag{4.4}$$

Note that the i subscript on the scattering-in rate $S_{\mathrm{i}}$ does not refer to the $i$th iteration. Once $g$ has been determined by successive iteration of Eq. 4.4, the drift mobility can be calculated by numerical integration of the following equation:

$$\mu = \frac{\hbar}{3m_\circ} \frac{\int k^3 (g/Fd) dk}{\int k^2 f dk} \tag{4.5}$$

where $d$ has to do with the energy dependent effective mass where $1/d = (m_\circ/\hbar^2 k)\partial\varepsilon/\partial k$. In the limit $k = 0$, $d = m^*/m_\circ$ is simply the effective mass ratio.

The thermopower can also now be calculated, though there is a bit of logic in this process worth discussing. The current density $J$ in the presence of electric field $F$ and temperature gradient $\nabla T$

is given by

$$J = \sigma[F - (\nabla\varepsilon_F/e) - S\nabla T] \tag{4.6}$$

where $\sigma$ is the electrical conductivity, $\varepsilon_F$ is the Fermi energy, and $S$ is the thermoelectric power or Seebeck coefficient. In open circuit, $J = 0$ and the crystal comes to equilibrium so that $\nabla\varepsilon_F = 0$ and

$$S = F/(\partial T/\partial z) \tag{4.7}$$

for a temperature gradient parallel to the z-axis. This equation is the definition of the thermopower: voltage that develops in the presence of a temperature gradient. And this is how thermopower is evaluated experimentally, in open circuit conditions. But somewhat non-intuitively, in order to evaluate $S$ theoretically the short circuit condition is applied and $S$ can be written as follows:

$$S = -\left(\frac{\partial\varepsilon_F}{\partial z}/e + \frac{J}{\sigma}\right)/\frac{\partial T}{\partial z}. \tag{4.8}$$

Then the spatial gradient in the Fermi energy is related to the temperature gradient through Poisson's equation and the Seebeck coefficient can be written

$$S = \frac{k_B}{e}\left[\frac{\int k^2 f(1-f)(\varepsilon/k_BT)dk}{\int k^2 f(1-f)dk} - \frac{\varepsilon_F}{k_BT}\right] - \frac{(J/\sigma)}{(\partial T/\partial z)}. \tag{4.9}$$

Numerical integration of Eq. 4.9 yields the Seebeck coefficient. This equation depends of course on the distribution function $f$, which in turn contains the perturbation part $g$, which contains the effects of scattering. Thus the effects of scattering are contained within this description of the Seebeck coefficient. It's also worth noting that Eq. 4.9 contains $\sigma = n\mu e$, which shows that the mobility must first be calculated using Eq. 4.5 before evaluation of the Seebeck coefficient.

Now one thing that has been ignored so far is the form of the elastic relaxation rates and inelastic scattering rates $\nu_{\text{el}}$, $S_{\text{o}}$, $S_{\text{i}}$. Included in these are the effects of elastic scattering mechanisms acoustic phonon (ac), piezoelectric (pe), ionized impurity (ii), and dislocation scattering (disl), and the inelastic optical phonon scattering (LO), the latter three of which are the most important in InN. The incorporation and dependence on material parameters (Table 4.2) of all of these scattering mechanisms is discussed by Rode [145] and remain unchanged in our analysis, except for dislocation scattering, which deserves further discussion. Although dislocation scattering is not included in Rode's treatment, it is easily incorporated there by calculating a relaxation rate for this mechanism and adding it to those of the other elastic scatting mechanisms, $\nu_{\text{el}} = \nu_{\text{ac}} + \nu_{\text{pe}} + \nu_{\text{ii}} + \nu_{\text{dis}}$. The methodology for calculating a relaxation rate for dislocation scattering has been developed by Look and Sizelove [136]. This method mirrors very closely the method used to treat ionized impurity scattering, differing only in the shape of the potential since the charge is arranged along a line rather than just at points. The charge is assumed to be distributed continuously along the line at a rate of 1 charge per c lattice constant distance; the line density of charge is then 1 $e$/0.570 nm along the lines of dislocation.[d] The potential surrounding a continuous line of charge, including mobile charge screening effects, had been developed previously by Bonch-Bruevich and Glasko in 1966, although here we use Rode's method of accounting for screening since it is valid for both

[d] As shown by Look, the dislocation density extracted from this analysis doesn't depend strongly on this assumption. Wang et al. assumed 1 charge per monolayer along TDs [52, 55]. Measurements of GaN have produced estimates in the range of 0.3-1 $e$ per $c$ lattice constant, depending on the type of dislocation and type (n- or p-) of GaN [137, 139, 146].

degenerate and nondegenerate cases [147]. The relaxation rate is then written as follows:

$$\nu_{\text{dis}}(k) = \frac{N_{\text{dis}} m^* e^4}{\hbar^3 \varepsilon_S^2 c^2} \left[\beta^4 \left(1 + \frac{4k^2}{\beta^2}\right)^{3/2}\right]^{-1} \tag{4.10}$$

where $\varepsilon_S$ is the static dielectric constant, $c$ is the lattice constant, and $\beta$ is the inverse screening length defined below. In our analysis, the effective mass term $m^*$ in Eq. 4.10 is replaced by $m_\circ d(k,T)$ to account for the energy dependent effective mass of InN. The screening length describes the rearrangement of mobile charge such as electrons around stationary charge such as charged dislocation lines following the Poisson equation; it provides a characteristic length beyond which the effects of the stationary charge are not "felt." The treatment of the screening length is very important in transport calculations as it guarantees a finite interaction volume, thereby preventing certain integrals in the scattering rate calculation from going to infinity and guaranteeing conversion to a finite value. This has been treated in various ways, most famously by Conwell and Weisskopf [148], Brooks and Herring [149, 150], and Dingle [151], but here we use a variation of Dingle's theory developed and implemented by Rode [145]. The inverse screening length $\beta$ is given by:

$$\beta^2 = (e^2/\varepsilon_S k_{\text{B}} T) \int (k/\pi)^2 f(1-f) dk. \tag{4.11}$$

In the degenerate and non-degenerate limits the above equation reduces to the more familiar inverse Debye length and inverse Thomas-Fermi screening length, respectively. It should also be noted that because the dislocations are donors, the electron concentration is given by the charge neutrality equation: $n + N_A = N_D + N_{\text{dis}}/c$, where $c$ is the lattice constant in the c-direction along the dislocation line, and $N_D$ and $N_A$ are the donor and acceptor concentrations. In the analysis below the donors are considered to be singly charged and compensation is minimized. Finally, there are a number of parameters used in the calculation of transport coefficients, which are listed in Table 4.2.

**Table 4.2** Summary of physical parameters and constants used in the transport calculations - taken from Ref. [123] unless noted otherwise.

| Parameter | Value |
|---|---|
| Bandgap (eV) | 0.7 |
| Band edge electron effective mass, $m_e^*/m_\circ$ | 0.065 |
| Band edge hole effective mass, $m_h^*/m_\circ$ | 0.64 |
| LO phonon energy (meV) | 73 |
| Static dielectric constant, $\varepsilon_S/\varepsilon_\circ$ | 10.3[a] |
| High frequency dielectric constant, $\varepsilon_\infty/\varepsilon_\circ$ | 6.7 |
| Volume deformation potential (eV) | 3.6 |
| Acoustic phonon velocity, longitudinal (cm/s) | $5.2 \times 10^5$ |
| Acoustic phonon velocity, transverse (cm/s) | $1.2 \times 10^5$ |
| Piezoelectric constant, $e_{14}$ (C/m$^2$) | 0.375 |
| $c$ lattice constant (nm) | 0.57038[b] |

[a] From Ref. [63]
[b] From Ref. [152]

Before comparisons are made to experiments, some simple exercises of the model will illustrate the effects of dislocation scattering on the overall transport landscape for InN. The calculated

mobility of InN at room temperature as a function of dislocation density $N_{\text{dis}}$ is shown in Fig. 4.6a for several values of the electron concentration $n$. Note the similarity between this plot and the Monte Carlo calculations of Yu and Liang shown in Fig. 4.4a [54]. A dislocation density threshold exists, below which the mobility is invariant to changes in $N_{\text{dis}}$ and above which the mobility sharply declines with increasing $N_{\text{dis}}$. The critical threshold depends on the electron concentration varying from $\sim 10^8$-$10^{10}$ cm$^{-2}$ for the range of $n$ considered here, taking on a larger value for higher electron concentrations. This is because a greater density of mobile charges serves to better screen the charged dislocations, thereby minimizing their deleterious effects until there are more of them. This figure also shows that the typical range of $N_{\text{dis}}$ reported in the literature is high enough to affect the mobility, especially for films with $n < 10^{18}$ cm$^{-3}$. Thus one can predict that if dislocation density can be reduced to below $10^7$ cm$^{-2}$, as accomplished with GaN, then the effect on transport can be made insignificant for InN with $n \geq 10^{17}$ cm$^{-3}$, the lowest electron concentration achieved to date.

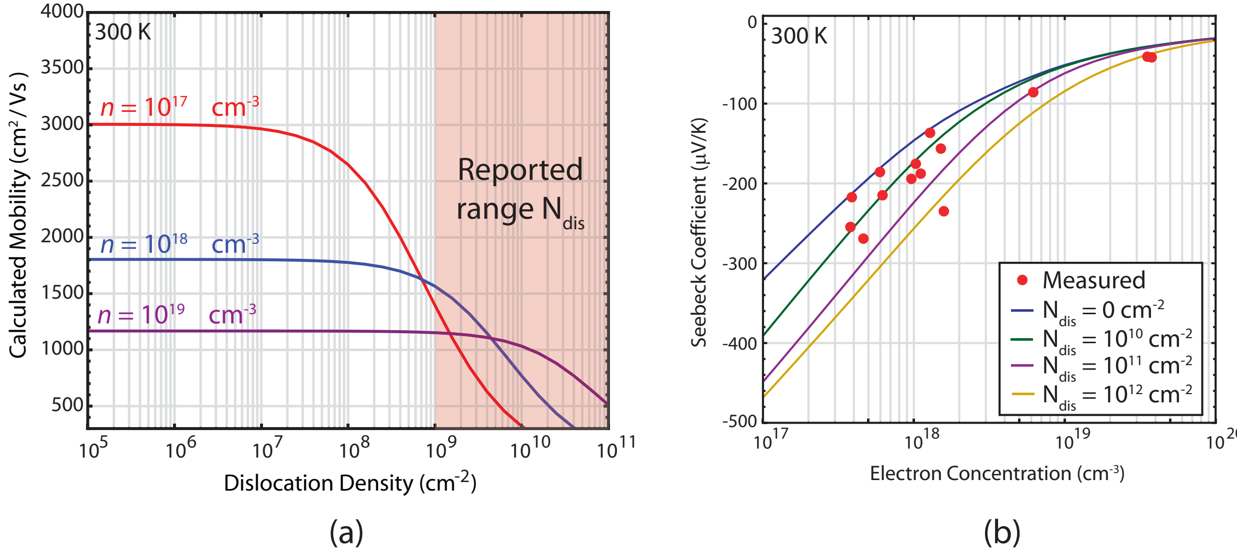


**Figure 4.6** (a) Calculated dependence of mobility on dislocation density for three different values of electron concentration, which is labeled for each curve. In each, the ionized impurity concentration is set equal to the electron concentration. The shaded region indicates the range of typical dislocation densities reported in the literature for InN. (b) Calculated Seebeck coefficient at room temperature as a function of electron concentration for several different values of $N_{\text{dis}}$. Measured values (red dots) are shown for comparison.

Calculations illustrating the effect of dislocation scattering on the Seebeck coefficient of InN are shown in Fig. 4.6b. The result, again accentuated at low electron concentrations due to screening effects, is that dislocation scattering increases the magnitude of the Seebeck coefficient, $|S|$. The measured Seebeck coefficient for a number of InN samples over a large range of electron concentrations are also plotted for comparison. Nearly all of the data points can be explained using $N_{\text{dis}} \leq 10^{11}$ cm$^{-2}$. The considerable scatter in the data may be explained then by variation of the dislocation density across this set of samples, although this has not yet been experimentally investigated.

Figs. 4.7a and b illustrate the individual contributions of the various scattering mechanisms to the total composite mobility as a function of electron concentration and temperature, respectively.

At room temperature, the acoustic and piezoelectric scattering modes are not playing a role, and the mobility is determined by dislocation, ionized impurity, and optical phonon scattering. The total mobility is plotted twice in each figure, once including (solid) and once ignoring (dashed) dislocation scattering to demonstrate the difference that it makes. In Fig. 4.7a, the effect is observed only for lower electron concentrations. Increasing $N_{\mathrm{dis}}$ shifts the *disl* curve down, pushing the dominance of this mechanism to higher electron concentrations. Fig. 4.7b shows that as the temperature decreases, optical phonon scattering quickly dissipates and the mobility is determined by the two Coulomb modes. Although dislocation and ionized impurity scattering have similar temperature dependences, dislocation scattering actually has a somewhat steeper slope owing to its higher scattering rate for very low energy carriers. This, combined with the very high density of TDs, produces the decreasing mobility at low temperature that could not be explained with ionized impurity scattering, as shown in Fig. 4.4b and discussed in more detail below.

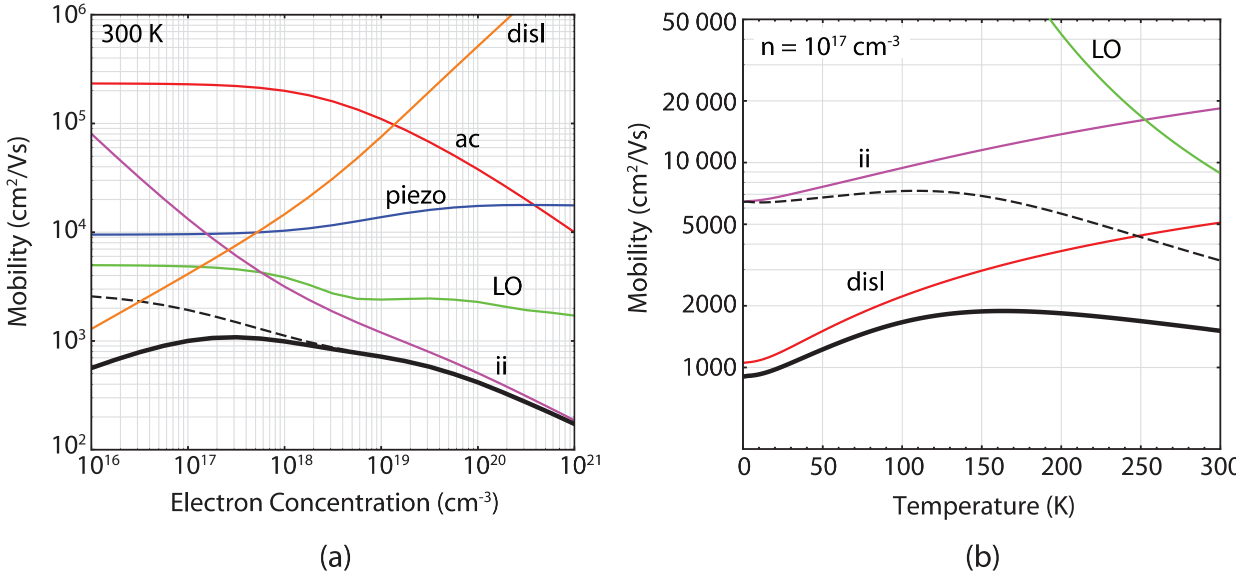


**Figure 4.7** Calculated mobility of InN (a) as a function of electron concentration and (b) as a function of temperature, both showing the individual contributions of dislocation scattering (disl) for $N_{\mathrm{dis}} = 10^9$ cm$^{-2}$, acoustic phonon scattering (ac), piezoelectric scattering (piezo), optical phonon scattering (LO), and ionized impurity scattering (ii). (a) is calculated at room temperature and (b) is for $n = 10^{17}$ cm$^{-3}$. In both plots the solid black line is the total composite mobility, and the black dashed line is the composite mobility without dislocation scattering.

## 4.4 Results and discussion

The measured Seebeck coefficients over a temperature range of ∼200 to 300 K are shown in Fig. 4.8a. The room temperature values are also shown in Table 4.1. As expected for n-type material the Seebeck coefficients are negative. The linear, monotonic increase towards zero with decreasing temperature is as expected for degenerately doped material and the magnitude varies strongly with electron concentration. Note that the thickness of these three samples differs by a factor of ∼100 and Hall electron concentration more than a factor of 10, as shown in Table 4.1. Such extremes in sample properties are chosen on purpose to illustrate the role of extended defects on transport

properties in InN. It is well known that electron concentration in InN tends to decrease with increasing sample thickness, though the cause for this and indeed the root cause of the background electron concentration in general is still a matter of debate. It has also been shown that the density of threading dislocations in InN films decreases strongly with increasing thickness since the substrate/film interface is a major source of strain in growing films. As discussed above, this correlation is viewed by some as evidence of the donor nature of dislocations.

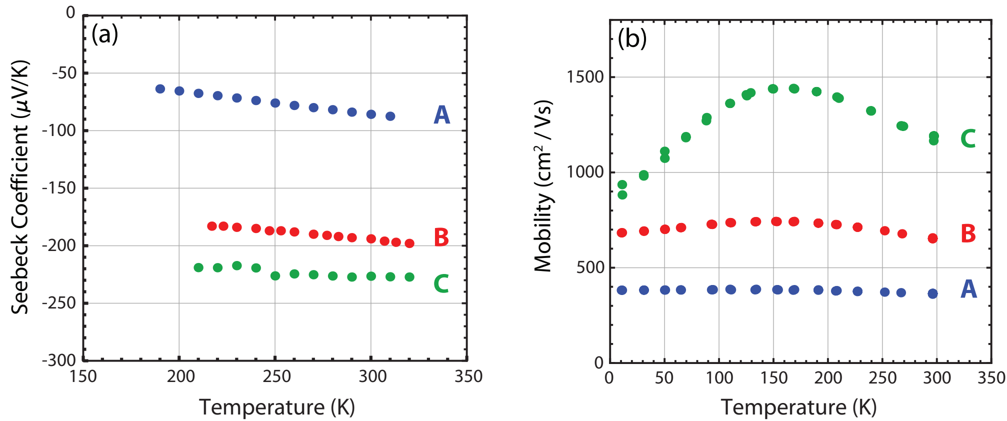


**Figure 4.8** Measured Seebeck coefficient (a) and mobility (b) of selected samples A, B, and C as a function of temperature as measured by thermopower and Hall effect.

The measured mobility from room temperature down to $\sim 4$ K is shown for the selected samples in Fig. 4.8b. The room temperature values are also shown in Table 4.1. Here we see that electron mobility is nearly temperature invariant for the higher carrier concentration samples A and B and only for sample C, with carrier concentration approaching $10^{17}$ cm$^{-3}$, does the mobility change significantly with temperature. This is typical behavior for InN, though it is not well understood. Fig. 4.9 shows the minimal variation of mobility with temperature for several InN samples of different thickness and electron concentration measured by *Lebedev et al.* [51]. This figure also illustrates for one sample how much the measured mobility deviates from the expected temperature dependence, $\mu \sim T^{3/2}$ at low temperature and $\mu \sim T^{-3/2}$ at high temperature, produced by ionized impurity and optical phonon scattering, respectively. This point is reiterated in Fig. 4.10a, which shows the component contributions of optical phonon and singly-ionized impurity scattering to the total mobility for a sample with relatively low carrier concentration. Varying the carrier concentration matching the measured $n$ of the three selected samples, as shown in Fig. 4.10b, shows that not only are the calculated mobilities too large by approximately a factor of four, but for all but the lowest concentration sample (C), the model fails completely to qualitatively reproduce the observed temperature invariance. It's as if there is another scattering mechanism so far unaccounted for reducing the mobility at nearly all temperatures. As shown below, this role can be filled at least partially by dislocation scattering.

As described in detail in section 4.3, Rode's iterative Boltzmann equation solution method can be used including a dislocation scattering component (following the method of Look and Sizelove) to calculate both the thermopower and mobility of n-type InN [136, 145]. The solid lines in Figs. 4.11a and 4.11b are the results of such calculations, using the dislocation density as primary fitting parameter. The dislocation density and to a minor degree the electron concentration are varied in order to achieve excellent agreement between the calculated and measured values of

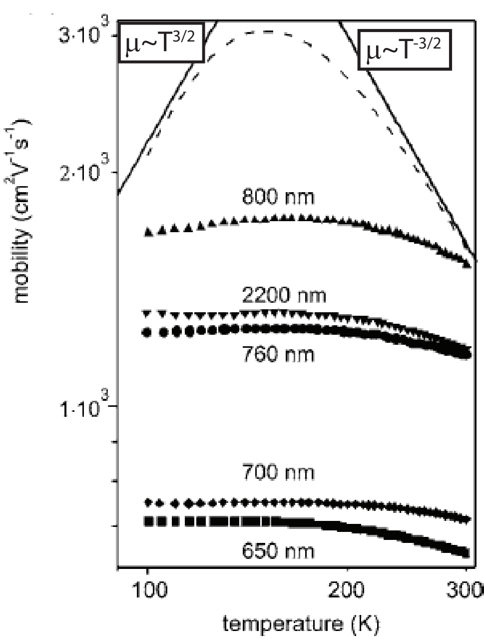


**Figure 4.9** Variation of mobility with temperature for several InN samples of different thickness and electron concentration (points) ranging from $\sim 2 \times 10^{17}$ cm$^{-3}$ to $\sim 6 \times 10^{18}$ cm$^{-3}$, reproduced from Ref. [51]. The dashed line shows the result of calculations for the expected variation of mobility for the 800 nm sample ignoring dislocation scattering; the solid lines indicate the typical dependence of mobility on temperature, $\mu \sim T^{3/2}$ at low temperature and $\mu \sim T^{-3/2}$ at high temperature due to ionized impurity and optical phonon scattering, respectively. Note the nearly temperature invariant mobilities and both quantitative and qualitative disagreement between calculated and measured values.

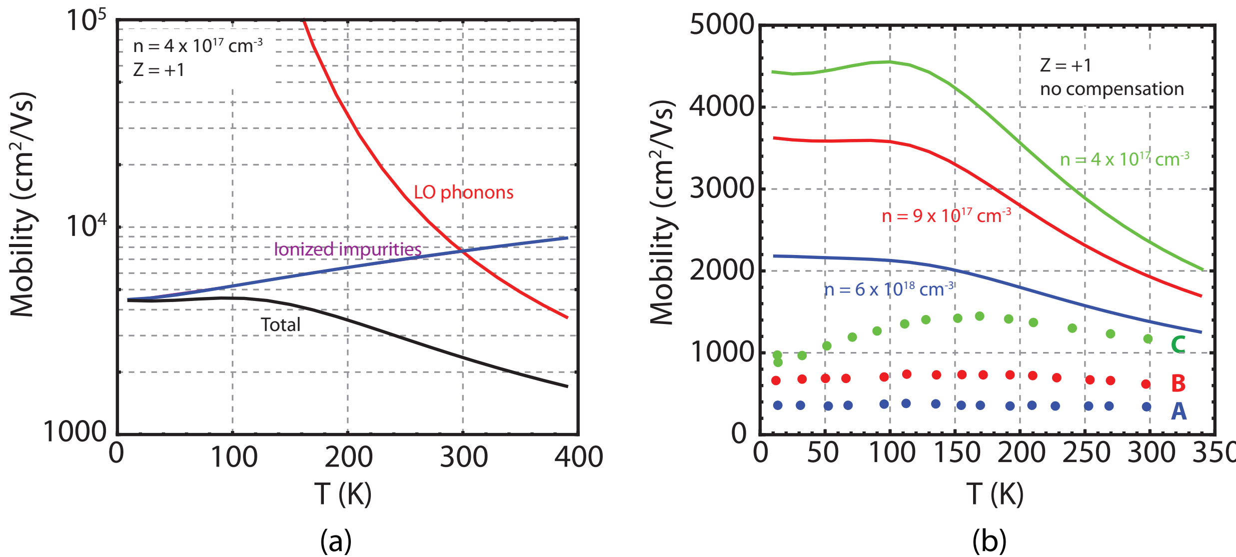


**Figure 4.10** (a) Calculated InN electron mobility for a sample with electron concentration $n = 4 \times 10^{17}$ cm$^{-3}$ showing the temperature dependence resulting from contributions of optical phonon and singly-ionized impurity scattering. Ignoring dislocation scattering, these are the two most dominant scattering mechanisms. (b) Measured (points) and calculated (lines) mobility using the measured electron concentration of the three selected samples. Note that not only are the calculated mobilities too large by approximately a factor of four, but for all but the lowest concentration sample (C) the model fails completely to qualitatively reproduce the observed temperature invariance. Adapted from figures courtesy of J. Ager.

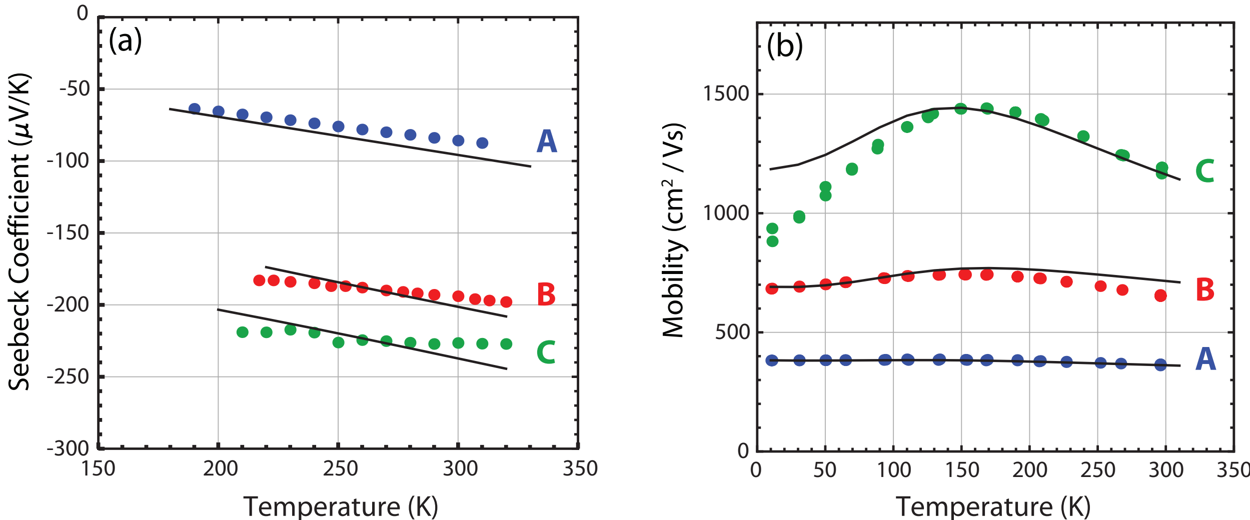


**Figure 4.11** Measured (points) and modeled (solid lines) Seebeck coefficient (a) and mobility (b) of selected samples as a function of temperature. For each sample the modeled curves in (a) and (b) are calculated using the same value of the dislocation density, which is the primary fitting parameter.

Seebeck coefficient and mobility as a function of temperature; the best-fit dislocation densities are listed in Table 4.3 along with those measured independently by TEM, showing good agreement for all three samples with dislocation densities that differ by as much as two orders of magnitude. The quality of self-consistent modeling of both the Seebeck coefficient and mobility and the ability to predict rather precisely the dislocation line density gives confidence in this approach and leads to the positive conclusion that dislocation scattering is indeed an important and sometimes dominant scattering mechanism in n-type InN.

**Table 4.3** Comparison of fitting parameters dislocation density $N_{dis}$ and carrier concentration $n$ to those measured by TEM and Hall effect, respectively.

| | $n_{RT}$ (cm$^{-3}$) | | $N_{dis}$ (cm$^{-2}$) | |
|---|---|---|---|---|
| Sample | Measured | Model | Measured | Model |
| A (GS1360) | $6 \times 10^{18}$ | $6.7 \times 10^{18}$ | $\sim 1 \times 10^{11}$ | $1.5 \times 10^{11}$ |
| B (100907AC) | $9 \times 10^{17}$ | $9.9 \times 10^{17}$ | $\sim 2 \times 10^{10}$ | $1.3 \times 10^{10}$ |
| C (GS2060) | $4 \times 10^{17}$ | $4.8 \times 10^{17}$ | $\sim 1 \times 10^{9}$ | $3.3 \times 10^{9}$ |

As mentioned above, dislocation density can vary through the thickness of InN films. The effect of this inhomogeneity on the current analysis should be considered. The dislocation densities reported in Table 4.3 are obtained from plan-view TEM samples, meaning that this is the dislocation density at or near the surface of the films. Dislocation densities measured in this way are generally more accurate than from cross sectional samples because it allows for a two dimensional view from which the areal density can directly be counted as shown in Fig. 4.12; in cross sectional samples a line density is measured from the side view from which an areal density can be inferred. Ultimately, measurements of dislocation density from both methods should be considered approximate. The cross sectional view allows for the determination of any thickness variation in dislocation density, which is not visible in the plan view. Thus, these measurements are complimentary. Cross sectional TEM images of sample B are shown in Fig. 4.13 for an example.

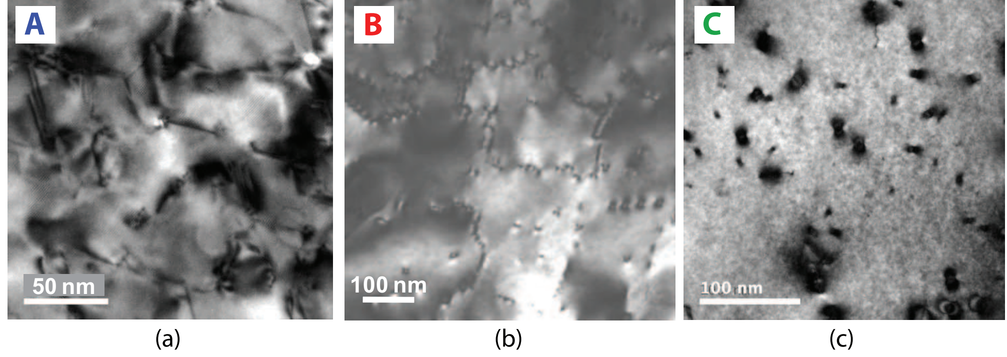


**Figure 4.12** Plan-view TEM images of samples (a) A, (b) B, and (c) C, respectively. Most of the contrast in these images comes from dislocations and other defects. Sample B is particularly interesting; here the dislocations form in lines stitching out a patchwork of areas that are largely dislocation free. This implies that the growth began as three dimensional islands, which later coalesced requiring dislocations to accommodate the low angle grain boundaries. This growth mechanism is typical of group III-nitrides and is termed columnar growth.

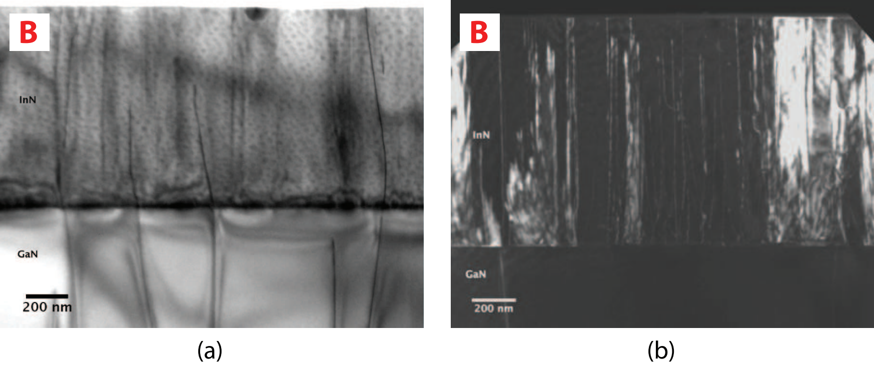


**Figure 4.13** Cross sectional TEM images of sample B in bright field (a) and dark field (b) modes. The threading dislocations are evident in approximately the same density throughout the thickness of the film except within about the first 100 nm of film where a great deal of contrast from defects is observed. The field of grey spots in (a) overlaying the InN part of the sample are actually In droplets, an artifact of sample preparation due to the preferential sputtering of N during ion milling of InN.

Table 4.4 lists the dislocation densities at the film surfaces obtained from plan-view samples as well as dislocation densities estimated near the interface from cross sectional samples. An interface density separate from the surface can't be determined for the thinnest sample so none is listed. For sample B, there is little difference between the interface and surface density, indicating that dislocation density is relatively constant through the 1 micron thickness. For sample C, which is much thicker at ∼12 microns, the dislocation density decreases by a factor of ∼30 from the interface to the surface. However, this decrease is assumed to occur non-linearly, dropping rapidly in within the first few hundred nanometers then leveling off, as reported in the literature [51]. Thus, the majority of electrons moving through the film encounter material with dislocation density closer to that measured at the surface. The Hall effect is also weighted by the square of the mobility of the carrier, which further weights this measurement towards low dislocation density parts of the film since dislocations act as strong scattering centers. These conditions are reflected in the fact that the modeled dislocation density matches the surface density much more closely than the interface density.

**Table 4.4** Comparison of fitting parameter dislocation density $N_{\text{Model}}$ to those measured near the surface with plan view samples $N_{\text{Surface}}$ and near the interface with cross sectional samples $N_{\text{Interface}}$.

| Sample | Thickness (nm) | $N_{\text{Model}}$ (cm$^{-2}$) | $N_{\text{Surface}}$ (cm$^{-2}$) | $N_{\text{Interface}}$ (cm$^{-2}$) |
|---|---|---|---|---|
| A (GS1360) | 128 | $1.5 \times 10^{11}$ | $\sim 1 \times 10^{11}$ | – |
| B (100907AC) | 1000 | $1.3 \times 10^{10}$ | $\sim 2 \times 10^{10}$ | $\sim 5 \times 10^{10}$ |
| C (GS2060) | 12160 | $3.3 \times 10^{9}$ | $\sim 1 \times 10^{9}$ | $\sim 9 \times 10^{10}$ |

The calculated mobility of sample C at low temperature diverges to some degree from the measured mobility; it is unclear at this time if this is simply the result of a breakdown of the model's assumptions such as the Born approximation, which holds best at high temperatures, or if a true physical origin such as sample non-uniformity or some other undetermined scattering mechanism plays a role. It should be noted that the measured mobility is averaged over all carriers

in the sample; thus decreasing mobility could also be due to greater contribution from low mobility carriers such as those at the surface or at other defective areas such as grain boundaries, inversion domains, or stacking faults. However, little physical information is yet available to motivate the use of such a model. In this analysis point defects were assumed to be singly charged and compensation was assumed to be minimal, though both factors would change the dislocation density estimated in this process. It should be noted that, for sample C especially, the dislocation density changes greatly throughout the thickness of the film, while the model assumes a uniform and homogeneous density. A more detailed model could account for this inhomogeneity.

## 4.5 Conclusions

The success of the transport model presented in this chapter at accurately reproducing the Seebeck coefficient and mobility, while predicting precisely the threading dislocation density of the films provides strong evidence that dislocations are in fact donors and lines of positive charge, which contribute significantly to the observed mobility of n-type InN. This conclusion provides several recommendations for the field. Although compelling, the experiment in this chapter provides only correlation and indirect evidence of charged dislocations; surface probe and electron microscopy techniques capable of directly observing charge on dislocations should be applied to InN. Such experiments would also provide insight into the donor nature of dislocations, i.e., whether dislocations are intrinsically donor-type or does this feature result from the decoration of dislocations by point defects. The reduction of dislocation density through growth studies should be actively pursued, likely leading to both reductions in the electron concentration and improved mobility. Threading dislocations may also act to short pn junctions, which would obviously have deleterious effects on any devices, but also provides a mechanism to explain why p-type material buried under an n-type surface layer is not junction isolated and contributes to electrical and thermoelectric measurements as if connected in parallel, as discussed in Chapter 3. Besides simply acting as nonradiative recombination centers affecting the optical properties of n-type InN, if the Fermi level is indeed pinned well above the conduction band edge at dislocations, then the bands will be bent severely in the vicinity of dislocations in p-type InN. These built-in fields could act to separate photocarriers, thereby explaining or contributing to the mysterious quenching of PL in p-type InN, also discussed in Chapter 2.

# Chapter 5

# Electrolyte-gated transport

## 5.1 Background and theory

In n-type InN, Fermi level pinning at the surface creates an accumulation of electrons within the first $\sim$ 10 nm below the surface. Electron concentrations on the order of $10^{20}$ cm$^{-3}$ exist within this layer. Similarly on p-type material, this Fermi level pinning creates an n-type inversion layer on the surface. Capacitance-voltage measurements are a common way of investigating doping in semiconductor devices within the depletion region of a p-n junction or Schottky contact [153]. However, due to the highly degenerate surface of InN films, all metals form Ohmic contacts. Instead, an electrolyte can be used to form a blocking contact over a range of a few volts. Electrolyte based capacitance-voltage (ECV) measurements have been used successfully to study inhomogeneities in carrier concentration in the near surface region and even to observe the presence of ionized, negatively charged acceptors in Mg-doped InN [70, 85–88].

This technique requires that changing the bias on the electrolyte contact changes the pinning position of the Fermi level at the surface relative to the conduction and valence band edges ($E_{\mathrm{CBE}}$ and $E_{\mathrm{VBE}}$) and results in a redistribution of free carriers in the film. Simulations employing solutions to the Poisson equation are shown in Fig. 5.1, which illustrate the band bending and variation of free electron and hole concentrations ($n$ and $p$) near the surface at equilibrium, $V_{\mathrm{Bias}} = 0$ V, and for an applied bias of +1.0 V for n-type and p-type InN. The net donor concentration ($N_D - N_A$) assumed for each case is as indicated. For the n-type sample at $V_{\mathrm{Bias}} = 0$ V, the bands are bent downward by nearly 1 V, and the electron concentration increases by two orders of magnitude near the surface. At $V_{\mathrm{Bias}} = 1$ V, the bands are nearly flat and an electron depletion layer actually exists near the surface. For the p-type sample at $V_{\mathrm{Bias}} = 0$ V, the bands are bent downward by $\sim$ 1.5 V and a depletion layer exists between an n-type surface inversion layer and the p-type bulk. At $V_{\mathrm{Bias}} = 1$ V, the band bending is reduced to $\sim$ 0.5 V, and the surface inversion layer is completely depleted, leaving only a depletion layer of holes at the surface. These simulations suggest that any properties of the films that are sensitive to the surface band bending or the surface accumulation/inversion layer would be greatly affected by application of a gate bias through an electrolyte.

ECV measurements have already shown this to be true. Additionally, it has been shown that ion-selective field-effect transistors (ISFETs) can be made from thin films of InN, taking advantage of the fact that exposure to solutions of different concentration or pH will alter the surface Fermi level pinning and therefore the conductance of the films, possibly leading to chemical and biological sensors based on InN [154, 155]. This property was also exploited by Brown *et al.* in an

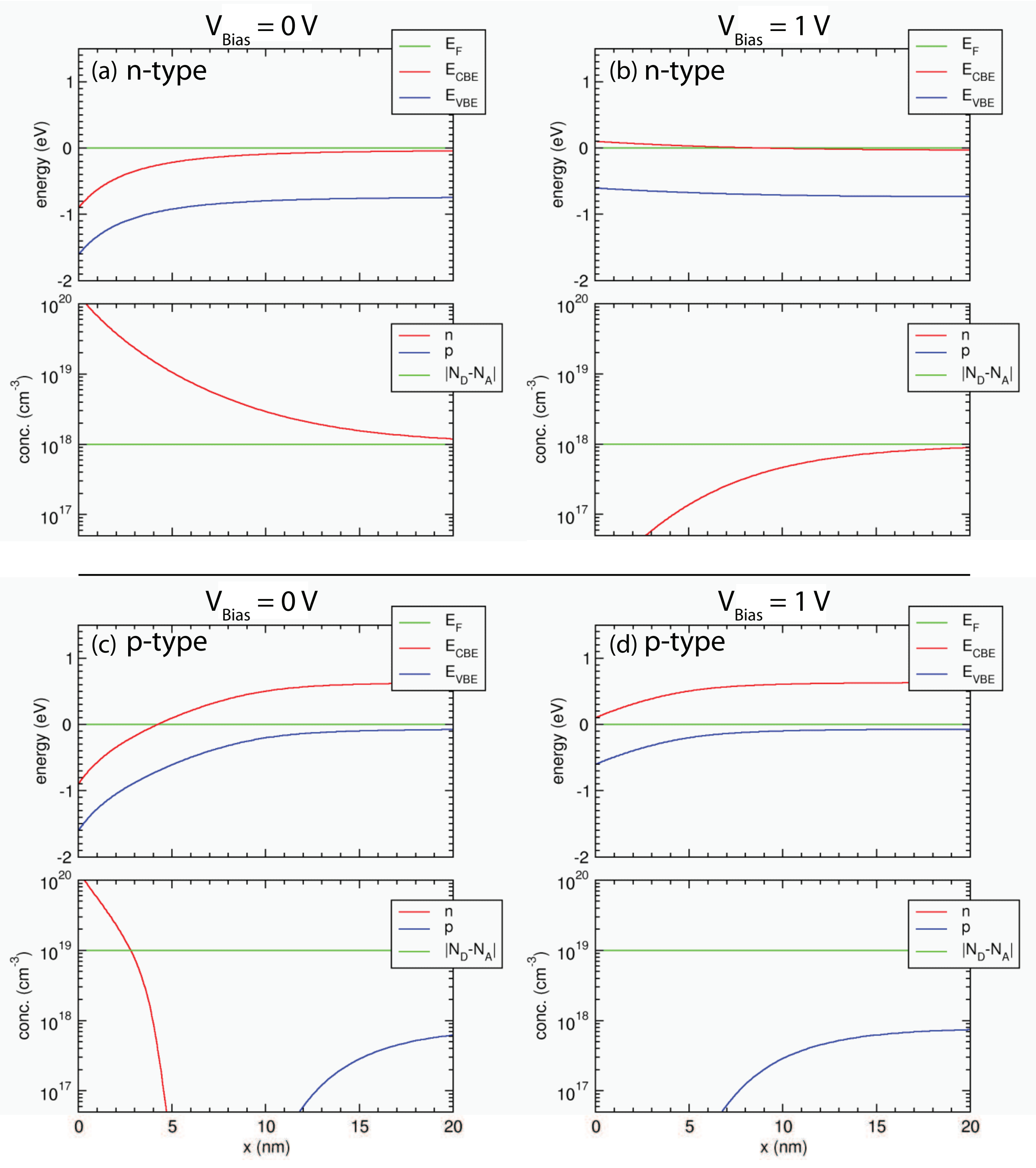


**Figure 5.1** Simulations of the band bending and carrier concentration profiles in the near surface region of n-type ((a) and (b)) and p-type ((c) and (d)) InN for different values of applied bias. At equilibrium, $V_{\mathrm{Bias}} = 0$ V, severe downward band bending and electron accumulation (inversion) is observed in n-type (p-type) material. With $V_{\mathrm{Bias}} = 1$ V this bending is largely undone, and surface electrons are depleted. Simulations by J. Ager using nextnano[3] (http://www.nextnano.de/nextnano3/).

attempt to deplete the surface inversion layer of p-type InN and measure a positive Hall coefficient [89]. Although these electrolyte-gated Hall effect measurements demonstrated strong evidence of modulation of the surface electron inversion layer, p-type Hall coefficients were still not observed likely due to the presence of a similar n-type inversion layer at the interface between the film and substrate/buffer layers. These examples show that the sensitivity of the surface accumulation/inversion layer to electrolyte gating provides more than a way to do ECV measurements; it can be used to control the properties of this layer for the formation of devices or detection by other characterization techniques. In this chapter, preliminary results are presented on two new applications for electrolyte gating of InN. In the first, modulation of the surface conductivity is observed through electrolyte-gated thermopower (ETP) measurements, potentially yielding a direct measure of the thermoelectric contribution of the surface layer to the total measured value. In the second, modulation of the surface conductivity is used to control parasitic surface currents in an effort to observe rectification for the the first time in InN.

## 5.2 Electrolyte-gated thermopower measurements

As discussed in depth in Chapter 3, InN films (especially p-InN) are inhomogeneous and contain various parallel conducting layers. A method for attempting to extract the properties of individual layers of interest was discussed, but required a number of samples with varying layer thickness and treatment with a parallel conduction model. This analysis is not very sensitive to the properties of the surface inversion layer on p-InN films. It would be very interesting to be able to directly measure the contribution from this surface layer in a single film, which is the subject of this section.

The strategy is based on previous work with (ECV) measurements and electrolyte-gated Hall measurements discussed above, showing that the surface accumulation (inversion) layer on n-type (p-type) InN can be modulated by application of a bias through an electrolyte contact. Within the parallel conduction model for thermopower measurements used successfully in previous chapters, this surface layer contributes in parallel with other layers. For p-type films, this surface layer has a negative value and decreases the measured Seebeck coefficient. Writing out Eq. 2.4 for the case of three types of layers is as follows:

$$S_{Observed} = S_{surf}\frac{\sigma_{surf}d_{surf}}{\sigma_T d_T} + S_{bulk}\frac{\sigma_{bulk}d_{bulk}}{\sigma_T d_T} + S_{int}\frac{\sigma_{int}d_{int}}{\sigma_T d_T} \tag{5.1}$$

where contributions from n-type *surf*ace, p-type *bulk*, and n-type *int*erface layers are included. If the surface inversion layer can be depleted completely by electrolyte gating, then the first term on the right hand side of Eq. 5.1 can be eliminated completely from the equation, thereby providing a direct measurement of its value. This is the motivation for performing thermopower measurements of samples in aqueous solutions, using the electrolyte to gate the surface layer: so called electrolyte-gated thermopower (ETP) measurements.

To perform such measurements, two methods immediately come to mind. One way would be to use the available thermopower measurement equipment and devise a way to bring electrolyte in contact with part of the sample surface without immersing the entire sample. This could be accomplished by using o-rings or by building a watertight box on top of each sample. However, the entire sample surface could never be reliably contacted and any leakage of electrolyte would cause shorts between the surface contacts. And construction of an electrolyte containment structure on top of every sample could be tedious. Another method, which will be used here, is to build a

new thermopower stage that can be completely immersed in electrolyte without shorting out the contacts. Such a setup is shown in Fig. 5.2. Pycene wax is used to insulate the thermocouple leads where they are attached to the samples by the usual method of pressed In metal. The stage itself is conceptually similar to those used before, where the sample is bridged between two blocks of different temperatures. In this case, only one block is heated while the other (made of sapphire plates) provides a heat sink. The heater is a 1 W, 200 Ω, thick film chip resistor, available commercially from electronics distributors such as Newark. The heat sink is necessary to set up the temperature gradient; without the heat sink the entire sample heats up nearly uniformly as the sample substrates are very conductive. Spring clips made of teflon and nylon screws secure the sample to the blocks. All of these components are affixed to a plate of plastic; in fact no metal is used in the stage at all to ensure that no unwanted electrochemical reactions take place during the measurements. Once the sample is mounted on the stage, the entire assembly is lowered into a beaker of electrolyte solution along with the Pt counter and standard calomel (SCE) reference electrodes. In this case, the gate bias and monitoring of leakage current were accomplished by using a Gamry Instruments model Reference600 potentiostat. Although the RT stage is not used, all of the electronics and control software for the RT thermopower rig discussed in Appendix B.3 are used for these experiments as well.

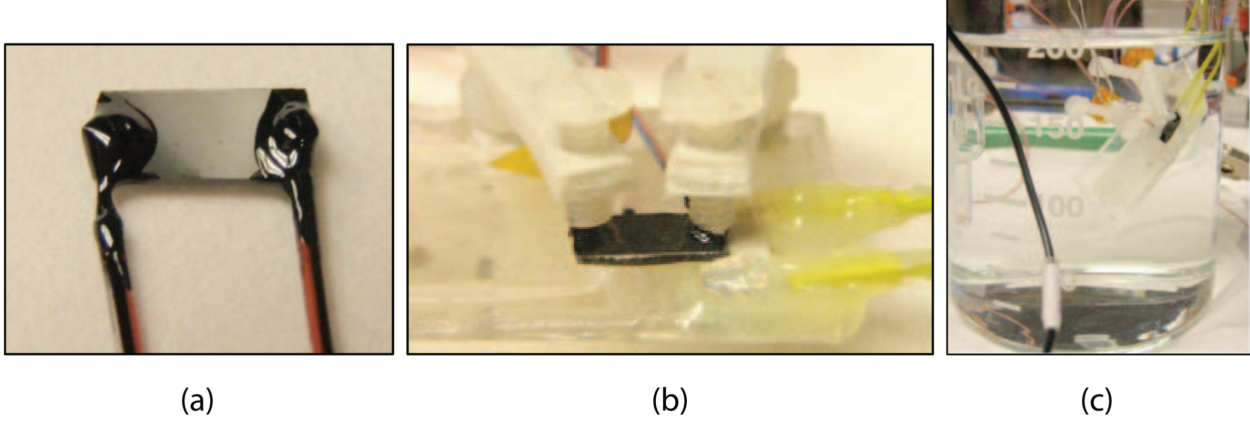


**Figure 5.2** Photographs of (a) an InN sample prepared for ETP measurements with thermocouples attached to either end and insulated with Pycene wax, (b) an InN sample mounted on the ETP stage, and (c) the entire ETP stage immersed in 1 M NaOH along with the Pt counter electrode and SCE reference electrode.

The results of initial ETP measurements are shown in Fig. 5.3 for two p-type samples and one n-type sample, although gate biases near the open circuit potential were applied to only one of the p-type samples.[a] Here the Seebeck coefficient is plotted as a function of gate bias. For the p-type sample plotted in green, applying a positive gate bias $V_G$ relative to the open circuit potential $V_{OC}$ results in an increasing Seebeck coefficient, which quickly saturates. Biasing in this direction depletes electrons from the surface inversion layer. Applying a negative gate bias relative to $V_{OC}$

[a] The open-circuit potential for InN in 1 M NaOH is typically negative, on the order of −0.3 V. This is the equilibrium potential between the sample and Pt counter electrode, given the existing surface band bending. It is not necessarily the same as in air or vacuum. This should be considered the “zero value” of the gate bias about which increases or decreases will cause modulation of the surface inversion layer conductivity.

results in a decreasing Seebeck coefficient by accumulating even more electrons into the inversion layer. For the n-type sample, modulation of the gate bias around $V_{OC}$ has no effect whatsoever on the Seebeck coefficient since the surface makes little contribution in a thick n-type sample. The control sample also gives confidence that the observed changes in the p-type sample are not an artifact due to the presence of the electrolyte. In all three samples at very large positive gate bias, the Seebeck coefficient increases dramatically, which is discussed below.

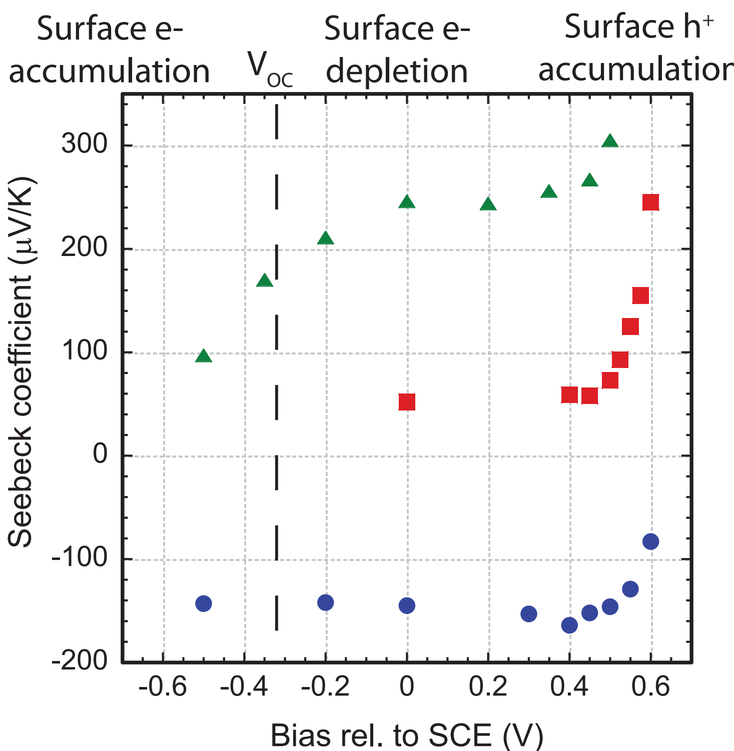


**Figure 5.3** Seebeck coefficient of two p-type samples (green and red) and one n-type sample (blue) as a function of gate bias. Here the open-circuit potential, $V_{OC}$, is marked indicating the near equilibrium state for these samples in a 1 M NaOH solution.

Although the polarity of the changes for the p-type sample are as expected, the magnitudes are much larger than expected. From the parallel conduction model and "known" properties of the inversion layer, changes of the Seebeck coefficient on the order of 1-10 % are expected, but instead, changes on the the order of 25-50% are observed. The reason for this is not well known at this time, but there are several possible explanations. It's possible that the "known" properties of the surface inversion layer are wrong, but this would require considerable reinterpretation of a great deal of experimental data, which seems unlikely. Another possibility is that the effect of the electrolyte gating on the redistribution of charge within the sample is more complicated than that shown in the simulations above; perhaps not just the surface layer is affected, resulting in more dramatic changes in Seebeck coefficient than expected. There is also the possibility that these changes are somehow an artifact due to leakage into the electrolyte or some kind of electrolytic conribution to the measured Seebeck coefficient (since the effective carrier concentration of the electrolyte is small, the Seebeck coefficient could be very large), although the fact that no effect is observed for the n-type sample would seem to rule out these artifactual possibilities.

Another curiosity is the dramatic increase in Seebeck coefficient for all three samples at very high gate bias. Again, this could be an artifact of some kind, especially since the blocking nature of the electrolyte contact is known to break down and leakage current begins to flow for gate biases beyond $\sim 0.6 - 0.7$ V. It's not known how current flow between the sample and electrolyte could result in such an effect, but it can't be ruled out at the moment. However, it's also possible that this is a real effect. It is known that for very large positive gate bias the surface electron accumulation can be completely depleted and holes can be brought to the surface; this would be a p-type inversion layer on n-type samples or a hole depletion layer on p-type samples. A layer of very low hole concentration would have a very large and positive Seebeck coefficient, possibly explaining this observation. By coupling simulations such as those shown in Fig. 5.1 with calculations of the thermopower using the parallel conduction model, the theoretical effect of varying the gate bias over these ranges could be assessed, which may shed some light on the unexplained results observed here. Increasing the data set to include more of both p-type and n-type samples may also help to solve these mysteries.

## 5.3 Electrolyte-gated IV measurements

For some in the InN field, the first demonstration of a pn-junction-based device in InN, such as a light emitting diode, is the "holy grail." Now that little controversy remains on the existence of p-type InN, the next step is to attempt to create pn junctions and demonstrate rectification within InN. Consider then a slab of InN, half n-type and half p-type, with a contact on each side. Ignoring for now that conducting threading dislocations may short the diode, the surface inversion layer around the outside of the sample may represent a significant path for parasitic current flow. This layer may short the diode and mask any rectification at the pn junction if it is less resistive than the current path through the bulk. Issues such as these are common in other materials where parasitic surface states may create a significant current path. In materials like GaAs, these problems are typically solvable by proper surface passivation treatments [156]. So far, nothing of this sort has been shown to work in InN [157–162]. However, it has been demonstrated that the surface inversion layer can be controlled using an electrolyte. Thus, it may be possible to turn off the parasitic surface current and expose the rectifying behavior of the bulk pn junction within, which is the topic of this section.

Using the pn junction samples available from Chapter 3, the ideal geometry for such a measurement is as shown in Fig. 5.4a where the n-type layer is directly contacted. This could be accomplished by *mesa* etching down to the n-type interlayer or by growing the n-type layer, masking off the contact pad, then growing the p-type layer. We will return to this idea later, but such sample geometry is not yet available. Though less controlled, another possible way to directly contact the n-type interlayer is to place a contact on top of a scratch through the film. An idealized version of this *scratch* method is shown in Fig. 5.4b. A third possible geometry is shown in Fig. 5.4c, where two contacts are placed on the surface and direct contact to the n-type layer is not expected. This one is labeled *double island* because, when the electrolyte is used to deplete the surface inversion layer, the two contacts are completely separated from any other n-type parts. Current-voltage (IV) measurements using both the scratch and double-island configurations were attempted. So far, the double-island configuration has produced the most interesting results, which will be discussed below. Note that Pycene wax (Apiezon W) is used to insulate the metal contacts and other areas such as the sample edges from being contacted by the electrolyte; this is illustrated in the diagrams by the black areas.

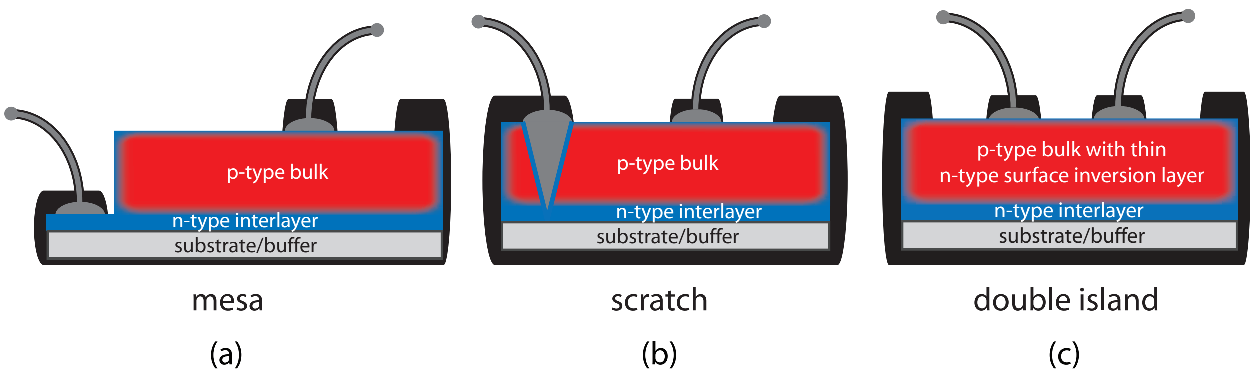


**Figure 5.4** Schematic illustrations of different possible measurement configurations for pn junction InN samples. (a) Ideal configuration, where the n-type layer is contacted directly, e.g. by mesa etching down to that layer. (b) Idealized illustration of directly contacting the n-type layer by simply putting a contact on top of a scratch in the film. Note that even the sidewalls of the scratch would likely be inverted. (c) Two surface contacts will ideally be completely disconnected (islanded) from the n-type surface and interlayer when depletion conditions are applied, as in Fig. 5.5a below. Note that all these scenarios ignore possible shorting by conducting threading dislocations.

Fig. 5.5 illustrates the double-island configuration in air and how the surface inversion layer is affected by immersing the structure in a 1 M NaOH solution and applying a bias through a Pt counter electrode. This is similar to the setup used for ECV measurements except that now the electrolyte is used as a gate electrode for IV measurements between the two sample contacts (the Source and Drain). Applying a gate bias $V_{\mathrm{G}}$ between the sample and Pt electrode modulates the surface inversion layer conductivity without passing a leakage current over $V_{\mathrm{G}} \sim \pm 0.4$ V, as shown in Appendix D. For negative $V_{\mathrm{G}}$, even more electrons are drawn into the surface inversion layer. For positive $V_{\mathrm{G}}$, the surface inversion layer is depleted until eventually p-type material comes all the way to the surface. Under this condition, the surface short between the two contacts is eliminated and current must flow through the bulk of the film. At least this is the desired condition; interpreting the data and identifying the actual current path will be less straightforward. Because the electrolyte does not affect the surface layer under the contact (or anywhere coated with wax), a $n^+$ surface inversion layer persists in the area directly under each contact.

IV measurements, current between source and drain $I_{\mathrm{SD}}$ vs. voltage between source and drain $V_{\mathrm{SD}}$, for a p-type sample in the double island configuration for different values of the gate bias $V_{\mathrm{G}}$ are shown in Fig. 5.6a. The IV characteristics are shown to diverge significantly from the completely linear (Ohmic) IV measurement in air and depend strongly on the gate bias. In accumulation condition (negative $V_{\mathrm{G}}$) the IV curves are asymmetric and kinked near zero source-drain bias. In depletion condition (positive $V_{\mathrm{G}}$), the IV curve takes on a mostly symmetric s-shape, blocking somewhat in both forward (+) and reverse (-) source-drain bias. The explanation for such a promising result may be that in depletion the current path flows from the $n^+$ region under the first contact, through the p-type bulk and into the $n^+$ region under the second contact, as discussed more below. It should be emphasized at this time that neither rectification nor any kind of non-Ohmic transport had ever been observed before in InN, not even Schottky contacts. Similar measurements for a fully n-type sample are shown in Fig. 5.6b. In contrast, only Ohmic character is observed with very weak dependence on gate bias. This gate bias dependence is as expected; when in accumulation

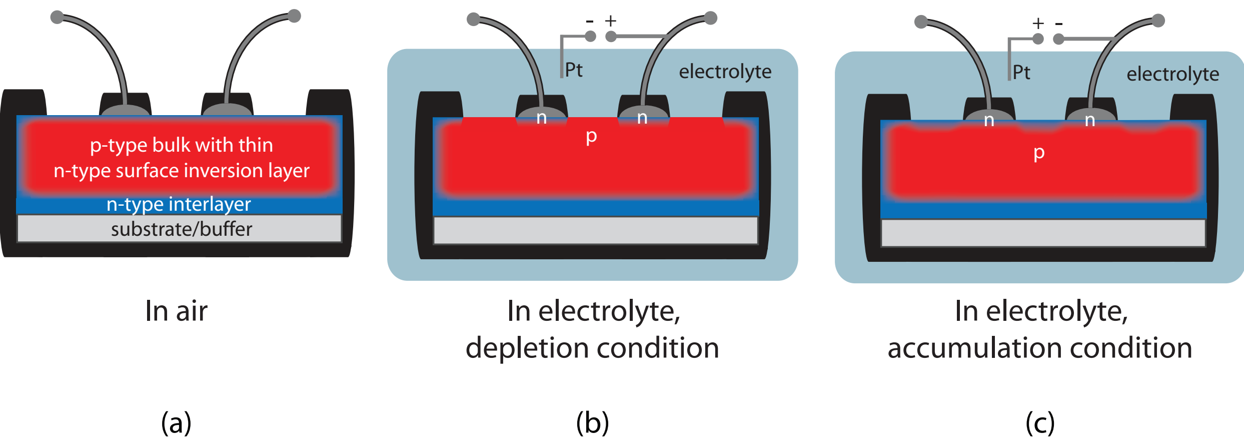


**Figure 5.5** Schematic illustrating the regions of n- and p-type conductivity for a sample contacted in the double island configuration (a) in air, (b) in an electrolyte with sufficiently positive gate bias such that the surface inversion layer is depleted, and (c) in an electrolyte with sufficiently negative gate bias such that even more electrons are drawn into the surface inversion layer.

condition more electrons are drawn into the surface layer and the resistance decreases slightly, in depletion fewer electrons are in the surface layer and resistance increases slightly. The dependence is weak because most of the current flows through the bulk in a fully n-type sample.

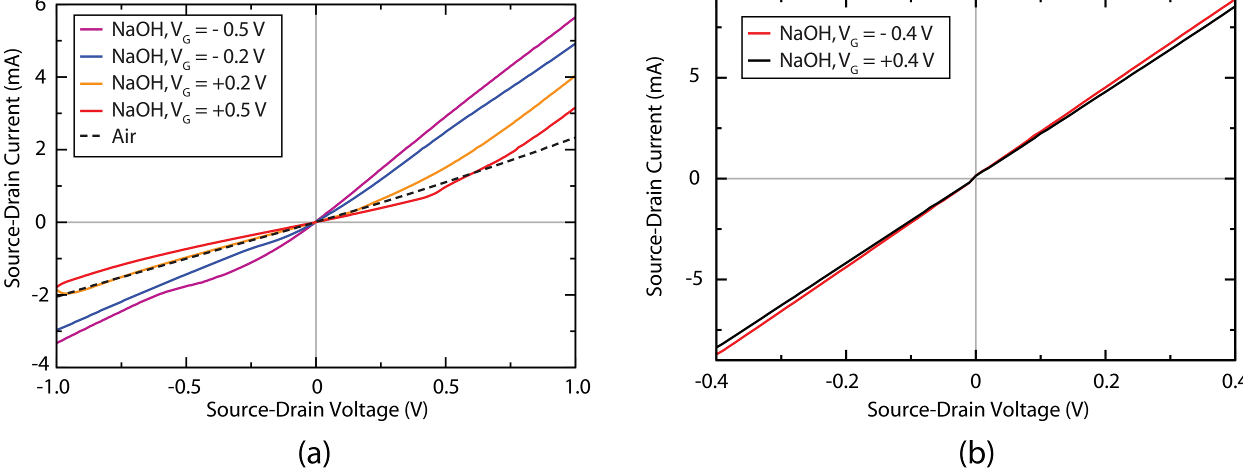


**Figure 5.6** (a) Comparison of $I_{\mathrm{SD}}V_{\mathrm{SD}}$ measurements of a p-type sample (S599) in air and in a NaOH solution with positive and negative gate bias $\mathrm{V_G}$. (b) Comparison of $\mathrm{I_{SD}V_{SD}}$ measurements of a n-type sample (S596) in a NaOH solution with positive and negative gate bias $\mathrm{V_G}$.

If the current path in the depletion condition is flowing through $\mathrm{n^+}$-p and p-$\mathrm{n^+}$ junctions, that are actually somewhat blocking, then forward current through each junction is dominated by the thermally activated diffusion current, which would be expected to respond to temperature. The current over an energy barrier $\phi_{\mathrm{B}}$ depends exponentially on the ratio of barrier height to thermal energy of the carriers, which is the well known Arrhenius relationship $J_{\mathrm{diff}} \propto e^{(-\phi_{\mathrm{B}}/k_{\mathrm{B}}T)}$. Thus, the IV curves should respond to temperature, being more blocking at low temperature and less blocking at higher temperature. Such measurements in this case are limited by the phase space of

the aqueous NaOH solution, being liquid over only $\sim 0 - 100$ °C. However, as shown in Fig. 5.7, due to the exponential relationship even a small temperature difference can have a large effect. Here the IV curve in depletion condition is shown to depend very strongly on temperature, passing less current at low temperature and more current at high temperature. At 5 °C, the structure is blocking over nearly $\pm 1$ V; at 76 °C, nearly Ohmic character has returned.

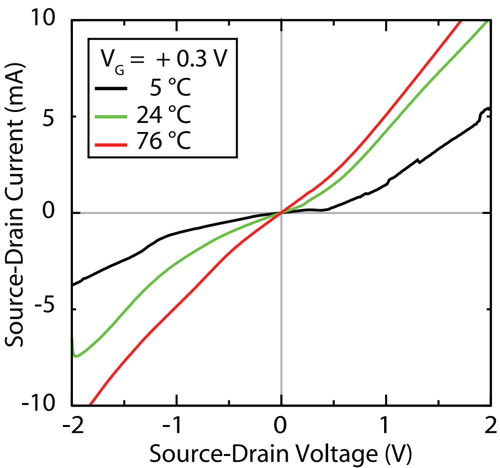


**Figure 5.7** Comparison of $I_{SD}V_{SD}$ measurements of a p-type sample (S599) in a NaOH solution at different temperatures under surface depletion conditions: gate bias $V_G = +0.3$V.

The data shown here represents only a small portion of the many electrolyte-gated IV measurements conducted on this sample, S599, including those with $V_{SD}$ as high as $\pm 3$ V and gate bias as high as $\pm 0.5$ V. Initially no changes to the sample could be detected visibly, but after many of these measurements including the higher potentials listed, the sample began to show signs of changes to the surface. Accidentally etching InN in electrolyte-based experiments such as these is very common; the positive gate bias direction brings holes to the surface, which, as broken bonds, make the sample susceptible to etching. A silvery haze was visible on the surface, which could be caused by excess In due to the release of N atoms during etching, due to the deposition of some kind of reaction product, or simply due to roughening of the surface, though the exact nature of the surface changes is unknown at this time.[b] The sample was then retested in air and remarkably some of the non-Ohmic character was retained even in the absence of the electrolyte, as shown in Fig. 5.8. This observation is important for two reasons. First, it proves beyond any doubt that the non-Ohmic character to the IV measurements is due to current flow in the sample rather than to some kind of artifact due to current flow in the electrolyte. Second, it implies that it is possible to alter InN surfaces in such a way that the surface inversion layer is at least semi-permanently depleted. Speculation at this time is that the surface states were at least partially passivated by whatever changes occurred to the surface during the measurements.

Earlier, it was proposed that the observed IV characteristics could possibly be due to a $n^+$-p-$n^+$ current path, i.e. due to current flowing through two back to back pn junctions. These pn junctions must be rather leaky, or else current flow would be small in both directions. The equivalent circuit proposed to represent this situation and the results of different shunt path scenarios are shown in

[b]Subsequent treatment with HCl removed some but not all of this haze, suggesting that it was not entirely due to excess In on the surface.

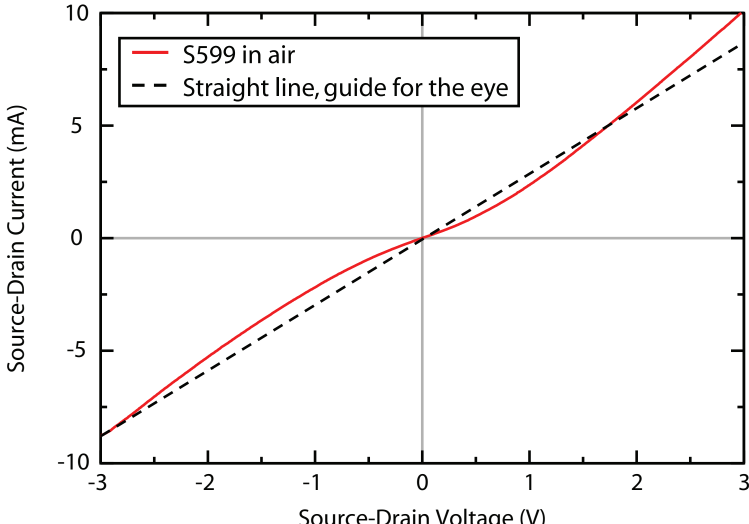


**Figure 5.8** $I_{SD}V_{SD}$ measurement of p-type sample (S599) in air after many measurements under electrolyte showing significant residual non-Ohmic character. The dashed line is simply a straight line drawn as a guide for the eye. Comparison of the measurement to the dashed line illustrates that the data is nonlinear and asymmetric.

Fig. 5.9.[c] In Fig. 5.9a, the equivalent circuit consists of two diodes (D1 and D2) facing opposite directions representing the pn and np junctions, a series resistor in between them (R5) representing the resistance of bulk transport through the film, and shunt resistors around each diode (R3 and R4) representing the diode leakage paths. The surface inversion layer is expected to represent a significant shunting path, which should respond to gate bias, but it may not be the only source of shunting. As shown in Fig. 5.9b, IV curves qualitatively similar to those shown in Fig. 5.6a for S599 can be simulated by proper choice of the shunt resistance values. When both shunt resistors are large (as in when the surface layer is depleted), a symmetric s-shaped IV curve results that is somewhat blocking for both forward and reverse source-drain bias. When one is small and the other large, a non-symmetric but mostly linear IV curve results. In order to increase the current at all biases, as observed in accumulation condition for S599, the shunt resistors are made small and unequal. The reason for unequal shunt paths in accumulation condition is not yet known, but could possibly be due to sample inhomogeneity of one form or another, possibly variable density of conducting dislocations. Perhaps more likely is that the high current at positive source-drain bias causing the asymmetry is partially due to an artifact of current flowing through the electrolyte. It's possible that the blocking behavior is real, as seems to be clear, while some of the large currents are artifacts. Some basic tests of the electrolyte itself are planned, which should shed some light on this issue.

Since the claim of the first observation of rectification in InN is a tremendous one, much effort should be directed at reproducing the observation. Two more p-type samples, similar to S599 were prepared and evaluated. Measurements on these samples are qualitatively similar to one another, but somewhat different from the behavior of S599, as shown in Fig. 5.10. In these films, the IV curves are asymmetric and respond strongly to gate bias, but the blocking s-curve is never

[c]Circuit analysis and performed using the student version of PSpice, http://www.electronics-lab.com/downloads/schematic/013/.

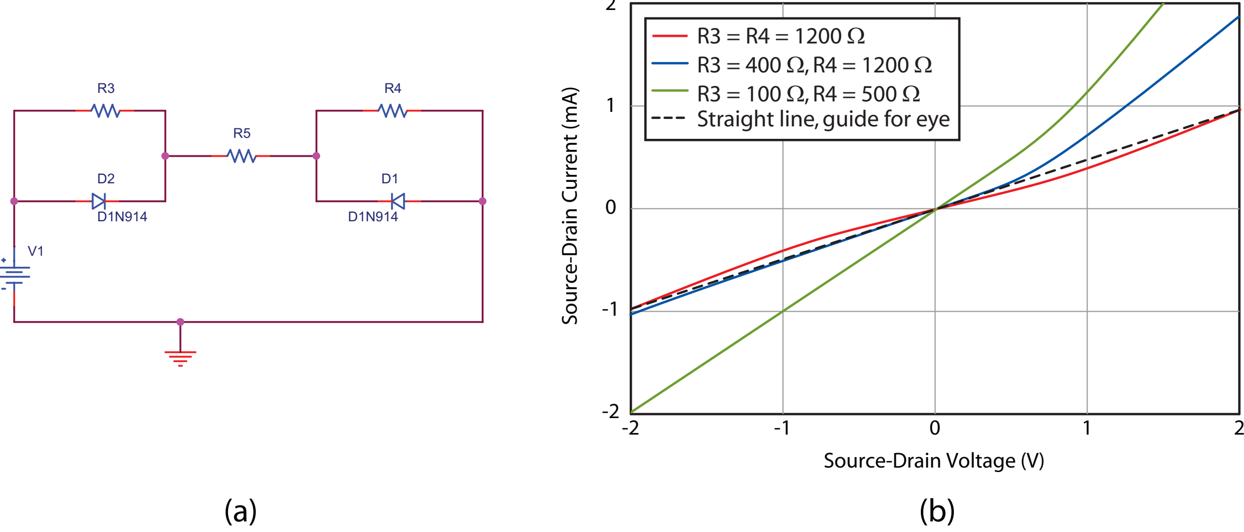


**Figure 5.9** (a) Diagram of proposed equivalent circuit explaining the IV data for p-type InN films with two surface contacts, such as shown in Fig. 5.6a. (b) Results of modeling using the circuit shown in (a) for three different scenarios for the values of the shunt resistors R3 and R4. The dashed line is simply a straight line as a guide for the eye.

observed. Instead, no matter whether in accumulation or depletion condition, the shape of the curves are similar to the shape of S599 in accumulation condition. Applying more positive gate bias only shifts the "turn-on" kink to larger source-drain bias. This behavior is not yet understood and measurements continue on this issue. It's likely that greater statistics in the form of larger numbers of samples and larger numbers of smaller contacts may help in this regard, as it seems that not all contacts to these samples are alike.

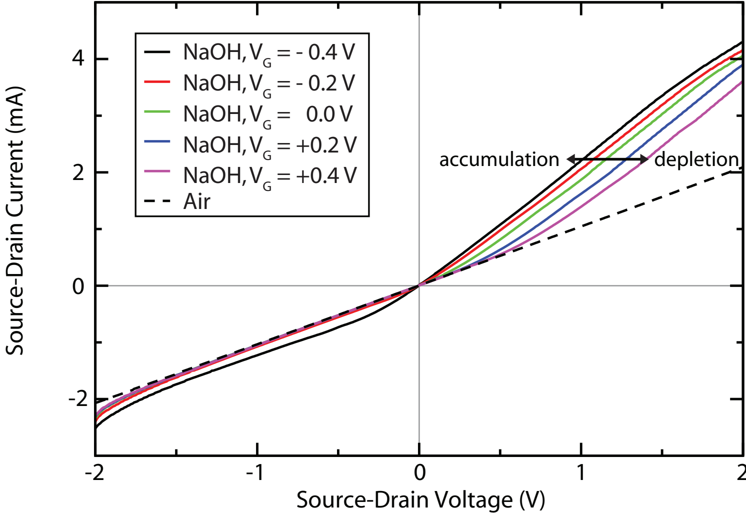


**Figure 5.10** Comparison of $I_{SD}V_{SD}$ measurements of a different p-type sample (S665) in air and in a NaOH solution with positive and negative gate bias $V_G$.

Worth further effort is understanding the potential at each point in the system. Consider the

situation where a source-drain bias of 3 V is applied and a positive 0.4 V gate bias is maintained to push the surface into depletion condition. The simplest case is that the potential drops linearly through the sample from one contact to the other; then the +0.4 V gate bias condition only applies right next to the source contact, and the gate bias changes linearly with distance between the contacts until at some point it switches over and the sample is actually at lower potential than the gate. This only occurs because the source-drain bias is larger than the gate bias. It may also not be entirely realistic, but the consequences should definitely be considered. In the area closer to the drain the surface is actually in accumulation for some distance, which would imply that the $n^+$ surface region there actually extends beyond the contact. Thus, the surface short is depleted for only part of the distance between the two contacts and this distance is a function of the source-drain bias. Such effects are certainly not encompassed by the simple equivalent circuit model of Fig. 5.9a and all the ramifications of such effects may not be straightforward. These second-order considerations definitely deserve more thought and may be better addressed through the use of finite element modeling.

Another consideration, is that this double island geometry is not ideal. At best, an $n^+$-p-$n^+$ current path results and the bulk pn junction in the sample is probably not involved. Ultimately, it may be difficult to interpret the results fully and prove exactly what is the true current path in this configuration. And because the surface inversion layer has such a high electron concentration, most if not all of the depletion at the $n^+$-p junctions occurs on the p-side; although still an important advance, technically this is more akin to a Schottky contact than a true pn junction. A better situation is as shown in Fig. 5.4a where the bulk n-type layer is directly contacted on one side. In this case, the bulk pn junction, with depletion on both sides of the junction, could be involved in the current path if the shorting current flow around the edge of the sample could be made low enough by electrolyte-gating or other means. The results from this configuration may be easier to interpret, and demonstrating rectification at a bulk pn junction will be more important on the path towards the first InN devices.

Although this project is as yet incomplete, the initial results are very encouraging and some important conclusions can already be made. IV measurements through p-InN samples can be modulated by the application of gate bias using a blocking electrolyte contact. For some samples, depletion of the surface inversion layer seems to be possible, and blocking IV curves result. Simple modeling of these curves implies that a current is flowing through two back to back, leaky, rectifying pn junctions in InN. This blocking behavior responds strongly to temperature, and in one case was observed to persist in air, hinting that semi-permanent passivation of InN surface states may be possible. With or without electrolyte gating, these results indicate that InN-based pn junction devices may indeed be possible in the near future.

# Chapter 6

# Conclusions and future work

The development of thermopower measurements for the study of p-type InN has been significant, offering new insights and providing a new tool, which is now in use by several groups worldwide. Positive Seebeck coefficients have been measured for many samples now, offering definitive proof of free-hole conduction and therefore truly p-type InN. The variation of Seebeck coefficient with Mg doping concentration has revealed a window of p-type conductivity, bound on both sides by the dominance of donor type defects. With increasing Mg content, the first transition is reached where the Seebeck coefficient becomes positive when the free hole concentration outnumbers the large background density of electrons. At the same time, the photoluminescence intensity is rapidly decreasing, disappearing completely shortly after positive Seebeck coefficients are reached, which is attributed to the opening of nonradiative recombination pathways as the Fermi level drops towards the valence band. But before the PL quenches, a Mg-related emission peak is observed below the band-to-band peak, which yields the Mg acceptor ionization energy of 61 meV. The Seebeck coefficient peaks and begins to drop until the second transition is reached and electron conduction becomes dominant again. This second transition is attributed to the formation of compensating Mg defect complexes and the formation of extended defects at high Mg concentrations.

At least two features of this work remain unexplored. The temperature dependence of the thermopower of these p-type films is for the most part uninteresting, but there are a few unique films that exhibit a nonlinear temperature dependence. This variation with temperature is most likely due to the underlying variation of the hole mobility with temperature. More detailed analysis of this data, along with temperature dependent Hall data, could yield some very important information about hole transport and Mg ionization. Another interesting idea is to search for some direct sign of the midgap defect states that are invoked without experimental evidence to explain the behavior of the PL intensity with increasing Mg content. Direct optical measurement of these purported mid-gap states, by means of fourier transform infrared spectroscopy (FTIR PL) or a similar technique, could provide great insight. As the study of deep levels in semiconductors is very mature, one is tempted to simply apply one of the myriad deep level spectroscopy techniques to search for these states electrically, but these require pn junctions, Schottky contacts, or resistive samples, which are still unobtainable in InN. The application of spectroscopic techniques, such as photothermal ionization spectroscopy (PTIS), to the study of the shallow acceptors in InN is also completely unexplored.

While investigating the effects of Mg doping, a model was brought to bear on the mystery of how a positive Seebeck coefficient could be observed while only contacting the n-type surface layer of an InN film, or more generally, how the various conducting layers of InN contribute to the

measured Seebeck coefficient. The finding that these layers contribute as if conducting in parallel and Ohmically connected at their ends, has helped to understand the Mg doping dependence to the thermopower data. But it also suggested another experiment; a systematic variation of the structure's layers could help to resolve properties of those individual layers from the composite bulk measurement. This idea has been developed and used to extract the free hole concentration and mobility from two series of samples with a variable thickness n-type interlayer. Free hole concentrations on the order of $10^{19}$ $cm^{-3}$ and hole mobilities of 3-14 $cm^2/Vs$ are deduced from the analysis, providing quantitative assessments of these parameters where many other techniques, including the Hall effect, have failed. The self-consistent modeling of thermopower and Hall effect data using parallel conduction models has also strengthened the case for poor junction isolation at InN pn junctions. The analogous experiment to this one, in which the thickness of the interlayer is held constant and the thickness of the p-layer is varied, is currently underway. This experiment may help to understand how the hole conduction properties of InN change as a function of thickness, and indirectly how they change with point and extended defect densities.

Investigating the role of extended defects such as dislocations on electron transport is much easier since the Hall effect can be used directly on n-type InN. In fact both Hall effect and thermopower are sensitive to scattering mechanisms. Using both of these transport coefficients, along with extensive modeling using the Boltzmann transport equation, it is shown that dislocations are very likely positively charged donors in InN and act as strong Coulombic scattering centers. By self-consistently modeling the Seebeck coefficient and mobility as a function of temperature, the density of threading dislocations was predicted with near-perfect agreement to independent measurement. Modeling showed that the mobility of InN is in some cases dominated by dislocation scattering, and is even more important for low electron concentrations where the protective effect of screening is diminished. Therefore, the future of InN devices where electron concentrations are even lower than today, will require that efforts be made to reduce threading dislocation densities. The possibility that threading dislocations are charged and act as conducting wires, possibly shorting pn junctions, further demands the reduction of dislocation density for future devices. Threading dislocations are very likely optically active as well and may play a role in the quenching of PL for p-type InN. However, no one has yet observed a charged dislocation in InN, and much is unknown about their nature. Are all dislocations charged? How much are they charged? Are the dislocations intrinsically charged or decorated by point defects? Is the case different for n- and p-type InN? These are all questions that may be answered by surface and electron microscopy techniques capable of directly imaging the charge on dislocations. Understanding the nature of such defects in InN is completely unexplored and ripe for investigation.

Finally, the early stages of two experiments are described in which an electrolyte is used to gate the surface inversion layer on p-type InN films. The first takes advantage of this technique with the hope of directly controlling the thermoelectric contribution of the surface layer to the measured composite value so that it can be measured and removed from the analysis. The preliminary results are promising in that the thermopower of a p-type sample was shown to be very sensitive to the gating process, while the thermopower of an n-type sample was not. However, the magnitude of the changes observed on the p-type sample far exceeded expectations and questions remain about the possible involvement of the electrolyte or gate leakage in augmenting the thermopower measurements. Nonetheless, this is a promising direction of research that deserves more effort.

The second experiment aims to deplete the surface inversion layer so that parasitic currents flowing through it will be eliminated and the rectifying behavior of a bulk pn junction can be revealed. The preliminary results of this experiment are even more promising than the last; the

IV curves of p-type samples are shown to be very sensitive to electrolyte biasing while those of n-type samples are not. For the first time, non-Ohmic IV behavior is observed in InN, which is attributed to rectification at back-to-back leaky diodes. Non-Ohmic IV behavior is even observed in air, suggesting possibly that the process made changes to the InN surface that at least partially depleted the surface inversion layer and were at least somewhat permanent. Going forward, basic measurements of the electrolyte and more samples will help to answer questions about the method and the nature of these contacting schemes. A mesa geometry is proposed for future measurements, which may ease the process of determining the current path through the structure and if successful will involve current flow through a bulk pn junction for the first time. If this can be accomplished, it would be interesting to attempt to measure electroluminescence from this structure, which would truly be a breakthrough for InN.

The basic transport properties of InN are now mostly understood as are the basic band structure properties and the nature of defects although much is still to be learned about hole transport and p-type conductivity. The minimum achievable electron concentration has been stagnant over the last several years, hovering around $10^{17}$ $cm^{-3}$ but never much below. Making the advances at reducing the electron concentration will take better control over the growth process and better understanding of the role of extended defects such as threading dislocations, stacking faults, and inversion domains, all of which may also be donors in InN. The day when InN is no longer a scientific curiosity and becomes a viable material for device applications is approaching, but significant challenges remain, least among them contacting p-type InN. With the intense interest in smaller bandgap group III-N materials for optoelectronic applications, many of the challenges of InN may be tackled first for the alloys containing a significant fraction of Ga or Al, then later for more In-rich material. The worldwide community of researchers investigating InN is still very small, and advances will come slowly but surely. Yet it remains an open question how useful this intriguing material will ever be for practical devices.

# References


[1] Oda, O. *Compound Semiconductor Bulk Materials and Characterizations.* World Scientific, (2007).

[2] Faraday, M. *Experimental Researches in Electricity*, volume I. Bernand Quaritch, (1839).

[3] Computer History Museum, Mountain View, CA. The Silicon Engine: A Timeline of Semiconductors in Computers: http://www.computerhistory.org/semiconductor/timeline.html.

[4] Becquerel, A. E. *Comtes Rendus de lAcademie des Sciences* **9**, 31–33 (1839).

[5] Nakamura, S., Mukai, T., and Senoh, M. *Japanese Journal of Applied Physics* **30**(12A), L1998–L2001 (1991).

[6] Nakamura, S. *J. Vac. Sci. Technol. A* **13**(3), 705–710 (1995).

[7] Nakamura, S. *Science* **281**(5379), 956 (1998).

[8] Nakamura, S. and Chichibu, S. F. *Introduction to Nitride Semiconductor Blue Lasers and Light Emitting Diodes.* Taylor and Francis, (2000).

[9] Aryal, K., Pantha, B. N., Li, J., Lin, J. Y., and Jiang, H. X. *Appl. Phys. Lett.* **96**(5), 052110 (2010).

[10] Avramescu, A., Lermer, T., Müller, J., Tautz, S., Queren, D., Lutgen, S., and Strauß, U. *Appl. Phys. Lett.* **95**, 071103 (2009).

[11] Wu, J., Walukiewicz, W., Yu, K. M., Shan, W., Ager III, J. W., Haller, E. E., Lu, H., Schaff, W. J., Metzger, W. K., and Kurtz, S. *J. Appl. Phys.* **94**, 6477 (2003).

[12] Pantha, B. N., Sedhain, A., Li, J., Lin, J. Y., and Jiang, H. X. *Appl. Phys. Lett.* **95**, 261904 (2009).

[13] Dahal, R., Pantha, B., Li, J., Lin, J. Y., and Jiang, H. X. *Appl. Phys. Lett.* **94**(6), 063505 (2009).

[14] Wu, J. *J. Appl. Phys.* **106**, 011101 (2009).

[15] Fujii, K., Ono, M., Ito, T., Iwaki, Y., Hirako, A., and Ohkawa, K. *J. Electrochem. Soc.* **154**(2), B175–B179 (2007).

[16] Tansley, T. L. and Foley, C. P. *J. Appl. Phys.* **59**, 3241 (1986).

[17] Walukiewicz, W., Ager III, J. W., Yu, K. M., Liliental-Weber, Z., Wu, J., Li, S. X., Jones, R. E., and Denlinger, J. D. *J. Phys. D: Appl. Phys.* **39**(5), R83–R99 (2006).

[18] Hovel, H. J. and Cuomo, J. J. *Appl. Phys. Lett.* **20**(2), 71–73 (1972).

[19] Lu, H., Schaff, W. J., Hwang, J., Wu, H., Koley, G., and Eastman, L. F. *Appl. Phys. Lett.* **79**, 1489 (2001).

[20] Nanishi, Y., Saito, Y., and Yamaguchi, T. *Japanese Journal of Applied Physics* **42**(Part 1, No. 5A), 2549–2559 (2003).

[21] Davydov, V. Y., Klochikhin, A. A., Seisyan, R. P., Emtsev, V. V., Ivanov, S. V., Bechstedt, F., Furthmuller, J., Harima, H., Mudryi, A. V., and Aderhold, J. *Phys. Status Solidi B* **229**(3) (2002).

[22] Wu, J., Walukiewicz, W., Yu, K. M., Ager III, J. W., Haller, E. E., Lu, H., Schaff, W. J., Saito, Y., and Nanishi, Y. *Appl. Phys. Lett.* **80**, 3967 (2002).

[23] Sugita, K., Takatsuka, H., Hashimoto, A., and Yamamoto, A. *Physica Status Solidi (B)* **240**(2), 421 (2003).

[24] Burstein, E. *Phys. Rev.* **93**(3), 632–633 Feb (1954).

[25] Moss, T. S. *Proc. Phys. Soc. London B* **76**, 775 (1954).

[26] Wu, J., Walukiewicz, W., Li, S. X., Armitage, R., Ho, J. C., Weber, E. R., Haller, E. E., Lu, H., Schaff, W. J., and Barcz, A. *Appl. Phys. Lett.* **84**, 2805 (2004).

[27] Gallinat, C. S., Koblmüller, G., Brown, J. S., Bernardis, S., Speck, J. S., Chern, G. D., Readinger, E. D., Shen, H., and Wraback, M. *Appl. Phys. Lett.* **89**, 032109 (2006).

[28] Schley, P., Goldhahn, R., Gobsch, G., Feneberg, M., Thonke, K., Wang, X., and Yoshikawa, A. *Phys. Status Solidi B* **246**, 1177 (2009).

[29] Martin, G., Botchkarev, A., Rockett, A., and Morkoç, H. *Appl. Phys. Lett.* **68**, 2541 (1996).

[30] Wu, C. L., Lee, H. M., Kuo, C. T., Gwo, S., and Hsu, C. H. *Appl. Phys. Lett.* **91**, 042112 (2007).

[31] King, P. D. C., Veal, T. D., Kendrick, C. E., Bailey, L. R., Durbin, S. M., and McConville, C. F. *Physical Review B (Condensed Matter and Materials Physics)* **78**(3), 033308 (2008).

[32] Walukiewicz, W. *Appl. Phys. Lett.* **54**, 2094 (1989).

[33] Walukiewicz, W. *Physica B: Physics of Condensed Matter* **302**, 123 (2001).

[34] Mönch, W. *Semiconductor surfaces and interfaces.* Springer Verlag, (2001).

[35] Mahboob, I., Veal, T. D., Piper, L. F. J., McConville, C. F., Lu, H., Schaff, W. J., Furthmüller, J., and Bechstedt, F. *Phys. Rev. B* **69**(20), 201307 (2004).

[36] Zhang, S. B., Wei, S. H., and Zunger, A. *J. Appl. Phys.* **83**, 3192 (1998).

[37] Fritsch, D., Schmidt, H., and Grundmann, M. *Phys. Rev. B* **69**(16), 165204 Apr (2004).

[38] Van de Walle, C. G. and Neugebauer, J. *Nature* **423**(6940), 626–628 (2003).

[39] Takei, Y. and Nakayama, T. *J. Cryst. Growth* **311**, 2767 (2009).

[40] Li, S. X., Yu, K. M., Wu, J., Jones, R. E., Walukiewicz, W., Ager III, J. W., Shan, W., Haller, E. E., Lu, H., and Schaff, W. J. *Phys. Rev. B* **71**(16), 161201 (2005).

[41] Emtsev, V., Davydov, V. Y., Klochikhin, A. A., Sakharov, A. V., Smirnov, A. N., Kozlovskii, V., Wu, C. L., Shen, C. H., and Gwo, S. *physica status solidi (c)* **4**(7) (2007).

[42] Li, S. X., Jones, R. E., Haller, E. E., Yu, K. M., Walukiewicz, W., Ager III, J. W., Liliental-Weber, Z., Lu, H., and Schaff, W. J. *Appl. Phys. Lett.* **88**, 151101 (2006).

[43] Jones, R. E., Li, S. X., Hsu, L., Yu, K. M., Walukiewicz, W., Liliental-Weber, Z., Ager III, J. W., Haller, E. E., Lu, H., and Schaff, W. J. *Physica B: Physics of Condensed Matter* **376**, 436 (2006).

[44] Lu, H., Schaff, W. J., Eastman, L. F., and Stutz, C. E. *Appl. Phys. Lett.* **82**, 1736 (2003).

[45] Mahboob, I., Veal, T. D., McConville, C. F., Lu, H., and Schaff, W. J. *Phys. Rev. Lett.* **92**, 036804 (2004).

[46] Cimalla, V., Niebelschütz, M., Ecke, G., Lebedev, V., Ambacher, O., Himmerlich, M., Krischok, S., Schaefer, J. A., Lu, H., and Schaff, W. J. *Physica Status Solidi A* **203**(1), 59–65 (2006).

[47] Klochikhin, A. A., Davydov, V. Y., Strashkova, I. Y., and Gwo, S. *Phys. Rev. B* **76**(23), 235325 (2007).

[48] Veal, T. D., Piper, L. F. J., Mahboob, I., Lu, H., Schaff, W. J., and McConville, C. F. *Physica Status Solidi C* **2**, 2246–2249 (2005).

[49] Piper, L. F. J., Veal, T. D., McConville, C. F., Lu, H., and Schaff, W. J. *Appl. Phys. Lett.* **88**, 252109 (2006).

[50] Wang, H., Jiang, D. S., Wang, L. L., Sun, X., Liu, W. B., Zhao, D. G., Zhu, J. J., Liu, Z. S., Wang, Y. T., Zhang, S. M., and Yang, H. *J. Phys. D: Appl. Phys.* **41**(13), 135403 (2008).

[51] Lebedev, V., Cimalla, V., Baumann, T., Ambacher, O., Morales, F. M., Lozano, J. G., and Gonzlez, D. *J. Appl. Phys.* **100**, 094903 (2006).

[52] Wang, X., Che, S. B., Ishitani, Y., and Yoshikawa, A. *Appl. Phys. Lett.* **90**, 151901 (2007).

[53] Wang, K. A., Cao, Y., Simon, J., Zhang, J., Mintairov, A., Merz, J., Hall, D., Kosel, T., and Jena, D. *Appl. Phys. Lett.* **89**(16), 162110 (2006).

[54] Yu, X.-G. and Liang, X.-G. *J. Appl. Phys.* **103**(4), 043707 (2008).

[55] Look, D. C., Lu, H., Schaff, W. J., Jasinski, J., and Liliental-Weber, Z. *Appl. Phys. Lett.* **80**, 258 (2002).

[56] Gallinat, C. S., Koblmüller, G., and Speck, J. S. *Appl. Phys. Lett.* **95**(2), 022103 (2009).

[57] Kane, E. O. *J.Phys.Chem.Solids* **1**, 249 (1957).

[58] Zawadzki, W. and Szymańska, W. *Physica Status Solidi (b)* **45**(2), 415 (1971).

[59] Wu, J., Walukiewicz, W., Shan, W., Yu, K. M., Ager III, J. W., Haller, E. E., Lu, H., and Schaff, W. J. *Phys. Rev. B* **66**(20), 201403 (2002).

[60] Fu, S. P. and Chen, Y. F. *Appl. Phys. Lett.* **85**(9), 1523–1525 (2004).

[61] Chang, Y.-M., Chu, H. W., Shen, C.-H., Chen, H.-Y., and Gwo, S. *Appl. Phys. Lett.* **90**(7), 072111 (2007).

[62] Hofmann, T., Darakchieva, V., Monemar, B., Lu, H., Schaff, W. J., and Schubert, M. *J. Electron. Mater.* **37**(5), 611–615 (2008).

[63] Inushima, T., Fukui, K., Lu, H., and Schaff, W. J. *Appl. Phys. Lett.* **92**, 171905 (2008).

[64] Takeuchi, D., Kato, H., Ri, G. S., Yamada, T., Vinod, P. R., Hwang, D., Nebel, C. E., Okushi, H., and Yamasaki, S. *Appl. Phys. Lett.* **86**, 152103 (2005).

[65] Qi, D., Gao, X., Wang, L., Chen, S., Loh, K. P., and Wee, A. T. S. *Chem. Mater.* **20**(21), 6871–6879 (2008).

[66] Veal, T. D., Piper, L. F. J., Schaff, W. J., and McConville, C. F. *J. Cryst. Growth* **288**(2), 268–272 (2006).

[67] Hall, E. H. *Am. J. Math.* **2**, 287 (1879).

[68] van der Pauw, L. J. *Philips Tech. Rev.* **20**, 220 (1958).

[69] van der Pauw, L. J. *Philips Res. Rep.* **13**, 1 (1958).

[70] Jones, R. E., Yu, K. M., Li, S. X., Walukiewicz, W., Ager III, J. W., Haller, E. E., Lu, H., and Schaff, W. J. *Phys. Rev. Lett.* **96**(12), 125505 (2006).

[71] Wang, X., Che, S. B., Ishitani, Y., and Yoshikawa, A. *Appl. Phys. Lett.* **92**, 132108 (2008).

[72] Chen, F., Cartwright, A. N., Lu, H., and Schaff, W. J. *Appl. Phys. Lett.* **87**(21), 212104 (2005).

[73] Yeo, Y. C., Chong, T. C., and Li, M. F. *J. Appl. Phys.* **83**(3), 1429–1436 (1998).

[74] Miller, N., Ager III, J. W., Smith III, H. M., Mayer, M. A., Yu, K. M., Haller, E. E., Walukiewicz, W., Schaff, W. J., Gallinat, C., Koblmüller, G., and Speck, J. S. *J. Appl. Phys.* **107**, 113712 (2010).

[75] Anderson, P. A., Swartz, C. H., Carder, D., Reeves, R. J., Durbin, S. M., Chandril, S., and Myers, T. H. *Appl. Phys. Lett.* **89**, 184104 (2006).

[76] Dmowski, L. H., Baj, M., Suski, T., Przybytek, J., Czernecki, R., Wang, X., Yoshikawa, A., Lu, H., Schaff, W. J., Muto, D., and Nanishi, Y. *J. Appl. Phys.* **105**(12), 123713 (2009).

[77] Johnson, S. M., Rhiger, D. R., Rosbeck, J. P., Peterson, J. M., Taylor, S. M., and Boyd, M. E. *Journal of Vacuum Science & Technology B: Microelectronics and Nanometer Structures* **10**, 1499 (1992).

[78] Baker, I. M. and Maxey, C. D. *J. Electron. Mater.* **30**(6), 682–689 (2001).

[79] Tsukamoto, H., Chen, E.-H., Woodall, J. M., and Gopal, V. *Appl. Phys. Lett.* **78**(7), 952–954 (2001).

[80] Jasinski, J. and Liliental-Weber, Z. *J. Electron. Mater.* **31**, 429 (2002).

[81] Lebedev, V., Cimalla, V., Pezoldt, J., Himmerlich, M., Krischok, S., Schaefer, J. A., Ambacher, O., Morales, F. M., Lozano, J. G., and González, D. *J. Appl. Phys.* **100**, 094902 (2006).

[82] Cimalla, V., Lebedev, V., Morales, F. M., Goldhahn, R., and Ambacher, O. *Appl. Phys. Lett.* **89**, 172109 (2006).

[83] Miller, N., Ager III, J. W., Jones, R. E., Smith III, H. M., Mayer, M. A., Yu, K. M., Hawkridge, M. E., Liliental-Weber, Z., Haller, E. E., Walukiewicz, W., Schaff, W. J., Gallinat, C., Koblmüller, G., and Speck, J. S. *Physica B* **404**, 4862–4865 (2009).

[84] Miller, N., Ager III, J. W., Jones, R. E., Smith III, H. M., Yu, K. M., Hawkridge, M. E., Haller, E. E., Walukiewicz, W., Schaff, W. J., Gallinat, C., Koblmüller, G., and Speck, J. S. *unpublished* .

[85] Yim, J. W. L., Jones, R. E., Yu, K. M., Ager III, J. W., Walukiewicz, W., Schaff, W. J., and Wu, J. *Phys. Rev. B* **76**(4), 41303 (2007).

[86] Wang, X., Che, S. B., Ishitani, Y., and Yoshikawa, A. *Appl. Phys. Lett.* **91**, 242111 (2007).

[87] Ager III, J. W., Miller, N., Jones, R. E., Yu, K. M., Wu, J., Schaff, W. J., and Walukiewicz, W. *Phys. Status Solidi B* **245**(5), 873 (2008).

[88] Ager III, J. W., Jones, R. E., Yamaguchi, D. M., Yu, K. M., Walukiewicz, W., Li, S. X., Haller, E. E., Lu, H., and Schaff, W. J. *Phys. Status Solidi B* **244**(6), 1820 (2007).

[89] Brown, G. F., Ager III, J. W., Walukiewicz, W., Schaff, W. J., and Wu, J. *Appl. Phys. Lett.* **93**, 262105 (2008).

[90] Meyer, J. R., Hoffman, C. A., Bartoli, F. J., Arnold, D. A., Sivananthan, S., and Fauri, J. P. *Semicond. Sci. Technol.* **8**, 805–823 (1993).

[91] National High Magnetic Field Laboratory. http://www.magnet.fsu.edu/.

[92] Matthews, K. D., Chen, X., Hao, D., Schaff, W. J., and Eastman, L. F. *Phys. Status Solidi C* **5**, 1863–1865 (2008).

[93] Seeger, K. *Semiconductor physics*. Springer New York, (2002).

[94] Wang, S. *Fundamentals of semiconductor theory and device physics*. Prentice Hall Englewood Cliffs, NJ, (1989).

[95] Johnson, V. A. and Lark-Horovitz, K. *Phys. Rev.* **92**, 226 (1953).

[96] Geballe, T. H. and Hull, G. W. *Physical Review* **98**(4), 940–947 (1955).

[97] Böer, K. W. *Survey of Semiconductor Physics*. Van Nostrand Reinhold New York, (1990).

[98] Lu, H., Schaff, W., Eastman, L. F., Wu, J., Walukiewicz, W., Look, D., and Molnar, R. J. *Mat. Res. Soc. Symp. Proc.* **743**, L4.10.1 (2003).

[99] Song, Y. W. Master's thesis, University of Canterbury. Physics and Astronomy, (2008).

[100] Nolas, G. S., Sharp, J., and Goldsmid, H. J. *Thermoelectrics: Basic Principles and New Materials Developments*. Springer, (2001).

[101] Kolodziejczak, J. and Zukotynski, S. *Phys. Status Solidi B* **5**(1) (1964).

[102] MacDonald, D. K. C. *Thermoelectricity: an introduction to the principles*. John Wiley and Sons, Inc., New York, (1962).

[103] Miller, N. Master's thesis, University of California - Berkeley, (2009).

[104] Baars, J., Brink, D., Edwall, D. D., and Bubulac, L. O. *J. Electron. Mater.* **22**(8), 923–929 (1993).

[105] Baars, J., Brink, D., and Ziegler, J. *Journal of Vacuum Science & Technology B: Microelectronics and Nanometer Structures* **9**, 1709 (1991).

[106] Wagener, M. C., Wagener, V., and Botha, J. R. *Appl. Phys. Lett.* **94**, 262106 (2009).

[107] Gopal, V., Chen, E. H., Kvam, E. P., and Woodall, J. M. *J. Electron. Mater.* **29**(11), 1333–1339 (2000).

[108] Piper, L. F. J., Veal, T. D., Lowe, M. J., and McConville, C. F. *Phys. Rev. B* **73**(19), 195321 (2006).

[109] Olsson, L., Andersson, C. B. M., Håkansson, M. C., Kanski, J., Ilver, L., and Karlsson, U. O. *Phys. Rev. Lett.* **76**(19), 3626–3629 (1996).

[110] Smit, K., Koenders, L., and Mönch, W. *Journal of Vacuum Science & Technology B: Microelectronics and Nanometer Structures* **7**, 888 (1989).

[111] Wu, J. personal communication, unpublished, April (2010).

[112] Lu, H., Schaff, W. J., Hwang, J., Wu, H., Yeo, W., Pharkya, A., and Eastman, L. F. *Appl. Phys. Lett.* **77**(16), 2548 (2000).

[113] Gallinat, C. S., Koblmüller, G., Brown, J. S., and Speck, J. S. *J. Appl. Phys.* **102**(6), 064907 (2007).

[114] Koblmüller, G., Gallinat, C. S., and Speck, J. S. *J. Appl. Phys.* **101**, 083516 (2007).

[115] Kaufmann, U., Schlotter, P., Obloh, H., Köhler, K., and Maier, M. *Phys. Rev. B* **62**(16), 10867 (2000).

[116] Romano, L. T., Kneissl, M., Northrup, J. E., Van de Walle, C. G., and Treat, D. W. *Appl. Phys. Lett.* **79**(17), 2734–2736 (2001).

[117] Vennéguès, P., Leroux, M., Dalmasso, S., Benaissa, M., De Mierry, P., Lorenzini, P., Damilano, B., Beaumont, B., Massies, J., and Gibart, P. *Phys. Rev. B* **68**(23), 235214 Dec (2003).

[118] Liliental-Weber, Z., Tomaszewicz, T., Zakharov, D., Jasinski, J., and O'Keefe, M. A. *Phys. Rev. Lett.* **93**, 206102 (2004).

[119] Liliental-Weber, Z. *Indium Nitride and Related Alloys*, chapter 14: Structure of InN and their alloys with Ga; Transmission Electron Microscopy Studies. CRC Press, Taylor and Francis Group, LLC (2009).

[120] Liliental-Weber, Z., Benamara, M., Swider, W., Washburn, J., Grzegory, I., Porowski, S., Lambert, D. J. H., Eiting, C. J., and Dupuis, R. D. *Appl. Phys. Lett.* **75**(26), 4159–4161 (1999).

[121] Wang, X., Che, S.-B., Ishitani, Y., Yoshikawa, A., Sasaki, H., Shinagawa, T., and Yoshida, S. *Appl. Phys. Lett.* **91**(8), 081912 (2007).

[122] Pezzagna, S., Venngus, P., Grandjean, N., and Massies, J. *J. Cryst. Growth* **269**(2-4), 249 – 256 (2004).

[123] Hsu, L., Jones, R. E., Li, S. X., Yu, K. M., and Walukiewicz, W. *J. Appl. Phys.* **102**, 073705 (2007).

[124] King, P. D. C., Veal, T. D., Gallinat, C. S., Koblmüller, G., Bailey, L. R., Speck, J. S., and McConville, C. F. *J. Appl. Phys.* **104**, 103703 (2008).

[125] Wang, X., Che, S. B., Ishitani, Y., and Yoshikawa, A. *Appl. Phys. Lett.* **90**, 201913 (2007).

[126] Khan, N., Nepal, N., Sedhain, A., Lin, J. Y., and Jiang, H. X. *Appl. Phys. Lett.* **91**, 012101 (2007).

[127] Arnaudov, B., Paskova, T., Paskov, P. P., Magnusson, B., Valcheva, E., Monemar, B., Lu, H., Schaff, W. J., Amano, H., and Akasaki, I. *Phys. Rev. B* **69**(11), 115216 (2004).

[128] Klochikhin, A. A., Davydov, V. Y., Emtsev, V. V., Sakharov, A. V., Kapitonov, V. A., Andreev, B. A., Lu, H., and Schaff, W. J. *Phys. Rev. B* **71**(19), 195207 (2005).

[129] Jones, R. E., van Genuchten, H. C. M., Li, S. X., Hsu, L., Yu, K. M., Walukiewicz, W., Ager III, J. W., Haller, E. E., Lu, H., and Schaff, W. J. *Mater. Res. Soc. Symp. Proc.* **892**, 105 (2006).

[130] Petritz, R. L. *Phys. Rev.* **110**, 1254 (1958).

[131] Look, D. C. and Molnar, R. J. *Appl. Phys. Lett.* **70**(25), 3377–3379 (1997).

[132] Look, D. *Electrical characterization of GaAs materials and devices.* Wiley New York, (1989).

[133] Gibart, P. *Rep. Prog. Phys.* **67**, 667–715 (2004).

[134] Lu, C. J., Bendersky, L. A., Lu, H., and Schaff, W. J. *Appl. Phys. Lett.* **83**(14), 2817–2819 (2003).

[135] Liliental-Weber, Z., Jones, R. E., van Genuchten, H. C. M., Yu, K. M., Walukiewicz, W., Ager III, J. W., Haller, E. E., Lu, H., and Schaff, W. J. *Physica B: Physics of Condensed Matter* **401**, 646–649 (2007).

[136] Look, D. C. and Sizelove, J. R. *Phys. Rev. Lett.* **82**(6), 1237–1240 (1999).

[137] Krtschil, A., Dadgar, A., and Krost, A. *Appl. Phys. Lett.* **82**(14), 2263–2265 (2003).

[138] Cherns, D., Jiao, C. G., Mokhtari, H., Cai, J., and Ponce, F. A. *Phys. Status Solidi B* **234**(3) (2002).

[139] Cai, J. and Ponce, F. A. *Phys. Status Solidi A* **192**(2) (2002).

[140] Akagi, T., Kosaka, K., Harui, S., Muto, D., Naoi, H., Araki, T., and Nanishi, Y. *J. Electron. Mater.* **37**(5), 603–606 (2008).

[141] Hansen, P. J., Strausser, Y. E., Erickson, A. N., Tarsa, E. J., Kozodoy, P., Brazel, E. G., Ibbetson, J. P., Mishra, U., Narayanamurti, V., DenBaars, S. P., and Speck, J. S. *Appl. Phys. Lett.* **72**, 2247 (1998).

[142] Muto, D., Naoi, H., Araki, T., Kitagawa, S., Kurouchi, M., Na, H., and Nanishi, Y. *Phys. Status Solidi A* **203**(7) (2006).

[143] Brandt, M. S., Herbst, P., Angerer, H., Ambacher, O., and Stutzmann, M. *Phys. Rev. B* **58**(12), 7786–7791 (1998).

[144] Polyakov, V. M. and Schwierz, F. *Appl. Phys. Lett.* **88**, 032101 (2006).

[145] Rode, D. L. *Semiconductors and Semimetals Vol. 10, Ch. 1: "LowField Electron Transport".* Academic Press, New York (1975).

[146] Müller, E., Gerthsen, D., Brückner, P., Scholz, F., Gruber, T., and Waag, A. *Phys. Rev. B* **73**(24), 245316 (2006).

[147] Bonch-Bruevich, V. L. and Glasko, V. B. *Fiz. Tverd. Tela* **3**, 36 (1966).

[148] Conwell, E. M. and Weisskopf, V. F. *Phys. Rev.* **77**, 388 (1950).

[149] Brooks, H. *Advan. Electron. Electron Phys.* **7**, 85 (1955).

[150] Falicov, L. M. and Cuevas, M. *Phys. Rev.* **164**, 1025 (1967).

[151] Dingle, R. B. *Phil. Mag.* **46**, 831 (1955).

[152] Moram, M. A. and Vickers, M. E. *Rep. Prog. Phys.* **72**(3), 036502 (2009).

[153] Blood, P. *Semicond. Sci. Technol.* **1**, 7 (1986).

[154] Lu, Y., Ho, C., Yeh, J., Lin, H., and Gwo, S. *Appl. Phys. Lett.* **92**, 212102 (2008).

[155] Lu, Y., Chang, Y., Hong, Y., Lee, H., Gwo, S., and Yeh, J. *Appl. Phys. Lett.* **95**, 102104 (2009).

[156] Lee, H. H., Racicot, R. J., and Lee, S. H. *Appl. Phys. Lett.* **54**(8), 724–726 (1989).

[157] Naoi, H., Muto, D., Hioka, T., Hayakawa, Y., Suzuki, A., Araki, T., and Nanishi, Y. *Physica Status Solidi B* **244**(6), 1834 (2007).

[158] Bailey, L. R., Veal, T. D., Kendrick, C. E., Durbin, S. M., and McConville, C. F. *Appl. Phys. Lett.* **95**(19), 192111 (2009).

[159] Lu, H., Schaff, W. J., and Eastman, L. F. *J. Appl. Phys.* **96**(6), 3577–3579 (2004).

[160] Jones, R. E. Master's thesis, University of California - Berkeley, (2002).

[161] Cimalla, V., Lebedev, V., Wang, C. Y., Ali, M., Ecke, G., Polyakov, V. M., Schwierz, F., Ambacher, O., Lu, H., and Schaff, W. J. *Appl. Phys. Lett.* **90**(15), 152106 (2007).

[162] Denisenko, A., Pietzka, C., Chuvilin, A., Kaiser, U., Lu, H., Schaff, W. J., and Kohn, E. *J. Appl. Phys.* **105**(3), 033702 (2009).

[163] Fraser, D. A. *The physics of semiconductor devices.* Clarendon Press, Oxford, (1986).

[164] Seebeck, T. J. *Abh. K. Akad. Wiss. Berlin* , 289 (1821).

[165] Seebeck, T. J. *Abh. K. Akad. Wiss. Berlin* , 265 (1823).

[166] Peltier, J. *Ann. Chim. Phys* **56**, 371–386 (1834).

[167] Bell, L. E. *Science* **321**(5895), 1457 (2008).

[168] Chen, G., Dresselhaus, M. S., Dresselhaus, G., Fleurial, J. P., and Caillat, T. *Int. Mater. Rev.* **48**(1), 45–66 (2003).

[169] Snyder, G. J. and Toberer, E. S. *Nat. Mater.* **7**(2), 105–114 (2008).

[170] Brazier, K. http://en.wikipedia.org/wiki/Peltier Open source images under official license http://creativecommons.org/licenses/by-sa/3.0/.

[171] National Instruments. LabVIEW is a product of National Instruments, available at http://www.ni.com/labview/.

# Appendix A

# Broader thermoelectric background and theory

## A.1 Thermoelectric Effects and Devices

There are actually three so-called "thermoelectric effects," and there is often some confusion about what these effects are and how they are related. The clearest discussions of these basic issues are found in MacDonald [102] and Fraser [163]. The three thermodynamically reversible thermoelectric effects are the Seebeck effect, the Peltier effect, and the Thompson effect, which will be described below. The Joule heating due to resistive losses within a conductor is not considered a thermoelectric effect, as discussed in comparison to the Peltier heat below. The Seebeck effect is the primary concern in this work, which is alternatively called the "thermopower." This is somewhat of a misnomer in that the measured quantity, the Seebeck coefficient $S = \Delta V/\Delta T$, is the voltage $\Delta V$ that develops across a conductor in which a temperature difference $\Delta T$ is applied, and thus refers to a voltage per unit temperature, which is not a unit of power. Nonetheless, this term will be used herein as it is in common use in the literature.

Thomas Johann Seebeck is given credit for the discovery of the Seebeck effect in the early 1820s [164, 165]. He was searching experimentally for a connection between electricity and heat and discovered, by accident, that if he made a circuit out of wires of two different metals (copper and bismuth) making two junctions and heated one junction preferentially, this caused a magnetized needle in the vicinity to be deflected. He thought that the difference in temperature across the wires magnetized the wires and published two papers in 1821 and 1823 respectively titled "About the magnetism of the galvanic chain" and "Magnetic polarization of metals and ores by temperature difference" (title translations courtesy L. Reichertz) [164, 165].[a] Others argued what we now know to be true, that the difference in temperature caused a current to flow in the circuit (now called a "Peltier current"), which produced a magnetic field.[b]

If a circuit is constructed as in Fig. A.1a where the two wires 1 and 2 are the same conducting material, the thermoelectric potential caused by the temperature gradient across each will exactly cancel due to symmetry such that no current will flow. Or equivalently, the voltage of an open circuit as in Fig. A.1b will be zero. For this reason, couples of two different materials are used

[a] He went on to postulate that the earth's magnetic field was caused by the difference in temperature between the poles and the equator.

[b] And of course, the earth's magnetic field results from convection in the outer core, e.g. see geodynamo theory.

such that the thermoelectric current (closed circuit) or potential (open circuit) is not zero. Then in this case the measured quantity (current or potential) depends on the difference in the Seebeck coefficient of the two materials. The necessity to have two different materials for easy observation of the Seebeck effect often causes the erroneous notion that it is somehow a junction effect. In fact it is not; a voltage will develop across a single piece of material in the presence of a temperature gradient as long as the Seebeck coefficient of that material is nonzero. The junction is used in a practical sense in order to make the thermoelectric potential readily observable but is not required by the phenomenon.

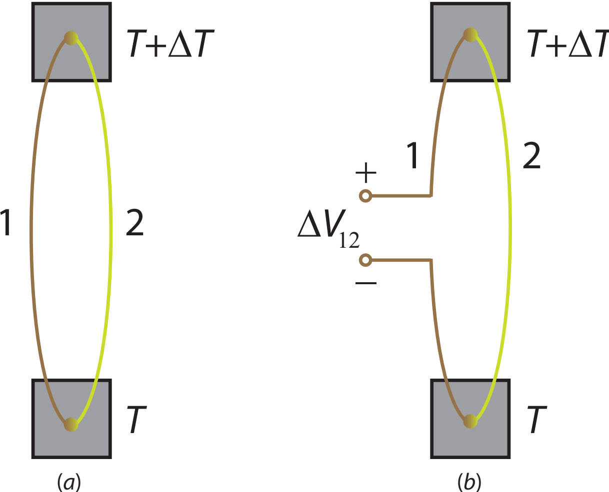


**Figure A.1** Schematic diagram of two basic thermoelectric circuits where junctions between wires 1 and 2 are attached to thermal reservoirs with fixed temperatures $T$ and $T + \Delta T$. a) closed circuit in which a current will flow if the wires 1 and 2 are made of different conducting materials, and b) open circuit in which there will be a thermoelectric potential $\Delta V_{12} \sim \Delta T$ if the wires 1 and 2 are made of different conducting materials and $\Delta T << T$. For the polarity shown, assuming $S_1$ and $S_2$ are both negative and $\Delta T > 0$, $|S_1| > |S_2|$.

The Seebeck coefficient of materials is preferably determined by measuring the thermoelectric potential in an open circuit configuration, such as that shown in Fig. A.1b. In the closed circuit condition of Fig. A.1a, the current flowing in the circuit does depend on the thermopower of the materials and the temperature difference $\Delta T$, but it would also depend on the resistance (and hence on the dimensions) of the conductors in the circuit. In an open circuit there is no current flow, and the thermoelectric potential does not depend on the shape or dimensions of the conductors in the circuit. The actual circuit used in this work is discussed in Appendix B and illustrated in Fig. B.1.

Directly measuring the thermopower of a single material is somewhat difficult but can be done. If one of the two materials is superconducting, then no voltage will drop across it, and the observed thermoelectric potential is that of the other conductor only. This is a very straightforward technique, but it is limited to the low temperature regime where superconducting materials exist. Another method is to make a couple out of one material of unknown thermopower and one material of *known* thermopower. If the thermopower of one of the "legs" is known then it is trivial to determine the thermopower of the other material. It is possible to establish known values of the thermopower up to even high temperatures through careful measurements of the Thomson heat (discussed below), which has been done for lead and platinum. This is how the absolute

thermopower of metals is measured. For semiconductors it is somewhat easier; since the absolute value of the thermopower of semiconductors is generally 10 to 1000 times larger than that of metals, the thermocouple voltage $\Delta V_{12}$ where one leg is a semiconductor and the other a metal is dominated by the semiconductor. This fact, in conjunction with the data collection method described in Appendix B, makes it relatively easy to perform accurate measurements of the absolute thermopower of semiconductors.

Around the same time, Jean Charles Athanase Peltier discovered that when an electric current passes from one substance to another, heat may be absorbed or evolved in the junction region depending on the direction of current flow [166]. This heat has to do with the change in the Fermi level at the junction, is thermodynamically reversible, and is clearly distinguishable from Joule heating. The Peltier heat is linear in both magnitude and sign (heating or cooling) with the current flow ($Q_{Peltier} \propto I$), whereas Joule heat is irreversible, depends on the resistance of the conductor, is always positive (heating), and depends on the square of the current ($Q_{Joule} \propto I^2$). The heat per unit time evolved or absorbed at a junction due to the Peltier effect is given by $\dot{Q} = \Pi_{12} I$ where $\Pi_{12} = \Pi_1 - \Pi_2$ is the Peltier coefficient of the junction between materials 1 and 2. The Peltier coefficient of a conductor can also be defined in terms of the Seebeck coefficient as follows

$$\Pi = TS \tag{A.1}$$

which is one of the *Onsager relations* and is known as the *second Kelvin relation* after Lord Kelvin (William Thomson) [93, 102]. Thus, by measuring the Seebeck coefficient, the Peltier coefficient of a material is also determined. The units of the Peltier coefficient are typically given in $\mu$V.

Fig. A.2 shows the Peltier effect schematically. Note that if the junction is not abrupt, the Peltier heat is absorbed or evolved over the junction volume as shown. Although the Peltier effect occurs at junctions, it is not a "contact effect." Neither the magnitude nor sign of the Peltier heat is affected by the nature of the contact; it is a function only of the bulk properties of the two materials brought together in the junction. The Peltier heat of a single material can be evaluated if put in a junction with a superconductor, which would contribute nothing to the Peltier heat.

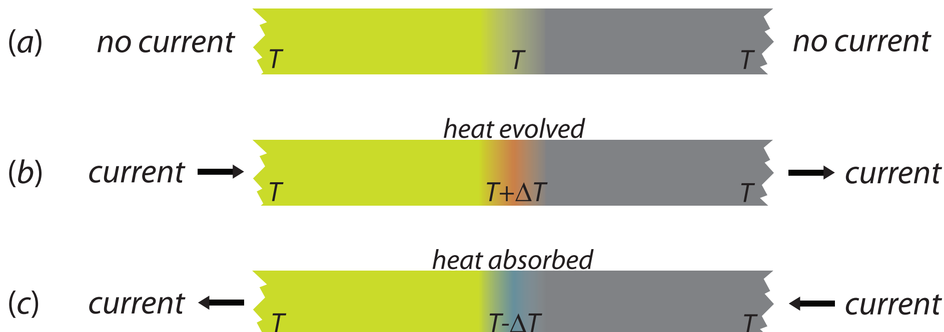


**Figure A.2** Schematic diagram of the Peltier effect in the junction of two different conductors. a) with no current flow there is no heat evolved or absorbed and the couple is isothermal, b) with current flow left-to-right heat is evolved at the junction proportional to the magnitude of the current and Peltier heating occurs in the region of the junction, and c) with current flow in the opposite direction through the same junction heat is absorbed at the junction proportional to the magnitude of the current and Peltier cooling occurs in the region of the junction.

The Peltier effect is utilized in solid-state thermoelectric heaters/refrigerators (since there are always two junctions symmetry dictates that heat will be evolved at one junction and absorbed at the other) as well as thermoelectric power generators. Schematics of these devices are shown in Fig. A.3. Running current through a set of junctions can be used either as a heater or refrigerator. An existing temperature difference across the device can be used to generate a current as a solid state generator. Both devices have found niche markets, but widespread adoption awaits further development of thermoelectric materials. The dimensionless figure of merit used to describe thermoelectric materials is $zT = \frac{S^2\sigma}{\kappa}$ where $\sigma$ and $\kappa$ are the electrical and thermal conductivities respectively. Maximization of this figure of merit in a given material will to first order maximize the efficiency of thermoelectric devices constructed of that material (see reference [167] for discussion of thermoelectric system-level optimization). This is a difficult problem since $S$ and $\sigma$ are usually anti correlated by their opposite dependencies on carrier concentration and $\sigma$ and $\kappa$ are usually correlated since electrical carriers contribute to both electrical and thermal transport. Also, improvement of crystalline quality generally improves both electrical and thermal transport since charge carriers and phonons are both scattered by defects. However, tremendous effort is being put into this problem and significant gains have been made in recent years with increasingly complex bulk materials as well as nanostructures [100, 168, 169].

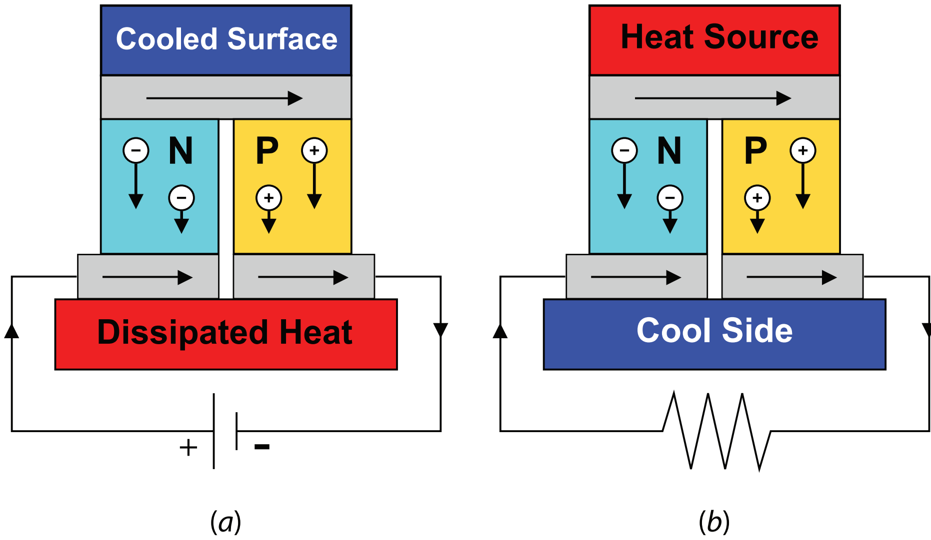


**Figure A.3** Schematic diagrams of thermoelectric devices based on the Peltier effect. a) Thermoelectric refrigerator in which current is pushed through p-type and n-type semiconductors such that heat is absorbed at the top and ejected to a reservoir (heat sink) at the bottom, and b) Thermoelectric generator in which the temperature difference between the top junctions and bottom junctions drives a current through the load. Figure after reference [170].

In 1854 William Thomson (later Lord Kelvin) analyzed the situation with the Seebeck and Peltier effects and concluded that there must be a third thermoelectric effect not yet accounted for, which led him to postulate the existence of the Thomson heat, which was later confirmed. The Thomson effect describes heat evolved or absorbed when an electric current is passed through a conductor in the presence of a temperature gradient. Given the same temperature gradient, the sign of the Thomson heat (evolved or absorbed) can be switched simply by changing the direction of current flow. The heat evolved or absorbed per unit volume and time in a conductor is given by

the following equation:

$$\dot{Q} = \frac{J_x^2}{\sigma} - \mu_{Th} J_x \frac{dT}{dx} \tag{A.2}$$

where $J_x$ is the current density, $\sigma$ is the electrical conductivity, and $\mu_{Th}$ is the Thomson coefficient. The first term of Eq. A.2 is the familiar and irreversible Joule heating; note that it is proportional to the square of the current and is independent of the temperature gradient. The second term is the Thomson heat, linearly proportional to the current and temperature gradient, and whose sign depends on the directions of these two terms relative to one another.

In other words, if charge carriers are traveling from low to high temperature, they absorb heat and Thomson cooling is observed. The analogy given by Thomson was that "we may call [the Thomson heats] the specific heats of electricity in the different metals, since they express the quantities of heat absorbed or evolved by the unit of current electricity in passing from cold to hot, or from hot to cold, between localities differing by a degree of temperature in each metal respectively [102]." It turns out to first approximation that this is so, and in materials with poor electron-phonon coupling this basic analysis holds that the Thomson heats are close to what is expected of the specific heat of the charge carriers. However, in materials where electron-phonon coupling is stronger, the "phonon-drag" effect becomes important; the electron reservoir is then connected to the lattice (and the lattice specific heat) by electron phonon scattering events. In this case a much more detailed analysis of transport is required to understand the Thomson heat.

The first Thomson relation gives the relationship between the Thomson coefficient and the Seebeck coefficient as follows

$$\mu_{Th} = T \frac{dS}{dT} \tag{A.3}$$

which allows the determination of the Seebeck coefficient from calorimetric measurements of the Thomson heat using the following relation

$$S(T) = \int_0^T \frac{\mu_{Th}}{T} dT \tag{A.4}$$

This is the method employed to construct an absolute thermoelectric scale for lead and platinum as mentioned earlier in this section. The set of relations given as Eqs. A.3 and A.1 are known as the Thomson or Kelvin relations, which provide the relationships between the Seebeck, Peltier, and Thomson coefficients. These relations show us that complete knowledge of all the thermoelectric properties of a material can be derived by measuring the Seebeck coefficient alone, which is readily achieved with great accuracy.

## A.2 Origins of the Seebeck Effect

The Seebeck effect is perhaps the best known of the three thermoelectric effects since it is easily measured and is the basis of thermocouple devices, which are widely used in research labs and industrial settings. The Seebeck effect of semiconductors is of the most interest here and the derivation of the nondegenerate approximation gives great insight into the origins of the thermoelectric potential that develops when a temperature gradient exists within a semiconductor. There are two phenomena that contribute to the thermoelectric potential: 1) the Fermi level is temperature dependent, and 2) the open circuit condition leads to an internal electric field due to the drift-diffusion balance. These two effects are shown schematically in Fig. A.4; the hot carriers

diffuse farther creating a net current of the majority carrier from hot to cold (diffusion), which is balanced by the formation of an internal electric field creating a current from cold to hot (drift) such that the net current is zero, and the Fermi level lies deeper in the gap at the hot side than the cold (exaggerated here for clarity).

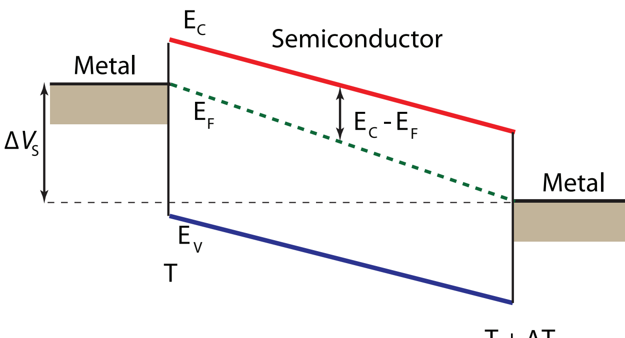


**Figure A.4** Schematic band diagram showing an n-type semiconductor with two metal contacts and a temperature gradient (cold on left, hot on right). The potential measured between the two metal contacts is the thermoelectric potential of the Seebeck effect with contributions both from the internal electric field and the temperature dependence of the Fermi level.

This derivation follows the method of Wang and assumes a parabolic band [94]. The first contribution comes from the temperature dependence of the Fermi level. Starting with the well known equation for calculating the electron concentration $n$ of a nondegenerate semiconductor from the effective density of states $N_C$, the bandgap $E_g$, and the Fermi level position $E_F$

$$n = N_C \exp\left(-\frac{E_C - E_F}{k_B T}\right) \tag{A.5}$$

where $E_g$ has been replaced by $E_C$ already since both are referenced to the top of the valence band. We can rearrange terms such that we have

$$E_C - E_F = k_B T \left(\ln N_C - \ln n\right) \tag{A.6}$$

Differentiating Eq. A.6 with respect to $T$ and assuming the gradient is constant we obtain

$$\frac{d(E_C - E_F)}{dT} = \frac{E_C - E_F}{T} + \frac{3k_B}{2} - k_B T \frac{d(\ln n)}{dT} = \frac{\Delta(E_C - E_F)}{\Delta T} \tag{A.7}$$

The second contribution comes from the internal electric field that develops in response to the drift diffusion balance. The electric current density can be written with drift and diffusion terms as follows

$$J = n\mu_e e E + e\frac{d}{dx}(D_e n) \tag{A.8}$$

where $x$ is the axis of the temperature gradient, $\mu_e$ is the electron mobility, $E$ is the electric field, and $D_e$ is the diffusivity of electrons. Since the Seebeck effect occurs under open circuit conditions the current density $J$ is zero and we can rearrange Eq. A.8 to read

$$E = \frac{-1}{\mu_e n}\frac{d}{dx}(D_e n) = \frac{-k_B T}{e}\left[\frac{d(\ln n)}{dx} + \frac{d(\ln D_e)}{dx}\right] \tag{A.9}$$

Using $\mu = e\tau/m^*$, $\varepsilon = Bk_\mathrm{B}T$ since the average kinetic energy of electrons is proportional to $k_\mathrm{B}T$, and again assuming within the relaxation time approximation that $\tau = A\varepsilon^r$ we can rewrite the diffusivity

$$D_e = \frac{k_\mathrm{B}T}{e}\mu_e = \frac{k_\mathrm{B}T}{m^*}A\varepsilon^r = \frac{AB^r}{m^*}(k_\mathrm{B}T)^{r+1} \tag{A.10}$$

Substituting Eq. A.10 into Eq. A.9 yields a more useful version of the electric field equation

$$E = \frac{-k_\mathrm{B}T}{e}\left[\frac{d(\ln n)}{dx} + \frac{r+1}{T}\frac{dT}{dx}\right] \tag{A.11}$$

Now one can add the two contributions to the electric field together to get the thermoelectric potential

$$\Delta V_S = -E\Delta x + \frac{1}{e}\left[\Delta(E_C - E_F)\right] \tag{A.12}$$

Substituting Eqs. A.7 and A.11 into Eq. A.12 and assuming the temperature gradient is constant such that $\Delta x = \frac{dx}{dT}\Delta T$ one can rewrite the potential and generate an equation for the thermopower as

$$S_\mathrm{nondegen} = \frac{\Delta V_S}{\Delta T} = \frac{-k_\mathrm{B}}{e}\left(r + \frac{5}{2} + \frac{E_C - E_F}{k_\mathrm{B}T}\right) \tag{A.13}$$

which is the same as Eq. 1.3 presented in the introduction. Again, an analogous equation for holes is obtained by replacing the $E_C - E_F$ term with $E_F - E_V$ and removing the negative sign in front of the equation. This derivation shows in a straightforward way the origins of the thermopower of a semiconductor and the meaning of the terms of the equation.

A similar analysis for metals yields the following approximation

$$S_\mathrm{degen} = (r + 3/2)\frac{-k_\mathrm{B}}{e}\frac{\pi^2}{3}\frac{k_\mathrm{B}T}{E_F} \tag{A.14}$$

which also holds for degenerate semiconductors by replacing $E_F$ by $E_F - E_C$ for n-type materials and $E_F - E_V$ for p-type materials. In the case of ambipolar conduction, the following relation gives the apparent thermopower

$$S_\mathrm{ambipolar} = \frac{S_h\mu_h p + S_e\mu_e n}{\mu_h p + \mu_e n} \tag{A.15}$$

where $S_e$ and $S_h$ are the electron and hole Seebeck coefficients assuming only one carrier type as in Eq. A.13 or the more general form discussed below [94]. The contributions of electrons and holes to the total thermoelectric response are weighted by their mobility-concentration product (or conductivity).

# Appendix B

# Thermopower equipment and measurement details

## B.1 Variable temperature apparatus: setup and instrumentation

Thermopower measurements were performed by measuring the voltage that develops across a sample when a temperature gradient is applied. To apply the temperature gradient, samples were suspended between two temperature controlled copper blocks as shown schematically in Fig. B.1 and photographically in Fig. B.2. The design of the sample stage assembly is based on the stage used by Brandt *et al.* to measure the thermopower of n- and p-type GaN [143]. The sample stage assembly was designed and custom machined specifically for this experiment while the rest of the system was assembled from preexisting or commercially available equipment and materials. The sample stage assembly is cooled by contact to a cold finger filled with liquid nitrogen. The sample stage and cold finger are enclosed inside a small vacuum chamber connected to a small turbo pump and backed by a mechanical roughing pump providing pressures as low as $9 \times 10^{-7}$ torr. The vacuum environment provides excellent thermal insulation and prevents substances in the air (such as water vapor) from condensing on the sample and wiring inside when conducting measurements at low temperatures.

In this configuration the sample temperature can be reduced to $\sim$130 K, significantly above the boiling point of nitrogen, 77 K, due to the lack of a radiative heat shield and other unwanted thermal coupling. Higher temperatures are produced by passing current through resistive heaters in each sample block. The temperature at each end of the sample is monitored by affixing type-T thermocouples to either end using small pieces of In foil to ensure good thermal contact to the sample. To minimize transmission of heat to or from the sample the thermocouples are fabricated from very fine wire, only 0.005 inches in diameter. Commercial temperature controllers using Proportional/Integral/Derivative (PID) algorithms are employed for precise, automated control of temperature, which supply the current to the resistive heaters and use the thermocouple inputs as control sensors. Platinum RTD (resistive temperature device) sensors are also attached to the bottom of each sample block and read by the temperature controllers as secondary inputs. The RTD sensors are used in conjunction with control logic to prevent the sample blocks from overheating in the event that a thermocouple becomes detached or otherwise thermally decoupled from the system.

The thermocouple wires are used to measure the voltage of the sample as well by attaching

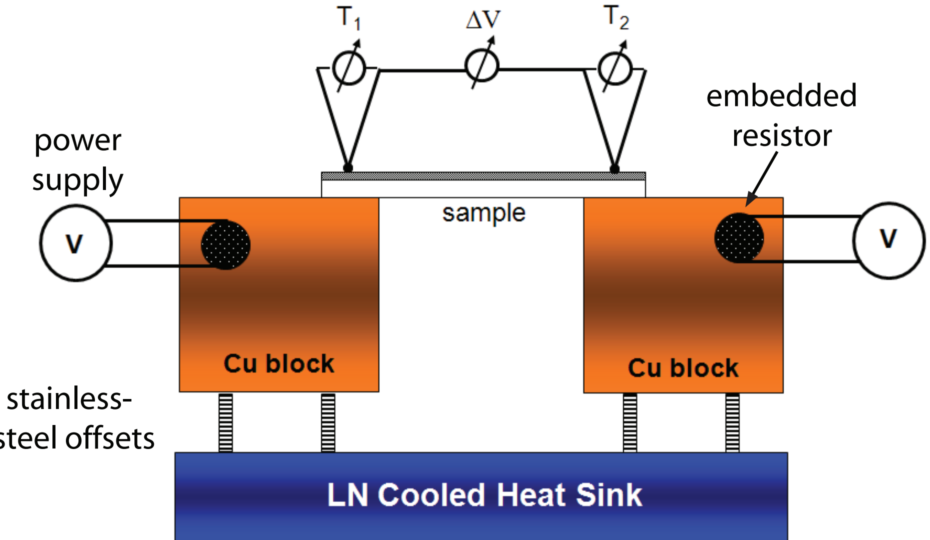


**Figure B.1** Schematic of sample stage assembly. There are three voltages measured, denoted by circles with arrows through them in the circuit diagram; the voltage of each thermocouple is measured to determine the two temperatures and $\Delta T$ and the voltage between the similar metals of the two thermocouples is measured to determine the voltage across the sample $\Delta V$.

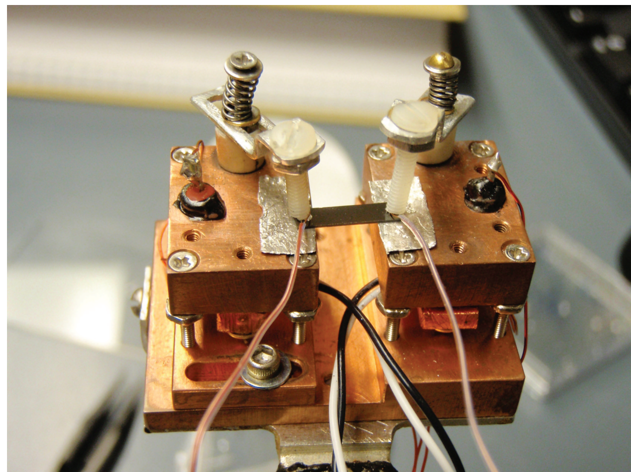

**Figure B.2** Top-view photograph of the actual sample stage assembly showing sample suspended at center with temperature probes held under spring loaded sample clips. The tops of the resistors embedded in the copper blocks are also visible as are the stainless steel offset screws. The two sets of thicker black and white wires extending from the bottom of each sample block are coming from the backup RTD sensors.

the leads of a high impedance digital multimeter (DMM) to the copper wire coming from each thermocouple as shown schematically in Fig. B.1. One major advantage of doing this is that the temperature and voltage are measured at exactly the same point on the sample. If the temperature and voltage are not measured at exactly the same point any inhomogeneities in the sample or applied temperature gradient could contribute to the error of the measurement. Because pressed In makes very good Ohmic electrical contacts to InN this process serves as both electrical and thermal contact to the sample. For samples where other electrical contact methods are used (e.g. Au-alloyed contacts on Si), In foil is still used on top for thermal contact. The best way to do this for thermal contact and mechanical stability is to press a small piece of In to the sample, then press the thermocouple tip into it, then press another piece of In foil on top making a sandwich. In this way the thermocouple head is entirely surrounded by metal, which is in good physical and thermal contact to the sample.

## B.2 Variable temperature rig: thermopower data collection

Both the digital multimeter and temperature controllers are connected to a computer running a LabVIEW program developed for this experiment [171]. The temperature data from the thermocouples and RTD sensors (along with other various parameters relating to temperature control) and the voltage data from the DMM are all fed into the computer. The LabVIEW program collects data from the instrumentation and sends commands to the temperature controllers (such as temperature set points and heater power level) based on the settings and logic of the program.

The Seebeck coefficient $S$ is given by the ratio $\Delta V/\Delta T$, where the deltas on voltage $V$ and temperature $T$ signify the difference between the values at the two ends of the sample. For better accuracy and to minimize offset effects from the metal contacts and leads, $S$ was found from the slope of a line fit to $\Delta V$ vs. $\Delta T$ for a series of measurements near a reference temperature, as shown in Fig. B.3 for an InN:Mg film. During the measurement, the temperatures of the two ends of the sample ($T_1$ and $T_2$) are equally spaced from the reference temperature to keep the average temperature of the sample constant at $T_{Ref}$. The variation of $T_1$ and $T_2$ with time during a measurement is shown schematically in the inset of Fig. B.3. Maximum values of $\Delta T$ of ∼10 K were typically used to maintain large voltage signals while minimizing error due to the temperature dependence of $S$. The excellent linearity of the $\Delta V$ vs. $\Delta T$ data verifies that $\Delta T$ was chosen to be sufficiently small. This procedure was repeated over a range of reference temperatures to determine the thermopower of n- and p-type InN from 150 to 300 K ($S$ vs. $T_{Ref}$).

The minimum achievable temperature at which thermopower data can be collected for this experimental setup is limited by heat transport through the sample from one block to the other (especially in the case of sample substrates made of Si or sapphire, which have very high thermal conductivity). Because thermal conductivity increases with decreasing temperature the transport of heat through the sample gets larger and larger until the desired temperature gradient can no longer be achieved, which sets the minimum temperature of the experiment. The instrumentation is sufficiently sensitive that a $\Delta T$ as small as 1 K is feasible and for smaller samples values of $\Delta T$ of 1 to 1.5 K were sometimes used in order to lower the minimum temperature. Another way to lower the minimum temperature limit is to ensure good thermal contact between the sample and blocks by using In foil or thermally conductive vacuum grease, which improves the physical contact at the interface. Increasing the aspect ratio or decreasing the thickness also reduces heat transport through the sample. The typical minimum achievable temperature for 5 mm × 10 mm samples with sapphire substrates using In foil at the sample/block interface is ∼180 K, however a lower

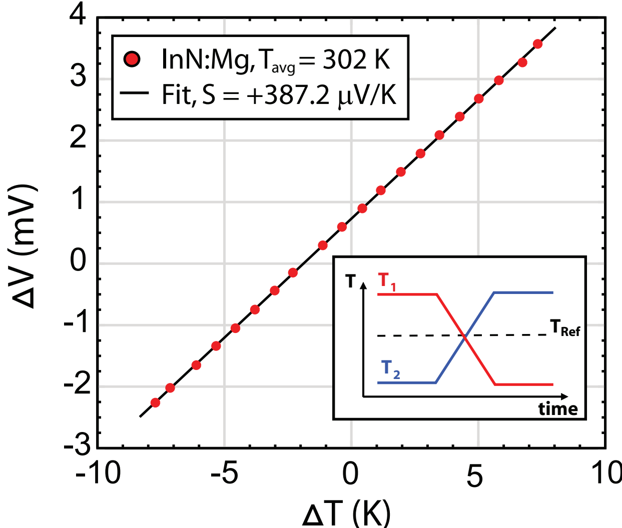


**Figure B.3** Measured $\Delta V$ vs. $\Delta T$ at 302 K for one InN:Mg film showing a positive slope indicative of p-type material. The linear fit yields a Seebeck coefficient of +387.2 $\mu V/K$. The inset is a schematic of the temperatures of the ends of the sample vs. time during the experiment.

limit as low as 130 K was achieved for one sample. In order to decrease the functional temperature of the experiment further the sample stage assembly would have to be redesigned with this goal in mind.

During a single experiment at a given $T_{Ref}$, the decrease in temperature of $T_1$ and increase in temperature of $T_2$ is accomplished through a series of steps. In order to improve the accuracy of the data set, statistically large sampling sizes were used wherever practical by making the step size small. Using a large number of steps (typically 20-40) results in more data points used in the slope fitting as shown in Fig. B.3. In fact, for clarity of this figure only every other data point is shown. With the goal of increasing the statistical significance of the $S$ vs. $T$ data set either a small step in $T_{Ref}$ such as 1 to 3 K between each data point was used, or the measurement was repeated at each $T_{Ref}$ 3 or 4 times and a larger step such as 10 to 20 K was used. Furthermore, the potential for errors due to asymmetry in the sample stage assembly was reduced by alternating from one data point to the next which side of the sample was hotter at the beginning of the experiment ($T_1$ or $T_2$).

For more information on the thermopower instrumentation and setup see Ref. [103].

## B.3 Room temperature apparatus

A second thermopower measurement system was used in collecting some of the room temperature data. This system was designed and built by a summer high school student, Charles Cao, under the supervision of Holland Smith, Joel Ager, and myself. The motivation was to build a system that was easy and fast to use, compared to the variable temperature (VT) system. This system is based on many of the same principles developed for the VT rig, but removes unnecessary complexity where possible. No vacuum system or liquid nitrogen cooling are used in the room temperature (RT) system, allowing a room temperature measurement to be taken in under 5 minutes time, whereas the VT system will take 6-12 hours to measure $S$ from 200-300 K and is impractical

for single room temperature measurements.

Fig. B.4 shows several photographs of the stage area of the RT system. Note that this stage area sits on a table-top rather than in a vacuum chamber. Voltage is measured through a programmable DMM similar to the VT system, but temperature is measured through an National Instruments (NI) card directly into the computer rather than through temperature controllers. In fact, no temperature controllers are used at all. The LabVIEW VI controls a programmable DC power supply, which supplies current to the resistive heaters embedded in the Al stage blocks, but only one at a time. The current can be slowly ramped by hand on the VI, or simply set to the desired endpoint value; the temperature and voltage data are recorded in real time off of the type-T thermocouple tips while the temperature is ramping, and no actual feedback temperature control or wait times are necessary. The current can also be manually switched to the other heater block if desired, but it is not necessary. Heat is conducted through the Al blocks into a large Al heat sink plate, which is sufficient to keep the blocks near room temperature. The average temperature does increase slightly over time, but only on the order of 1-3 °C, which is not a problem. Although less controlled than the VT rig's method, this is plenty accurate in most cases and produced Seebeck coefficient measurements within a few percent of the VT apparatus for several reference samples tested.

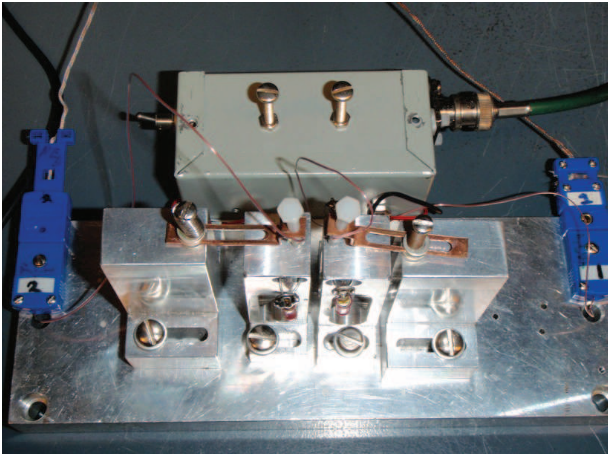

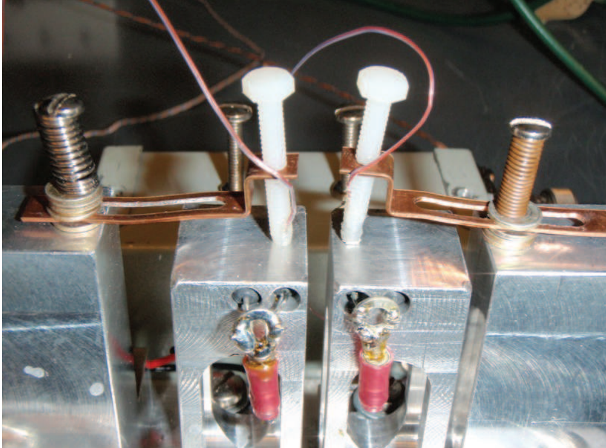

**Figure B.4** Photographs of the RT thermopower rig. The two sample stage blocks in the center are heated with embedded resistors. The thermocouples are embedded in the ends of the nylon screws used in the spring clips. The blue connectors at the sides link the small diameter type-T TC wires to the larger diameter type-T wires that lead to the NI box. The grey switch box at back links the BNC cable from the power supply into the local resistor wires, houses some fuses, and controls which block is heated by way of a toggle switch.

# Appendix C

# Interlayer experiment modeling

In section 3.2.2, the electron concentration and mobility of the interlayer were assumed to be constant over the thickness of the interlayer, but to depend on average on that thickness. In other words, the layer was assumed to be homogeneous, but a 10 nm thick layer was assumed to have higher electron concentration and lower mobility than a 100 nm thick layer. This is a first order attempt at including the variation of these properties with thickness within the layers. A more complicated approach could be used, in which the layers are not assumed to be homogeneous, but this would greatly increase the complexity of the model and, as explained in section 3.2.2, would not affect the values of the p-layer properties extracted from the analysis. These properties of interest are in great part insensitive to the treatment of the interlayer electrical properties. However, the Hall effect is very sensitive to the treatment of the interlayer properties, so to be self-consistent in modeling both the thermopower and Hall data, the first order approximation of the thickness variation of these properties was adopted.

Thus, functions describing the variation of carrier concentration and mobility on thickness $n(x)$ and $\mu(x)$ were assumed. Ideally these functions would be informed entirely from experimental measurements of thin n-type InN grown under the same conditions as the interlayer, but at the time limited data was available on such material. What was known at the time was that films grown to approximately 500 nm in thickness had a carrier concentration of $\sim 2 \times 10^{18}$ cm$^{-3}$ and mobility in the 1200-1300 cm$^2$/Vs range as shown in Table C.1. In fact, these films show a remarkable uniformity of carrier concentration and mobility; a reproducibility atypical of MBE growth, which speaks volumes about the Nanishi group's control of the growth process. This data demonstrates that the background electron concentration achieved with this method is $\sim 10^{18}$ cm$^{-3}$, as it doesn't change at all between the 500 nm films and the 750 nm film. The carrier concentration at the interface is assumed to be similar to the surface, reaching $10^{20}$ cm$^{-3}$. Based on these data points and influenced by the $n(x)$ data from Refs. [51, 82], the function $n(x) = 7.5 \times 10^{11} x^{0.90309}$ where $x$ is the interlayer thickness in nm was assumed for this analysis, which is also plotted in Fig. C.1a.

The dependence of mobility on thickness, $\mu(x)$, is estimated by assuming first a function for the variation of mobility with electron concentration, $\mu(n)$, then plugging in the assumed $n(x)$ function from above. The $\mu(n)$ dependence is well documented in the literature [123, 129]. The assumed function for the analysis was $\mu(n) = 1.23773 \times 10^{13} n^{-0.556303}$, where $n$ is in cm$^{-3}$, which yields the functional $\mu(x) = 1408.27 x^{0.502391}$ where $x$ is the interlayer thickness in nm. Both are plotted in Fig. C.1.

Fig. C.2 shows the data for the two interlayer series of samples, along with two versions of the fitting calculations. In one case (red dashed lines), the parameters of the interlayer are constrained

| Sample | $d$ (nm) | $S$ ($\mu$V/K) | $[n]$ (cm$^{-3}$) | $\mu$ (cm$^2$/Vs) |
|---|---|---|---|---|
| S596 | 750 | -174 | $1.7\times10^{18}$ | 1570 |
| S342 | 500 | -120 | $1.7\times10^{18}$ | 1260 |
| S333 | 500 | -118 | $1.8\times10^{18}$ | 1320 |
| S335 | 500 | -134 | $1.6\times10^{18}$ | 1340 |
| S326 | 500 | -117 | $1.9\times10^{18}$ | 1200 |
| S336 | 500 | -128 | $1.7\times10^{18}$ | 1270 |

**Table C.1**

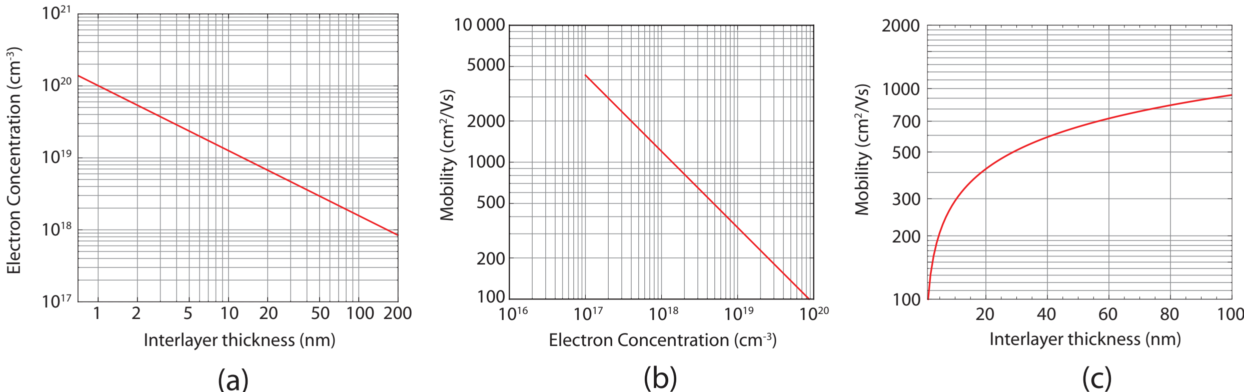


**Figure C.1** Assumed variation of average electron concentration and mobility with thickness of n-type interlayer. The intermediate $\mu(n)$ dependence is also plotted.

by the Hall effect data. In the other case (black dashed lines), the thermopower data is fit allowing the interlayer parameters to vary openly without constraint by the Hall data. Note that the modeled curves are very similar, both provide excellent agreement to the thermopower data, and both produce nearly the same parameters for the p-type layer, which are listed in Table C.2. However, the unconstrained models use interlayer electron concentrations over $10^{19}$ cm$^{-3}$ even though the known electron concentration of Nanishi n-InN is a factor of 5-10 lower. This descrepancy is cleared up in the constrained model, as shown in Fig. 3.7.

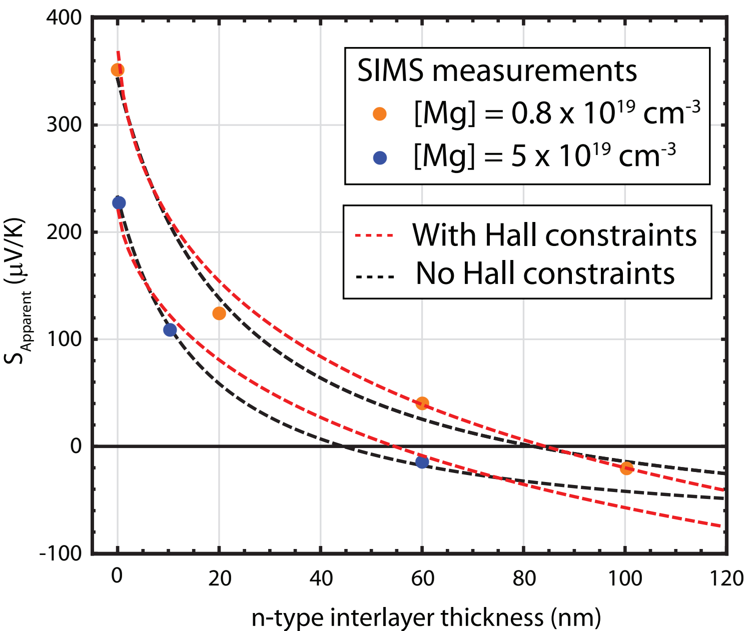


**Figure C.2** Interlayer series data and fits, part of the sensitivity analysis for the interlayer property assumptions.

| | $T_{\mathrm{Mg}} = 200$ °C series | | $T_{\mathrm{Mg}} = 225$ °C series | |
|---|---|---|---|---|
| | TP only | TP and Hall | TP only | TP and Hall |
| Free hole concentration, $p$ (cm$^{-3}$) | $1.4 \times 10^{19}$ | $0.9 \times 10^{19}$ | $4 \times 10^{19}$ | $4 \times 10^{19}$ |
| Hole mobility, $\mu_h$ (cm$^2$/Vs) | 10 | 14 | 2.6 | 3.5 |

**Table C.2** Summary of p-layer parameters (free hole concentration $p$ and mobility $\mu_h$) extracted from parallel conduction analysis in two different ways: one in which only the thermopower (TP) data is used to constrain the model allowing the interlayer properties to vary freely, and one in which the thermopower TP, Hall coefficient, and Hall mobility are all used to constrain the model, which serves to constrain the interlayer properties. This illustrates the insensitivity of the p-layer parameters to the assumptions made about the interlayer properties.

# Appendix D

# Electrolyte-based measurements

The electrolyte-based measurements are performed by taking advantage of the blocking nature of an electrolyte contact to InN. Fig. D.1 illustrates that over a significant range of bias, effectively no current flows between the InN sample and the solution.

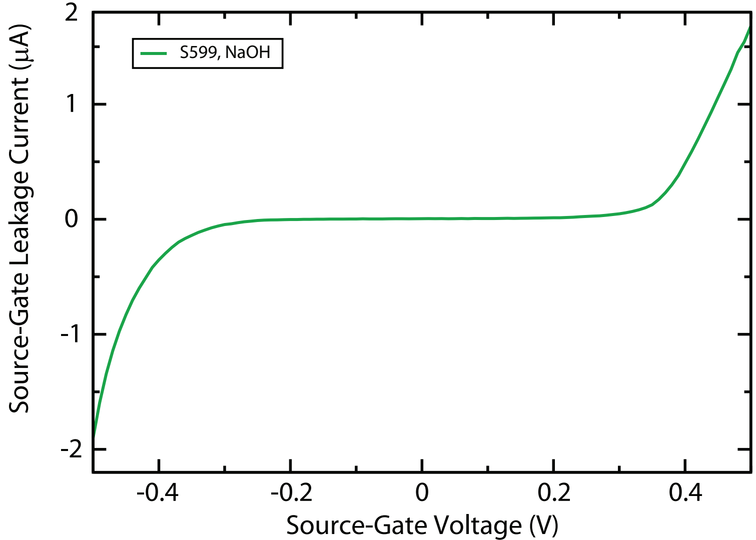


**Figure D.1** Current-Voltage (IV) relationship between one of the contacts and the Pt counter electrode, leakage current measurement from source to gate electrode, for sample S599.